Carboniferous tectono-metamorphic evolution of the Variscan crust in the Belledonne-Pelvoux area.

Kévin Fréville, Pierre Trap, Jonas Vanardois, Jérémie Melleton, Michel Faure, Olivier Bruguier, Marc Poujol, Phillipe Lach

To cite this version:

Kévin Fréville, Pierre Trap, Jonas Vanardois, Jérémie Melleton, Michel Faure, et al.. Carboniferous tectono-metamorphic evolution of the Variscan crust in the Belledonne-Pelvoux area.. Bulletin de la Société Géologique de France, inPress, 10.1051/bsgf/2022008 . insu-03678397v1

HAL Id: insu-03678397
https://insu.hal.science/insu-03678397v1

Submitted on 25 May 2022 (v1), last revised 22 Aug 2022 (v2)

Carboniferous-Permian tectono-metamorphic evolution of the Pelvoux massif (External Crystalline Massif, Western Alps), with discussion on flow kinematics of the Eastern-Variscan Shear Zone.

Évolution tectono-métamorphique Carbonifère-Permien du massif du Pelvoux (Massif cristallin externe, Alpes occidentales), avec discussion sur la cinématique de fluage de la zone de cisaillement Est Varisque.

Kévin Fréville[1,2,3], Pierre Trap[2], Jonas Vanardois[2], Jérémie Melleton[3], Michel Faure[1], Olivier Bruguier[4], Marc Poujol[5], Philippe Lach[3]

[1] UMR 7327, Institut des Sciences de la Terre d'Orléans, Université d'Orléans, CNRS, 45071 ORLEANS Cedex 2, France.

[2] UMR 6249 Chrono-environnement, Université de Franche-Comté, 16 route de Gray, 25030 Besançon Cedex, France

[3] BRGM-French Geological Survey, 3 Avenue Claude Guillemin, 45100, Orléans, France.

[4] Géosciences Montpellier, Université de Montpellier, CNRS, Place Eugène Bataillon, 34095 Montpellier Cedex 5, France

[5] Univ. Rennes, CNRS, Géosciences Rennes -UMRS 6118, F-35000 Rennes, France

Corresponding author: kevin.freville@gmail.com

Keywords: Variscan belt, Western Alps, Belledonne-Pelvoux, East-Variscan Shear Zone, migmatite, transpression.

Mot clés : Chaîne Varisque, Alpes Occidentales, Belledonne-Pelvoux, Zone de Cisaillement Est varisque, migmatite, transpression.

Abstract

Based on new structural, petrological and U-Th-Pb geochronological data, a reappraisal of the Variscan tectono-metamorphic history of the Pelvoux massif (External Crystalline Massif, French Alps) is proposed with the aim to understand the flow pattern and kinematics of the Variscan partially molten crust and the Eastern Variscan Shear Zone. The Pelvoux massif consists of high-grade metamorphic rocks of middle to lower crust, mostly migmatites, that record a prominent syn-metamorphic deformation event (D_2) characterized by a pervasive NE-SW striking, steeply dipping, S_2 foliation, and a network of anastomosed NS and NW-SE trending shear zones, the kinematics of which indicates a sinistral transpression. Relics of an early synmetamorphic event (D_1/M_1) related to crustal thickening and top-to-the east nappe stacking are also reported. Both the D_1 and D_2 features are interpreted as reflecting a NW–SE shortening event, firstly marked by dominant nappe stacking, and secondly overprinted by a sinistral transpression that started at peak metamorphism with the onset of crustal partial melting at ca. 650°C during the late Visean (ca 335-330 Ma). Ongoing sinistral D_2 transpression in the partially molten middle-lower crust of the Pelvoux involved strain partitioning between C and C' shear zones and horizontal longitudinal flow in the range 330-300 Ma. Along the anatectic front, vertical shortening and top-to-the NW shearing (D_3) is coeval with D_2 and argue for south-eastward motion of the partially molten crust. The contemporaneity between NW-SE directed transpressional flow and vertical shortening is supported by our radiometric data of D_2 and D_3 and attests for strain partitioning between the suprastructure and infrastructure during horizontal crustal flow under transpressive regime. The exhumation of deep-seated rocks during sinistral transpression followed a near isothermal (ca. 700 °C) evolution down to pressure of ca. 0.5 GPa in the period 325-306 Ma. The sinistral transpression recorded in the Pelvoux massif might corresponds to an antithetic shear zone coeval with the dextral East-Variscan Shear Zone, proposed for this part of the Variscan orogen.

Résumé

Sur la base de nouvelles données structurales, pétrologiques et géochronologiques U-Th-Pb, une réévaluation de l'histoire tectono-métamorphique varisque du massif du Pelvoux (Massif cristallin externe, Alpes françaises) est proposée dans le but de comprendre le style et la cinématique du fluage de la croûte varisque partiellement fondue et de la Zone de

Cisaillement Est Varisque. Le massif du Pelvoux est constitué de roches métamorphiques de haut grade, de la croûte moyenne à inférieure, principalement des migmatites, qui enregistrent un événement de déformation syn-métamorphique prédominant (D_2) caractérisé par une orientation NE-SW, une foliation S_2 à fort pendage et un réseau anastomosé de zones de cisaillement d'orientation NS et NW-SE dont la cinématique indique une transpression senestre. Des reliques d'un événement synmétamorphique précoce (D_1/M_1) lié à l'épaississement de la croûte et à l'empilement des nappes à vergence Est sont retrouvées. Les caractéristiques de D_1 et D_2 sont interprétées comme reflétant un événement de raccourcissement NW – SE, d'abord marqué par l'empilement dominant des nappes, qui évolue ensuite en une transpression senestre, initiée au pic du métamorphisme avec le début de l'anatexie crustale dès 650°C, à la fin du Viséen (335-330 Ma). Dans la croûte partiellement fondue, la déformation transpressive senestre D_2 se partitionne avec la formation de zones de cisaillement C et C' qui accommodent le fluage longitudinal entre 330 et 300 Ma. Le long du front anatectique, un raccourcissement vertical accompagné d'un cisaillement vers le NW (déformation D_3) sont contemporains de D_2 et participent aussi à l'échappement vers le sud-est de la croûte partiellement fondue. La contemporanéité entre le fluage transpressif dirigé NW-SE (D_2) et le raccourcissement vertical à cinématique NW (D_3) est étayée par nos données radiométriques. L'exhumation des roches profondes lors de la transpression senestre a suivi une évolution quasi isotherme (~ 700 ° C) jusqu'à une pression d'environ 0,5 GPa dans la période 325-306 Ma. La transpression senestre enregistrée dans le massif du Pelvoux pourrait correspondre à une zone de cisaillement antithétique contemporaine de la zone de cisaillement dextre Est-Varisque.

1. Introduction

Together with the Maures-Corsica-Sardinia massifs, the External Crystalline Massifs (ECMs), exposed in the Helvetic zone of the Western Alpine belt represent the Eastern Branch of the Variscan orogen (Fig. 1). In spite of several geodynamic interpretations (Corsini & Rolland, 2009; Faure et al., 2014; Faure and Ferrière, 2022; Fernandez et al., 2002; Guillot & Ménot, 2009; Oliot et al., 2015; Rossi et al., 2009; Von Raumer et al., 2013), the timing of the main tectono-metamorphic events in the ECMs, and the correlations between these massifs remain poorly constrained mainly because of a strong imprint by late-orogenic transpressional tectonics during Carboniferous time and intense partial melting and plutonism in the mid-lower crust at that time. Widespread Carboniferous crustal partial melting in response to thermal relaxation (i.e. Alcock et al., 2015; Barbey et al., 2015; Villaros et al., 2018) triggered horizontal flow of the lower and middle crust (Vanderhaeghe et al., 2020, Cochelin et al., 2017) and strain partitioning along strike-slip shear zone and exhumation of migmatitic domes (Vanderhaeghe et al., 1999; Ledru et al., 2001). In the ECMs, the structural and kinematic feature associated with partial melting and magmatism are still elusive.

The Eastern Crystallin Massifs (ECMs) stand out as a complex portion of the European Variscan Belt that was built along a major crustal-scale wrenching corridor, named the East Variscan Shear Zone EVSZ (Fig. 1A; EVSZ; Carosi et al., 2012; Corsini & Rolland, 2009; Guillot & Ménot, 2009; Padovano et al., 2012, 2014; Rolland et al., 2009; Simonetti et al., 2018). The EVSZ is considered as the main structure that accommodated the shaping of the variscan eastern orocline (Fig. 1A; Ballèvre et al., 2018; Bellot, 2005; Matte, 2001). A series of multidisciplinary studies have provided many structural, petrological, and radiometrical data in that part of the East Variscan branch that was affected by the EVSZ (Guillot and Menot, 2009), i.e. the Aiguilles-Rouges and Mont-Blanc massif (Von Raumer et al., 2013; Von Raumer and Bussy, 2004, Simonetti et al., 2020a), the Belledonne-Pelvoux massifs (Guillot and Menot, 2009), the Argentera Massif (Simonetti et al., 2018, 2021), the Maures-Tanneron massif (Rolland et al., 2009, Schneider et al., 2014; Gerbault et al., 2018, Simonetti et al., 2020b), and Sardinia (Carosi et al., 2012) showing that the EVSZ was responsible for complex strain partitioning in time and space during Carboniferous. Simonetti et al. (2020a) proposed the first detailed picture of the EVSZ with the position, orientation and kinematics of the major branches constituting the regional-scale anastomosed system (Fig. 1B). Because not all ECMs are considered in the EVSZ system, the location, thickness and internal strain pattern of the EVSZ remains elusive as well as the variations of strain regimes and kinematics that are expected to exist at lithospheric scale.

In this contribution we focus on the Belledonne-Pelvoux area that is a large but still poorly understood portion of the ECMs, and absent from the reconstruction of the EVSZ anastomosed system (Fig. 1B). The Pelvoux massif displays a well exposed section of the late-Variscan low and middle crust mainly composed of migmatites and granites formed in response to a crustal melting event developed at the end of a HT low-to-medium pressure Carboniferous metamorphism (Pecher, 1970; Le Fort, 1973). There, a sinistral kinematics was documented (Strzerzynski et al., 2005) making it unique in the transpressive framework of the ECMs where dextral shearing dominates (Carosi et al., 2012; Corsini & Rolland, 2009; Guillot & Ménot, 2009; Padovano et al., 2012, 2014; Rolland et al., 2009; Simonetti et al., 2018, 2020a).

Presently, the Pelvoux massif lacks large-scale structural analysis combined with quantified tectono-metamorphic evolution using modern petrological methods. Simonetti et al. (2018; 2020a, 2020b) suggested that dextral transpression in the ECMs was initiated at ca. 320 Ma with the exception of the Argentera massif where it could have started at ca. 330-340 Ma. In the Pelvoux massif, rare geochronological data document the protolith age of some orthogneiss, but the syn-metamorphic deformation is still undated. A study of the Pelvoux massif will help integrating the sinistral kinematics in the general framework of the dextral transpression model of the EVSZ (e.g. Simonetti et al., 2020a) and of the whole Variscan belt (e.g. Ballèvre et al., 2018; Edel et al., 2018).

In this article, we present (i) the detailed finite strain pattern at the transition from the upper crust and the former partially molten crust that crops out in the Pelvoux massif and (ii) microstructural, petrological and geochronological analyses on samples from the unmolten and molten crust. These results allow us to discuss (i) the P-T-D-t evolution recorded in some high-grade metamorphic rocks; (ii) the geometrical and temporal relationships between deformation, metamorphism, partial melting, and magma emplacement; (iii) the kinematics of ductile flow in the mid-crust. Our findings are compared to those recently obtained on the adjacent Belledonne massif by Fréville et al. (2018) and Jacob et al. (2021) and enable us to propose a tectono-metamorphic evolution model of the Pelvoux that may represent an antithetic branch of the EVSZ.

Geological setting.

2.1. Overview of the Variscan Belt in the Alpine Crystalline massifs

The Variscan belt formed in response to collision between Gondwana and Laurussia continents, and several Gondwana-derived microcontinents during the Late Devonian to Early Carboniferous (Fig. 1A), (Autran and Cogné, 1980; Paris and Robardet, 1990; Franke, 2000; Tait et al., 1997, 2000; Matte, 1991, 2001, 2007; Von Raumer et al., 2003; Faure et al., 2005; Stampfli et al., 2013). From Late Visean to Early Permian, thermal relaxation and mafic to felsic plutonism enhanced a widespread partial melting of the thickened low-middle crust, that modified gravity vs boundary stress balance and enhanced a complex intracontinental strain partitioning in a global transpressive regime (e.g. Rabin et al., 2015; Cochelin et al., 2017; Henk et al., 2000).

In its present geometry, the External Crystalline Massifs (ECMs) of the Alps form an arcuate, concave to the East, branch of the Variscan belt that includes, from North to South, the *Aar-Gothard*, *Aiguilles Rouges-Mont Blanc*, *Belledonne*, *Grandes Rousses*, *Pelvoux*, and *Argentera* massifs (Fig. 1B) (e.g. Barfety et al., 2000; Guillot and Ménot, 2009). A first-order three-fold subdivision, previously proposed by Bordet and Bordet (1963), and Guillot and Ménot (2009) (Fig. 1B), defines the Western, Central and Eastern domains.

The Western domain consists of slightly metamorphosed micaschists and metagreywackes considered as a turbiditic series of Ordovician age (Bordet and Bordet, 1963; Fréville et al., 2018). The central domain, including the SW part of the Aiguilles Rouges, the SW part of Belledonne massifs, and the western part of the Pelvoux massif or Cortical Pelvoux area (Le Fort, 1973; Fig. 2) is made of a stack of several litho-tectonic units, namely from top to bottom: (i) the Cambro-Ordovician Chamrousse ophiolite (Carme, 1965a; Carme, 1965b; Carme, 1970; Bodinier et al., 1981; Ménot, 1987; Pin and Carme, 1987; Ménot, 1988a; Ménot, 1988b); (ii) an amphibolitic facies gneiss, micaschists and volcano-sedimentary rocks (VSU, *Riouperoux-Livet* and *Allemont* units) overlained by (iii) a weakly metamorphosed and deformed conglomerate, black schist, and acidic volcanic rocks, named the *Taillefer* unit (Gibergy, 1968; Ménot, 1988; Fréville et al. 2018).

The Eastern part of the ECMs consists of high-grade rocks of the mid-lower crust with migmatites enclosing several lenses of HP granulites and retrogressed eclogites that crop out in the *Argentera* massif, the Inner Pelvoux area, the NE Belledonne area, the major part of the *Aiguilles Rouges-Mont Blanc* massif, and the *Aar-Gothard* massif. (Fig. 1B, Paquette et al., 1989; Abrecht and Biino, 1991; Lombardo et al., 1997; Von Raumer and Bussy, 2004; Ferrando et al., 2008; Compagnoni et al., 2010; Rubatto et al., 2010; Jacob et al., 2021). These three crustal domains are juxtaposed along the Synclinal-Median Fault (SMF) and the Rivier-Belle Etoile Fault (RBEF, Fig. 1B)

2.2. Impact of the post-variscan reworking in the Belledonne-Pelvoux area

The Jurassic rifting, coeval with the opening of the Liguro-Piemonte ocean, was responsible for the development of brittle normal faults associated with the local tilting of the Paleozoic basement. It was responsible for the individualization of several Liassic blocks. These are the *La Mure* and *Le Taillefer* blocks within the Belledonne massif, and *Le Rochail*, *L'Emparis*, *La Meije*, and *Le Combeynot* blocks in the Pelvoux massif (Fig. 2) (Lemoine et al., 1986; Barféty et al., 1988; Lemoine, 1988). The Miocene Alpine deformation inverted the Jurassic normal faults and was responsible for the development of localized NW-SE trending shear zones with a top-to-the NW ductile shearing (Bellahsen et al., 2014; Bellanger et al., 2014, 2015; Boutoux et al., 2014). The Alpine shortening in the Paleozoic basement was coeval with a weak metamorphic overprint in the prehnite-pumpellyite to greenschist facies. Outside these localized Alpine shear zones, the markers of the Pre-Alpine tectono-metamorphic events are particularly well-preserved in the Belledonne-Pelvoux area.

2.3. Summary of previous P-T-t data on the Pelvoux Massif

In the literature, the Pelvoux massif is described as two-fold, with the Cortical and the Inner Pelvoux domains, the boundary of which is mainly reworked by alpine faulting (Le Fort, 1973). The Cortical Pelvoux, located in the western part, consists of an alternation of volcaniclastic rocks and micaschists with migmatitic gneisses at the base of these series (Fig. 2). Barrovian metamorphism is attested by kyanite-staurolite bearing micaschists documented in the Cortical Pelvoux (Le Fort, 1973) but quantitative thermobarometric estimates are not available. In the adjacent SW Belledonne, a MP-HT barrovian metamorphism (M_1) is documented with P-T conditions at ca. 0.5-0.6 GPa, 600 °C, recorded in staurolite-bearing micaschists and up to ca. 0.8 GPa, 680 °C for the migmatitic gneiss in lowest unit (Guillot and Ménot, 1999; Fernandez et al., 2002; Fréville et al., 2018). The M_1 metamorphism is coeval with a D_1 deformation characterized by the development of a westward dipping foliation S_1 and E-W stretching L_1 lineation interpreted as an eastward nappe stacking event (Fréville et al., 2018). At upper structural level in the Cortical Pelvoux, a series of micaschists and volcaniclastic rocks is overlain by black schists and conglomerates, similar to the *Taillefer* unit observed in SW Belledonne (Barfety et al., 2000; Guillot and Ménot, 2009) (Fig. 2).

The Inner Pelvoux is composed of i) migmatites that developed through partial melting of paragneiss, orthogneiss and amphibolite, and ii) several generations of granitoids (Pecher, 1970; Le Fort, 1973). Some mafic lenses (e.g. *Peyre-Arguet*, Fig. 2) within migmatitic paragneiss record amphibolite facies P-T conditions of 0.7 ± 0.1 GPa, 650 ± 50 °C, and a low-pressure granulite facies of 0.5 ± 0.1 GPa, 800 ± 50 °C, followed by a retrogressive evolution in the greenschist facies conditions (Grandjean et al., 1996). Granulitic conditions have also been inferred from the migmatitic gneiss (Pecher, 1970; Pecher and Vialon, 1970) but without any phase diagram quantification. Two episodes of partial melting are recognized with a first low-temperature, cordierite-free migmatite, and a high-temperature – low-pressure, cordierite-bearing migmatite (Bogdanoff et al., 1991). In the Inner Pelvoux, the foliation is mostly steeply dipping to vertical, but superimposed deformation has been invoked (Pecher, 1970; Le Fort, 1973) and the relationships between partial melting and deformation are still unclear.

Two groups of granitoids are distinguished, namely two-mica granites and monzonitic granites (Barféty et al., 1982; Debon and Lemmet, 1999). Presently, only the two-mica Rochail and Combeynot granites, and the Turbat-Lauranoure monzonite have been dated with proposed emplacement age at 343 ± 11 Ma, 312 ± 7 Ma and 302 ± 2 Ma, respectively (U-Pb on zircon; Canic, 1998; Guerrot and Debon, 2000). N-S to NW-SE striking, syn-magmatic sinistral C-S fabrics are described in granitic plutons (Strzerzynski et al., 2005) but the geometrical and kinematic relationships with their migmatitic host rocks are poorly understood.

3. Structural analysis

3.1. Strain patterns in the metamorphic and migmatitic pile

At the scale of the entire Pelvoux massif, field observations show that the dominant macroscopic ductile structure is a steeply dipping foliation, ascribed here to the D$_2$ event (Fig. 3 and 4). Due to its pervasive character, the D$_2$ event will be presented first.

3.1.1 The D$_2$ submeridian sinistral shearing

The majority of this D$_2$ planar structure is represented by a gneissic (i.e. solid-state deformation), and a migmatitic foliation (i.e. suprasolidus deformation). It ranges from NW-SE to NE-SW with the occurrence of three main directional populations: ~N30°E, ~N140°E and ~N170°E (Figs. 3 and 4). The ~N30°E foliation is less represented than the two other directions and is referred to as S$_2$ in the following. S$_2$ is axial planar to upright folds F2 that deform~~s~~ an earlier weakly dipping S$_1$ foliation (see below). S$_2$ developed in response to an E-W to NW-SE bulk shortening (Figs. 5A and 5B). In the Inner Pelvoux, S$_2$ consists of a migmatitic layering that almost totally transposes S$_1$ that is only preserved within F$_2$ folds hinges (see next paragraph and Fig. 5C).

The two most developed D_2 planar fabrics are striking N170°E and N140°E with a high (>70°) dip angle (Fig. 3). Both sets show melt-present and solid-state deformation features (Fig. 5D). When the three directional populations of planar fabrics, i.e. ~N30°E, ~N140°E and ~N170°E are observed on the same outcrops, the cross-cutting relationships clearly indicate that the ~N170°E planar surface is a shear plane that reworks the ~N30°E directed foliation, and that both ~N30°E and ~N170°E trending planar surfaces are reworked by the ~N140°E shear zone, as portrayed in Figure 7.

In the northern and eastern portions of the Emparis and La Meije Blocks, the N170°E trending and highly penetrative planar surface forms 100 meters to several kilometers wide shear zones (Figs. 3 and 4) along which a southward low-angle plunging L_2 stretching lineation is observed (Fig. 3B). A sinistral kinematics is deduced from the observation of sigmoidal minerals or aggregates and the deflection of S_2 (Figs. 3, 5E, 5F, 6A). In the southern part of the Pelvoux massif, similar meter to kilometers sized sinistral high-strain corridors strike mostly ~N140°E (Fig. 3). Where the NW-SE planar fabric becomes preponderant, the N-S surface is only preserved within centimeter to meter scale lenticular bodies (Fig. 7A). The mineral and/or stretching lineations are rarely observed; but when it is the case, they are sub-horizontal or moderately plunging (Fig. 3). In some places, within stromatic migmatite, the oblate shape of mafic restites suggests that flattening strain without the development of a preferred stretching direction was dominant (Fig. 6B). At the outcrop scale, some conjugate dextral and sinistral shear bands are also observed (Fig. 6C). Considering the geometric and kinematic features of the D_2 structures, it appears that the N170°E and N140°E planar surfaces might be considered as C_2 and C'_2 shear planes that developed synchronously with S_2 in a bulk sinistral strike-slip regime. This S_2, C_2, C'_2 anastomosing system is observed from kilometer to meter scale (Figs. 3). The presence of leucosome within the S_2, C_2 and C'_2 shear bands attests for the onset of D_2 in a partially molten rock, under supra-solidus conditions (Fig. 5). Diatexite commonly shows rafts and schollens with a high aspect-ratio parallel to the migmatitic foliation arranged either on the C_2 or C'_2 trends (Figs. 6D, 6E and 6F). In some places, cm-scale elongated cordierite aggregates are preferentially aligned along C_2 and C'_2 planes (Fig. 6F) indicating that low-pressure/high-temperature partial melting was coeval with the D_2 sinistral strike-slip. The D_2 planar surface is also reported within garnet-bearing amphibolites (Fig. 7B) that are interpreted as retrogressed HP granulites (Grandjean et al., 1996).

3.1.2 The relictual D_1 structure

The D_2 anastomosed system reworks a nearly horizontal or westward shallowly dipping early foliation, named S_1 (Figs. 3 and 4). Within the Inner Pelvoux, the relictual S_1 foliation corresponds to a gneissic layering and lithological alternations, the attitude of which marks large scale F_2 folds. This is exemplified by the attitude of the La Lavey amphibolite formation in the La Meije block where a low angle (20-40°) S_1 foliation is observed (Fig 3). In the Inner Pelvoux, the S_1 foliation only remains as isolated F_2 fold hinges (Figs. 5A and 5B). In the Cortical Pelvoux, a S_1 gneissic layering with a low-angle dip is also recognized. It is worth noting that L_1 lineation is very rare with no clear preferred direction. Generally, the superimposition of S_2 and S_3 over S_1 makes the latter difficult to depict in the outcrop. Relics of S_1 are best recognized at the cm-scale (thin section) (Fig. 8B).

3.1.3 Late horizontal shearing: D_3 structure

A flat-lying foliation (S_3) superimposed on both the D_1 and D_2 fabrics is observed in the Inner Pelvoux, at m-cm scale, and attributed here to a D_3 deformation (Fig. 3, 4 and 8). The D_2 planar fabric elements (S_2-C_2-C'_2) are involved in the formation of S_3 axial planar F_3 folds, and C_3 shear bands with top-to-the-NW kinematics (Figs. 8 and 9). The attitude of leucosome that parallels S_3 and the horizontal axial plane of F_3 folds argue for melt migration during D_3 (Figs. 9A and B). The melt-bearing S_3 foliation cuts across S_2 the upper structural level of the *La Meije* block.

In the *Le Rochail* block, a similar D_3 strain pattern is observed with centimeter-scale F_3 folds, with sub-horizontal axial planes that rework the subvertical S_2 foliation. F_3 fold axes are weakly plunging toward the NW. In the Cortical Pelvoux, a kilometer-scale D_3 decreasing strain gradient can be observed from west to east. The S_3 becomes more penetrative and presents a mylonitic fabric in which a N150-160°E stretching lineation L_3 is observed (Figs. 3 and 8D). Along the L_3 stretching lineation, kinematic criteria (sigmoidal structures, pressure shadow, and shear bands) indicate a top-to-the northwest sense of shear whatever the observation scale (Figs. 8 and 9). A-type folds with axes parallels to L_3 lineation can be also observed. Accordingly, a similar stretching direction is documented by Jacob (2022) and Jacob et al. (2022) in the La Meije Block with the observations of a syn-migmatitic flat-lying foliation documenting a N150-N180 directed horizontal flow that reworks early D_1 and D_2 fabrics.

3.2. Strain patterns in the felsic plutons

Within the granitic bodies of the Inner Pelvoux area (e.g. Turbat-Lauranoure, Etages, La Bérarde-Promontoire plutons), the S_1, S_2 and S_3 were not identified but the two C_2 (~N170°E) and C'_2 (N140°E) structures are recognized. The preferred orientation of feldspar, biotite and shape ratio of mafic enclaves define a ~N160-170°E striking subvertical magmatic foliation. When observed, the stretching lineation is sub-horizontal and trends NNW-SSE as previously described by Strzerzynski et al. (2005). In agreement with these authors, we also document the presence of N135-140°E striking and vertical ductile shear bands. These shear-bands rise to C-S -like structures, which reflect a sinistral strike-slip shearing, as best exemplified in the Bérarde-Promontoire and Etages granites (Fig. 3). In agreement with Strzerzynski et al. (2005), we consider that the sinistral kinematics was coeval with pluton emplacement. These C_2 and C'_2 planar surfaces that developed under supra-solidus magmatic conditions, appear in continuity with the D_2 structures observed in the country rocks, indicating a syn-D_2 emplacement of those plutons.

In the northern part of the Cortical Pelvoux, the Rochail granite shows a sub-horizontal magmatic foliation inferred from biotite arrangement (Barféty et al., 1988) and does not show subsolidus deformation. The D_2 deformation was not observed in the pluton, and the S_3 foliation wraps around the granite (Fig. 4A). This may indicate that the flat-lying magmatic foliation could be ascribed to S_1 (see discussion below in section 5).

4. Petro-chronological results

This section presents U-Th-Pb radiometric analyses of monazite and zircon grains from (1) mylonitic gneiss (samples *MCE379* and *MCE382b*), (2) Al-rich metapelites (samples *MCE339v, MCE338* and *MCE328*), (3) migmatites (samples *MCE314, MCE330, MCE140b* and *MCE313b*) and (4) metamafics (sample *MCE304v2*) sampled in the Cortical and Inner Pelvoux (Fig. 2; Table 1). A petrological description is given for each sample (Fig. 10). Before isotopic analyses, cathodoluminescence (CL) and back-scattered electron (BSE) images were acquired for all zircon and monazite grains, respectively, using a scanning electron microscope (SEM) in order to check spot locations with respect to the internal microstructures, inclusions, fractures and physical defects. For monazite, U-Th-Pb analyses were performed by LA-ICP-MS directly in thin section at the University of Montpellier (samples *MCE338*, *MCE314* and *MCE382b*) and at BRGM (Bureau de Recherche Géologique et Minière) (*MCE328, MCE339v* and *MCE379*) (Table S_1). The analytical protocol for the University of Montpellier followed the procedure described in Bruguier et al. (2017) and is presented in Table S2. Manangotry (Poitrasson et al., 2000) and Moacyr (Goncalves et al., 2016) monazites used as calibration and quality control reference materials yielded concordia ages of 552 ± 2 Ma (MSWD=2.2, n=38) and 507 ± 2.5 Ma (MSWD=0.02, n=14), respectively. The analytical protocol for the BRGM is presented in Table S3 and the Madmon and Namaqualand monazites used as quality control reference materials yielded concordia ages of 514 ± 7 Ma (MSWD=1.4, n=10) and 994 ± 17 Ma (MSWD=1.3, n=10), respectively.

The zircon U-Pb analyses were performed at BRGM (Sample *MCE330*, *MCE 304v2* and *MCE313b*) and at GeOHeLiS analytical platform (University Rennes 1) (Sample *MCE140b*, Table S1, S4). Zircon grains were obtained by a conventional mineral separation. The selected grains (~100-200 µm size) were mounted in epoxy resin and polished down to expose their near equatorial sections. The analytical protocol for the BRGM is presented in Table S3 and the Plešovice zircon (Sláma et al., 2008) used as quality control reference material yielded a concordia age of 340 ± 3 Ma (MSWD=1.5, n=24). The analytical protocol for the GeOHeLiS analytical Platform is presented in Table S4 and the Plešovice zircon (Sláma et al., 2008) used as quality control reference material yielded a concordia age of 337.6 ± 2.0 Ma (MSWD=0.23, n=15). See Manzotti et al. (2016) for more details on the analytical protocol.

Two Al-rich metapelitic samples (*MCE339v* and *MCE338*) were investigated for their metamorphic evolutions through petrology and phase diagram calculations. Electron microprobe analysis has been performed at the University of Orléans on a CAMECA SX-FIVE. The P-T metamorphic conditions were obtained through calculations of pseudosection diagrams using Perple_X 6.9.1. software (Connolly and Pettrini, 2002; Connolly, 2005; hpver62 database from Holland and Powell, 2011). The considered system was MnO-Na_2O-CaO-K_2O-FeO-MgO-Al_2O_3-SiO_2-H_2O (MnNCKFMASH). Solution models used in the calculations were garnet, biotite, white mica, staurolite, cordierite, chlorite, chloritoid and melt (White et al., 2014) as well as plagioclase (Fuhrman & Lindsley, 1988) and ilmenite (White et al., 2000). Whole rock major element compositions (Table 2) were obtained using a PANalytical AxiosmAX X-Ray Fluorescence (XRF) Spectrometer at Lausanne University, Lausanne, Switzerland. The P–T conditions of biotite, muscovite and plagioclase equilibrium were estimated using the third model quality factor Qcmp described in Duesterhoeft & Lanari (2020) in order to have a quantitative approach. This factor calculates the fitting between the mineral composition and the composition modelled and takes account of the relative analytical uncertainty of the extracted compositions. The comparison of mineral composition was restricted to MnO, MgO, FeO, SiO_2 and Al_2O_3 contents for biotite, of Na_2O, K_2O, CaO, Al_2O_3, FeO, MgO and SiO_2 contents for muscovite, and of CaO, K_2O, Na_2O, SiO_2 and Al_2O_3 contents for plagioclase.

4.1. Gneissic mylonites (samples MCE379 and MCE382b)

The sample *MCE379* is a gneiss from the volcano-sedimentary unit of the northern part of the Cortical Pelvoux where the main planar fabric is a composite S_{1-3} foliation (Fig. 4A). It is composed of Qtz + Kfs + Bt with rare garnet and muscovite occurrences and few late white micas (Fig. 10A). It is structured by D_1 shear planes oriented N120°E/30NW, kinematic is not clear because of D_3 superimposition. Quartz ribbons show undulose extinction and Grain Boundary Migration recrystallization (GBM; Stipp et al., 2002). Monazite is located either in the quartzo-feldspathic matrix (Fig. 10B) or as an undeformed inclusion in biotite marking the S_1 foliation (Fig. 10C and D). Monazite grains do not show any zonation in BSE images (Fig. S1) and have U, Pb and Th contents ranging between 1322-3462 ppm, 869-2110 ppm and 22326-72038 ppm, respectively, with Th/U ratios between 8.1 and 27.8 (Table S1). Twenty-nine analyses were performed on 26 monazite grains within the matrix. Except two discordant analyses, all analyses yield a concordant date at 334.8 ± 3.2 Ma (n = 27; $MSWD_{(C+E)}$ = 1.3) (Fig. 12A).

Sample *MCE382b* is a gneiss coming from the same area as sample *MCE379* (Fig. 2). It is composed of Qtz + Kfs + Bt + Grt + late Ms (Fig. 10E). In this sample, D_3 strain is higher than in sample *MCE379* and the D_3 mylonitic planar fabric is oriented N133°E;30NE with a L_3 stretching lineation trending N120°E. C-S structures and sigmoidal quartz aggregates indicate top-to-the-NW kinematics (Fig. 10E). Quartz crystals are stretched and form quartz-ribbons with undulose extinction and GBM recrystallization.

Fourteen monazite grains from sample *MCE382b* have been analyzed *in situ*, they do not show any zonation (Fig. S1) but display two habitus: monazite included in large biotite marking the S_3 foliation (group 1; Fig. 10G and H) and monazite located inside the quartzo-feldspathic matrix (group 2; Fig. 10F). Monazite grains from the quartzo-feldspathic matrix (group 2) have U, Pb and Th contents between 740-1016 ppm, 1198-1796 ppm and 15803-26505 ppm, respectively, and Th/U ratios of 19.4-36.9 (Table S1). Monazite inclusions within large biotite marking the S_3 foliation (group 1) have higher U contents (1241-1997 ppm), similar Pb and Th contents (1063-1478 ppm and 11914-21818), and lower Th/U ratios (6.1-16.4). Two ages can be identified (Fig. 11B), the oldest one is calculated from 7 monazite grains located in the matrix (group 2) that provide a concordant date at 334.5 ± 3.4 Ma ($MSWD_{(C+E)}$

= 0.88). The second one is obtained from 4 grains included within large biotite (group 1) yielding a concordant date at 306.0 ± 3.5 Ma ($MSWD_{(C+E)}$ = 0.39).

4.2. Al-rich metapelites (samples MCE339v, MCE338 and MCE328)

Sample *MCE339v* is a micaschist composed of Qtz + Grt + Ky + St + Bt + Ms + Pl (Fig. 11A) sampled in the middle part of the Cortical Pelvoux (SW of Entraigues village, Fig. 2). It is structured by a pervasive D_2 shear zone oriented N0°E;70E with a horizontal stretching lineation trending N0. Staurolite and kyanite are relictual and are strongly affected by the D_2 shearing. An old foliation, probably S_1, is preserved in kyanite and garnet (Fig. 11B). Micas and quartz layers form sinistral sigmoids wrapping around garnet porphyroblasts.

Garnet grains show a slight zonation (Fig. 13A) with a core composed of ca. 64% of almandine, 5% of pyrope, 18.5% of grossular and 12.5% of spessartine, and a rim composed of 74% of almandine, 12% of pyrope, 13% of grossular and 1% of spessartine (Table 3). Mineral compositions were modified by diffusion processes, as suggested by the smooth compositional zoning (Fig. 13A). Plagioclase is an oligoclase with $Ab_{76,}$ and biotite presents a stable composition at X_{Fe} 0.57 (Table 3). A phase equilibrium diagram was calculated for this sample with a H_2O content at 1.33 % wt, which corresponds to the saturation of the sample at the solidus conditions as estimated from a T-X_{H2O} diagram (Fig. 13B). The obtained phase diagram defines a large stability field corresponding to the mineral assemblage of sample *MCE339v* (Qtz + Grt + Ky + St + Bt + Ms + Pl) with temperature and pressure conditions below 600 °C and 0.7 GPa, respectively (Fig. 13C). The phase diagram fails to reproduce the garnet core composition, perhaps due to diffusion process and modification of the initial composition of the garnet core. The Qcmp factor of the plagioclase composition only slightly varies, and its maximal value is 99.8% of fitting with the reference composition (Fig. 13C). This highest Qcmp value (Duesterhoeft et Lanari, 2020) indicates P-T conditions inferior to 650 °C and 0.6 GPa and is well expressed in the stability field of the mineral assemblage (Fig. 13C). The Qcmp factor of the biotite reaches a value of 95% of fitting with the reference composition and indicates temperatures between 525 and 750 °C and pressure conditions between 0.4 and 0.7 GPa and only expressed in the stability field of the mineral assemblage at around 550 °C and 0.5 GPa (Fig. 13D). These results must be taken with caution due to potential diffusion processes that might have affected the mineral compositions and analytical uncertainties on the reference compositions.

Monazite grains from sample *MCE339v* do not show any zonation, however two populations are recognized: the first one (group 1) is composed of monazite grains not oriented within the S_2 foliation and often included in quartz and sometimes in kyanite (Fig. 11B), displaying U, Pb and Th contents at 2985-6844 ppm, 1894-4304 ppm and 20221-45439 ppm, respectively, and medium Th/U ratios (5.1-7.6). The second population (group 2) is composed of monazite grains oriented parallel to the main S_2 foliation in mica-rich layers (Fig. 11C), with higher U and Pb contents ranging at 7069-8247 ppm and 4006-4827 ppm, Th varying in the range 33668-50915 ppm. The Th/U ratios are in the range 4.8-6.7 (Table S1). Analyses performed on monazite grains from the first group yield a concordant date at 346.6 ± 4.8 Ma (n = 7; $MSWD_{(C+E)}$ = 0.51) (Fig.11C), whereas analyses from the second group of monazite grains provide a concordant date at 319.2 ± 6.1 Ma (n = 4; $MSWD_{(C+E)}$ = 0.78).

Sample *MCE338* is a metapelite sampled in the middle of the Cortical Pelvoux (Fig. 2). It is composed of Qtz + Pl + Ms + Bt + Grt + Sill with scarce tourmaline (Fig. 11D). The main planar fabric is a S_1 foliation showing numerous variscan sigmoidal and C-S structures reoriented by the alpine tectonics. Garnet grains are boudinaged by D_1 with boudin necks filled by biotite, quartz and sillimanite (Fig. 11D). Fibrolitic sillimanite is localized in D_1 structures and in D_1 sigmoid tails, suggesting a syn-D_1 crystallization. A phase equilibrium diagram was calculated for this sample. (Fig. 14). H_2O amount was defined at 1.47 %wt, which corresponds to the saturation of the sample at the solidus conditions of the mineral assemblage and was estimated from a T-X_{H2O} pseudosection (Fig. 14B). Garnet grains show a slight zonation (Fig. 14A) with a core composed of ca. 71% of almandine, 12.5% of pyrope, 5.5 % of grossular and 11% of spessartine, and a rim composed of 68.5% of almandine, 8.5% of pyrope, 4% of grossular and 19% of spessartine (Table 3). Plagioclase is homogeneous in composition with $Ab_{75,}$ and biotite presents a stable composition at X_{Fe} 0.56 (Table 3). The resulting pseudosection (Fig. 12B and C) indicates a stability field with the mineral assemblage corresponding to the one observed in the sample (i.e. Pl + Grt + Ms + Bt + Sill + Qtz). Due to its low proportion and variability, grossular was not used to constrain the P-T conditions. The almandine, pyrope and spessartine isopleths of the garnet core cross-cut at 565 ± 30 °C and 0.46 ± 0.04 GPa in the stability field of the observed mineral assemblage (Fig. 12B). Regarding the low volume of garnet in this sample (i.e. inferior to 3 vol%), we did not calculate a new pseudosection removing the garnet core bulk composition. Isopleths from the garnet rims cross-cuts at 450 ± 30 °C and 0.36 ± 0.02 GPa (Fig. 12B). The best Qcmp values of the biotite and plagioclase do not perfectly fit with these P-T conditions, but their Qcmp remains high at the

P-T conditions defined by the garnet core composition (Fig. 14D and F). The best Qcmp factor of the muscovite might indicate a higher-pressure stage around 0.7-0.8 GPa before the P-T conditions defined by the garnet core (Fig. 14E).

In the sample *MCE338*, monazite grains are included in quartz, in biotite and in muscovite-biotite layers (Fig. 11E and F). They are mainly parallel with the S_1 foliation (Fig. 11F) and sometimes show syn-D_1 kinematic criteria (Fig. 11E). They do not show zonation on BSE images (Fig. S1). Twenty-eight analyses display U, Pb and Th contents ranging between 1486-5802 ppm, 786-3070 ppm and 7372-33214 ppm, respectively, with constant Th/U ratios (4.2-6.1; Table SE1). By removing discordant data (ja8, ja11, ja15, ja20, ja24, ja27, ja28 and ja29; Table SE1), as well as the younger and older analyses (ja13 and ja5 respectively; Table SE1), the remaining data points provide a concordia date of 333.2 ± 1.6 Ma (n = 18; $MSWD_{(C+E)}$ = 0.83) (Fig. 11D).

Sample *MCE328* is a micaschist from the southern part of the Cortical Pelvoux (Fig. 2). It is composed of quartz, muscovite, biotite, staurolite and kyanite (Fig. 11G). The main planar fabric of this sample is a composite S_{1-3} foliation oriented N160°E;25E with a subhorizontal L_3 stretching lineation trending N160°E. The quartz and micas sigmoidal aggregates indicate a D_1 top-to-the-NW sense of shear, while D_3 shear bands indicate top-to-the-SE kinematics (Fig. 11G). Kyanite and staurolite, often surrounded by a white mica-corona, are deformed by the D_3 shear bands. Biotites are commonly chloritized. Monazite grains are mainly located in the quartz-matrix or in biotite marking the S_1 foliation and are typically oriented parallel to the S_1 foliation (Fig. 11H). Some monazite grains also seem included in staurolite (Fig. 11I). They do not show chemical zoning (Fig. S1). The analyzed grains display U, Pb and Th contents ranging between 3761-8639 ppm, 2160-5277 ppm and 24475-45307 ppm, respectively, and constant Th/U ratios (5.2-7.1 except one data at 4.0; Table S1). As the whole, 17 analyses were performed, among them, 14 are concordant and yield a concordia date of 330.7 ± 3.1 Ma ($MSWD_{(C+E)}$ = 1.4) (Fig. 11E).

4.3. Migmatites (samples MCE314, MCE330, MCE140b and MCE313b)

The cordierite bearing migmatite *MCE314* has been sampled in the Inner Pelvoux massif (Fig. 2). It is composed of quartz, K-feldspar, muscovite, chloritized biotite and pinitized cordierite. This sample exhibits a highly dipping and N140°E striking S_2 foliation defined by quartz aggregates and phyllosilicates. Subsolidus deformation is rare, and S_2 foliation is mainly a suprasolidus planar fabric. The alpine tectonics induced a low-grade retrogression as shown by chlorite around biotites, and sericite around K-feldspar. Unfortunately, because of alpine retrogression and strong pseudomorphosis of cordierite, pseudosection calculation was not possible. One may consider that cordierite-bearing migmatites are generally formed under low-pressure and high temperature conditions at ca. 0.4-0.6 GPa; 750-850 °C (Barbey et al., 1999; Kalt et al., 1999).

Monazite grains, located within the quartzo-feldspathic matrix, are not zoned and display heterogeneous U and Th contents (3437-10171 ppm and 5909-86534 ppm, respectively), relatively constant Pb content (1210-5516 ppm), and heterogeneous Th/U ratios (1.3-20.2) (Table S1). Despite this chemical heterogeneity, all analyses are concordant or sub-concordant (except jb7; Table S1), and yield a concordia date of 307.5 ± 1.9 Ma (n = 18; $\mathrm{MSWD}_{(C+E)} = 1.4$) (Fig. 11F).

The Roux migmatite *(MCE330)*, located in the Cortical Pelvoux, is a migmatitic gneiss developed at the base of the VSU (Fig. 2 and 4B). It is composed of quartz + K-feldspar + plagioclase + Biotite + Muscovite and is the equivalent of the Allemont migmatites from the SW Belledonne area (Fréville et al., 2018). The *MCE330* migmatite shows a N110°E40 solid-state protomylonitic foliation that erased syn-melting fabrics (Fig. 9F). The preferred orientation of mica and quartz-feldspar aggregates defines S-C fabrics that we attribute to D_3. The CL images of the analysed zircon grains show inherited cores with a typical magmatic concentric oscillatory zoning and metamorphic rims (Fig. S1). Zircon cores and rims have similar U and Pb contents ranging between 247-2605 ppm and 12-140 ppm, respectively (Table S1). Thirty analyses have been performed on 30 zircon grains (Fig. 13A). In the Tera-Wasserburg diagram, analyses mainly cluster into two groups. The first one, includes 13 concordant analyses on zircon cores, indicate a late Neoproterozoic age of crystallization. Among them 9 analyses yield a concordant date at 590.6 ± 6.2 Ma ($\mathrm{MSWD}_{(C+E)} = 0.95$). Two zircon cores show concordant and sub-concordant dates at ca. 1700 Ma and 1800 Ma (Fig. 13A), and two single analyses yield concordant dates at ca. 405 and 380 Ma. The second cluster includes 12 analyses performed on zircon rims and yields a concordia date at 330.5 ± 3.1 Ma ($\mathrm{MSWD}_{(C+E)} = 0.92$) (Fig. 13A).

The Etages migmatite *(MCE140b)*, located in the Inner Pelvoux, forms the country rock of the Etages granite (Fig. 2 and 4A). Composed of chloritized biotite, feldspars and quartz this rock shows a slight C_2 orientation, and it was also superimposed by a low-temperature alpine deformation (Fig. 4A). Euhedral zircon crystals with elongated shapes present oscillatory zonings in CL (Fig. S1). Twenty-eight zircon grains were analysed and they form two age groups (Fig. 13B). The first one is composed of four analyses forming a concordant cluster with low U, Pb and Th contents and Th/U ratios ranging from 0.08 to 0.5 (Table S1), that yields a concordant date at 317 ± 3.6 Ma ($MSWD_{(C+E)}$ = 0.38) (Fig. 13B). The second group is composed of 22 analyses with higher U, Pb and Th contents than the first group, but with similar Th/U ratios ranging from 0.06 to 0.5 (Table S1). Among this group, numerous analyses show lead loss (Fig. 13B) but ten analyses define a concordant date at 297.8 ± 2.1 Ma ($MSWD_{(C+E)}$ = 0.66) (Fig. 13B). In addition, one analysis shows a concordant date at ca. 460 Ma.

The Peyre-Arguet cordierite-bearing migmatite *(MCE313b)* displays a C'_2 foliation along which the cordierite grains are aligned. Zircon grains display patchy and oscillatory zoning (Fig. S1). Nineteen grains have been analysed and they broadly scatter along the Concordia between 650 and 280 Ma. The most abundant age population is defined by 12 analyses ranging from 481 to 419 Ma with low U (292-1043 ppm) and Pb (19-66 ppm) contents (Table SE1). Among this group, 7 analyses yield a concordant date of 451.4 ± 5.2 Ma ($MSWD_{(C+E)}$ = 0.66) (Fig. 13C).

4.4. Peyre-Arguet garnet amphibolite (sample MCE304v2)

The Peyre-Arguet meta-mafic (*MCE304v2*) is a garnet-bearing amphibolite from the Inner Pelvoux (Fig. 2) that consists of an amphibole, quartz, plagioclase and garnet assemblage that recorded D_2 deformation. Relics of clinopyroxene have been described by Barféty et al. (1982) and Jacob et al. (2022). Rutile grains are included within garnet and are replaced by ilmenite in the matrix. Garnet grains are surrounded by plagioclase-amphibole coronas. CL images of zircon included in garnet cores show cores with concentric oscillatory zoning surrounded by near homogeneous rims (Fig. S1). Zircon cores have high U (102-1349 ppm) and Pb (6.8-89.6 ppm) contents compared to rims (U: 3-72 ppm; Pb: 0.1-3.3 ppm) (Table SE1). Twenty-nine analyses have been performed on 29 zircon grains that define two clusters (Fig. 13D). The first one, composed of 12 concordant analyses from zircon cores, yields a concordant date at 471.3 ± 5 Ma ($MSWD_{(C+E)}$ = 1.06; n =11) (Fig. 13D). The second cluster is formed by 11 analyses performed on zircon rims that define a lower intercept at 329.6 ± 9.2 Ma (MSWD = 0.85). Among them, 8 analyses yield a concordant date at 326.9 ± 9.1 Ma (MSWD = 0.85) (Fig. 13D). Several analyses show concordant dates at ca. 379, 385, 409 and 432 Ma, which probably reflect a mixture between an old core (~ 470 Ma) and a younger rim (~ 327 Ma) and are probably therefore without geological meaning.

5. Discussion

5.1. *Pre-Variscan history*

Inherited dates at 451.4 ± 5.2 Ma and 460 ± 10 Ma were obtained from magmatic zircon grains of the Peyre-Arguet and Etages migmatites (samples *MCE313b* and *MCE140b*; Fig. 13; Table S1). This Ordovician record is interpreted as the emplacement age of felsic laccoliths, i.e. the protolith of orthogneisses. Numerous orthogneiss-derived from Ordovician protoliths are well documented in the entire Variscan belt (e.g. Melleton et al., 2010; Lardeaux et al. 2014) as within the ECMs (e.g. Schaltegger, 1993; Sergeev and Steiger, 1993; Bussy and von Raumer, 1994; Bussy et al., 2011; Bussien Grosjean et al., 2017). Even though a continental magmatic arc setting is sometimes suggested, presently, the preferred interpretation for the Ordovician magmatism is rather a rifting episode related to the opening of the Variscan oceans (e.g. Von Raumer et al., 1999, Von Raumer et al., 2013; Vanderhaeghe et al., 2020).

Similarly, the magmatic zircon cores from the Peyre-Arguet amphibolite (sample *MCE304v2*) display an inherited date of 471.3 ± 5 Ma that likely represents the intrusion age of a mafic protolith during the Ordovician crustal thinning, in agreement with inheritance recorded in other metabasites from the ECMs (Paquette et al., 1989; Oberli et al., 1994; Rubatto et al., 2001; Bussy et al., 2011; Jacob et al., 2021, 2022; Vanardois et al., 2022).

Older detrital and inherited zircon ages from pre-Neoproterozoic to Cambrian were also obtained (Fig. 13). Lack of Mesoproterozoic dates (>1500 Ma; Fig. 13A) point to a Gondwan~~a~~ian origin, i.e. the West African Craton (e. g. Melleton et al., 2010; Linnemann et al., 2014; Gärtner et al., 2017), and NE Africa-Arabia, Baltica and Amazonia (Stephan et al., 2019) as possible source regions. In the Cortical Pelvoux, the Roux migmatite (*MCE330*) did not record any Ordovician inheritance, but magmatic zircon cores rather indicate a Neoproterozoic magmatism at 590.6 ± 6.2 Ma (Fig. 13A). The Roux migmatite did not originate from the partial melting of an Ordovician intrusive protolith but from that of a metasedimentary protolith probably related to Pan-African (750-600 Ma) or Cadomian (590-540 Ma) orogeneses (Linneman et al., 2014). Similar metasedimentary rocks in the SW Belledonne display inherited zircons at ca. 590 Ma (Fréville et al., 2018). These Pan-African and Cadomian inherited zircon ages are common in the South-Western Variscan belt (e.g. Roger et al., 2004; Melleton et al. 2010; Schnaperelle et al., 2020) with a possible source region linked to the north-eastern Gondwana margin (Linnemann et al., 2014; Couzinié et al., 2014; Von Raumer et al., 2015; Chelle-Michou et al., 2017).

5.2. Carboniferous crustal thickening (D_1 deformation)

The mineral assemblage Qtz + Bt + Ms + Pl + Grt + Ky + St from sample *MCE339v* defines a large stability field with P-T conditions lower than 0.75 GPa and 625 °C (Fig. 13C). A set of old monazite grains, some being included in kyanite, yield a concordant date at 346.6 ± 4.8 Ma that gives a time constraint for prograde metamorphism (Fig. 16b). In the sample *MCE338*, the main assemblage Qtz + Ms + Bt + Pl + Grt + Sill (Fig. 11D) gives P-T conditions between 550-700 °C and 0.35-0.80 GPa (Fig. 16a). The highest Qcmp factors for muscovite and biotite give a P-T refinement at ca. 0.6 GPa and 650 °C (Fig. 16a). Garnet grains are also a part of the mineral assemblage and mark the same planar fabric than micas (Fig. 11D), but their core compositions are best modelled at lower-grade conditions (0.45 GPa and 575 °C; Fig. 14c). Garnet core shows a perfect homogeneous composition (Fig. 14A) that might be the result of diffusion process, which could explain the lower grade metamorphic conditions defined by the garnet core composition. Garnet rim composition yields P-T conditions at 0.35 GPa and 450 °C (Fig. 14c). The mineral composition modelling highlights a retrograde P-T path from the peak of metamorphism at ca. 0.6 GPa and 650 °C to the end of the retrograde path at 0.35 GPa and 450 °C (Fig. 16a). In the corresponding sample (*MCE338*), monazite grains are often localized within biotite-muscovite layers (Fig. 11F) and yield a concordant date of 332.2 ± 1.6 Ma (Fig. 12D), which is therefore interpreted as the age of the peak of M_1 metamorphism. These two samples present near similar P-T paths (Fig. 16c) with metamorphic conditions slightly higher in the sample *MCE338*, which is consistent with its deeper position into the crust (see Fig. 4B).

In sample *MCE339v*, the relictual S_1 foliation preserved in garnet and kyanite is dated by monazite at 346.6 ± 4.8 Ma. Similarly, the S_1 foliation in the sample *MCE338* is defined by the alignment of micas and by the orientation of monazite and is dated at 332.2 ± 1.6 Ma. Similar ages are obtained in samples *MCE379*, *MCE382b* and *MCE328* with a main S_1 foliation with syn-kinematic monazite grains (Fig. 10, 11 and 12). These results indicate that a D_1 deformation was active at ca. 345-330 Ma (Fig. 16d).

A similar D_1/M_1 event is documented in the SW Belledonne area with the well-preserved low angle S_1, holding a E-W trending L_1 stretching lineation, interpreted as due to an eastward nappe stacking event responsible for crustal thickening coeval with the barrovian metamorphism (M_1) (Fernandez et al., 2002; Guillot et al., 2009; Guillot and Ménot, 2009; Fréville et al., 2018). In SW Belledonne massif, the peak of M_1 metamorphism is dated on monazite (LA-ICP-MS) and zircon (SIMS) at around 337 ± 7 Ma and 338 ± 5 Ma respectively (Fig. 16d; Fréville et al., 2018). The D_1/M_1 barrovian evolution culminated with the partial melting as observed at the bottom of the VSU in the Cortical Pelvoux and SW Belledonne (Gidon et al., 1980; Barféty et al., 1988; Guillot et al., 2009; Fréville et al. 2018; this study) as exemplified by the "Roux migmatite" that yields a similar concordant age at 330 ± 3 Ma (Fig. 13A) obtained on metamorphic rims of zircons (sample *MCE330* in this study).

The deposition age of the SW Belledonne VSU is dated at 352 ± 1 Ma from a plagioclase-rich leucocratic sill (Fréville et al., 2018). Based on the lithological similarities of these volcano-sedimentary rocks in SW Belledonne and Cortical Pelvoux, we propose that the volcano-sedimentary rocks of the Cortical Pelvoux deposited during the late-Devonian early-Carboniferous rifting and therefore predated the D_1 crustal thickening.

Retrogressed eclogites and HP granulites are well documented in others ECMs (e.g. Albrecht et al., 1991; Von Raumer and Bussy, 2004; Ferrando et al., 2008; Jouffray et al., 2020; Jacob et al., 2021; Vanardois et al., 2022) and yield zircon and rutile ages at ca. 340-330 Ma (Rubatto et al., 2010; Vanardois et al., 2022). Recently, M_1 high-pressure peak condition recorded within retrograded eclogites of the NE Belledonne and Inner Pelvoux was constrained at ca. 340-330 Ma (Jacob et al., 2021, 2022). In the Inner Pelvoux, the Peyre-Arguet mafic HP granulite (Barféty et al., 1982) recorded a metamorphic age at 326.9 ± 9.1 Ma (Fig. 13D), confirming that a D_1/M_1 crustal thickening event at 350-330 Ma is recorded in both the Pelvoux and Belledonne massifs (Fig. 16e). Consistently, the sub-horizontal magmatic foliation we recognized in the Rochail granite and dated at 343 ± 11 Ma age (Guerrot and Debon, 2000) is interpreted as a S_1 foliation that resulted from crustal thickening.

5.3. Sinistral transpression and longitudinal flow (D_2 and D_3 deformations)

In the Cortical Pelvoux, the D_2 tectono-metamorphic event corresponds to a NW-SE shortening responsible for folding of the S_1 and formation of the N30°E striking S_2 foliation, also documented in the SW Belledonne (Fréville et al., 2018), in the course of D_1 contraction. In sample *MCE339v*, from the central part of the Cortical Pelvoux, the S_2 foliation is defined by the preferential alignment of biotite for which the highest Qcmp factor indicates temperature conditions above 525 °C and allows us to refine the P-T condition of biotite-bearing S_2 foliation at around 0.5 GPa and 550 °C near the kyanite-sillimanite transition (Fig. 13D). Monazite grains included in the biotite-layers (Fig. 11C) yield an age at 319.2 ± 6.1 Ma (Fig. 11C) providing a time constraint for D_2 transpression (Fig. 16b).

In the Inner Pelvoux, D_2 structures are ubiquitous with the development of penetrative and steeply dipping planar surfaces, such as the S_2 foliation, and C_2-C'_2 sinistral shear zones, and weakly plunging lineations formed under sinistral strike-slip regime (Fig. 17A). The syn-D_2 cordierite-bearing migmatite *MCE314* shows U-Th-Pb data obtained on monazite grains that form a cluster with an intercept at 307.5 ± 1.9 Ma (Fig. 11F). It suggests that the partially molten crust was under high temperature and low-pressure conditions at ca. 308 Ma (Fig. 16c), giving another time constraint for the D_2 deformation. In the Etages migmatite (*MCE140b*), four zircon grains yield a concordant date at 317 ± 4 Ma (Fig. 13B) that we also relate to the D_2 transpression. The Etages migmatite *MCE140b* also gives a concordant date at 297.8 ± 2.1 Ma, like the age of the Etages and the Bérarde-Promontoire syn-D_2 plutons (this study; Strzerzynski et al., 2005) dated at ca. 303-299 Ma (Fréville, 2016). Hence, we propose that the timing of the D_2 transpression ranged from at least ca. 320 Ma to 298 Ma (Fig. 16d), but it might have started as early as 330 Ma (Fig. 16e). In the SW and NE Belledonne massif, the onset of the D_2 transpression with the development of S_2 occurred after the peak of pressure at 330 Ma (Fréville et al., 2018; Jacob et al., 2021), a period that corresponds to the onset of partial melting in the lower crust. In both Pelvoux and Belledonne massifs, the transpression is more pervasive in the anatectic crust (Fréville et al., 2018; this study). Melt-enhanced strength drop may have impacted stress distribution and initiated transpressional strain in the deep crust with the preferential appearance of the steeply dipping S_2 cleavage in the partially molten middle-lower crust, while NW-SE contraction was accommodated by upright to SE-verging D_2 folding in the upper-middle crust (Fig. 17).

Near the anatectic front, we have recognized a S_3 sub-horizontal planar fabric affecting the former S_1 and S_2 foliations (Fig. 8, 9 and 17). In sample *MCE382b* located in the Cortical Pelvoux, 4 monazite grains included in undeformed biotite marking the S_3 foliation (Fig. 10G and H) yield a concordant date at 306 ± 3.5 Ma (Fig. 11B). The record of the D_3 deformation in monazite is probably dependent on D_3 strain localization. Thus, we propose that the ca. 306 Ma age is a reliable one for the D_3 deformation in the Cortical Pelvoux (Fig. 16d). Our results suggest that during the Late Carboniferous, the D_2 and D_3 deformations were partly synchronous (Fig. 16d) and therefore attest for strain partitioning during a same tectonic event responsible for longitudinal flow of the middle-lower crust. We interpret the top-to-the NW shearing along S_3 as a local accommodation of a southeastward horizontal flow of the partially molten lower crust during sinistral transpression. Recently, Jacob (2022) and Jacob et al. (2022) also show that in the central Inner Pelvoux (La Lavey area) the S_1 foliation is reworked by a syn-migmatitic flat-lying foliation showing evidence for a NW-SE, i.e. N150-N180 directed horizontal flow. These authors argue that the horizontal flow was coeval with a sinistral shearing along a N140-N170 directed high-strain corridor (D_2) characterized by a vertical shortening of the D_2 planar fabrics by the syn-magmatic flat-lying foliation. This is consistent with our own field observations of the S_3 foliation, made in the same La Meije block, a few kilometers to the SE (Fig. 3). The contemporaneity between NW-SE directed transpressional flow and vertical shortening in that part of the la Meije block is supported by our radiometric data of D_2 and D_3 and attests for strain partitioning between the suprastructure and infrastructure during horizontal crustal flow under transpressive regime as commonly described in the Variscan belt (Aguilar et al., 2014; Cochelin et al., 2017, 2021; Rabin et al., 2015; Trap et al., 2017).

5.4. Kinematic flow at the scale of the EVSZ

At large scale, the shape and strike of the EVSZ and how it connects to other major shear zones of the Variscan belt framework is not straightforward (e.g. Ballèvre et al., 2018; Chardon et al., 2020; Simonetti et al., 2020a). In most of previous studies, the authors proposed that the EVSZ runs from the Aar-Gothard, Aiguilles-Rouges-Mont-Blanc, Belledonne massifs, and to the Argentera, Maures-Tanneron and Corsica-Sardinia massifs with a main trend that changes from NE-SW to N-S respectively (Fig. 1; e.g. Guillot et al., 2009; Padovano et al., 2012; Duchesne et al., 2013; Simonetti et al., 2020a) that consider a post-Variscan counterclockwise rotation of the Argentera massif of about 90° that is not recorded within the Permian sedimentary cover (Bogdanoff and Schott, 1977; Sonnette et al., 2014). The major rotational movements described in the internal Alps are accommodated by transcurrent faults that did not affect the ECMs (Collombet et al., 2002). Any rotation of the Argentera massif may have occurred prior to the deposition of Permian sedimentary rocks deposits and at these times the rotation in the southeastern part of the Variscan belt is clockwise (Edel et al., 2014, 2015). Following the work of Edel et al. (2014, 2018) that consider the rotation of the Maures-Tanneron - Corsica -Sardinia block, we propose an alternative geometry for the EVSZ with the individualization of several branches forming the anastomosed network (Fig. 18).

The large-scale transpression is a strain feature the whole ECMs have in common, with a general dextral kinematics (Von Raumer et al., 1999; Von Raumer and Bussy, 2004; Simonetti et al., 2018, 2020a; Jacob et al., 2021) except in the Pelvoux massif where it is sinistral (this study, Strzerzynski et al., 2005; Jacob et al., 2022). Our results argue that the sinistral shearing in the Pelvoux massif was active between at least ca. 320 and 300 Ma. Similar ages have been reported for the dextral transpressional shearing in the Aiguilles-Rouges - Mont-Blanc massifs (Simonetti et al., 2020a; Vanardois, 2021), in the Argentera massif (Sanchez et al., 2011; Simonetti et al., 2018, 2021), in the Maures-Tanneron massifs (Rolland et al., 2009; Corsini and Rolland, 2009), in Sardinia and Corsica (Giacomini et al., 2008; Carosi et al., 2012). Since dextral and sinistral shearing were synchronous, we propose that at the scale of the ECMs, the sinistral shearing in the Pelvoux massif corresponds to an antithetic domain within the dextral dominated shear zone network (Fig. 18). During the Late Carboniferous times, the average antithetic C’ shear zone strikes N140-150E in the Pelvoux massif while dextral shear zones trends ca. N30E in the Aiguilles-Rouges-Mont-Blanc massif and Belledonne massif (e.g. Simonetti et al., 2020, Jacob et al., 2021). Vanardois (2021) argue that N30E directed dextral deformation in the Aiguilles-Rouges Massif (Fig. 18) corresponds to 1-2 km wide synthetic C’ shear zones in a regional-scale (> 10km) N-S directed shear zone system. The strain pattern of the Aiguilles-Rouges massif is made of a S-C-C’ dextral framework with NW-SE-directed S planes, N-S directed C planes and N30E directed C’ planes (Fig. 18; Vanardois 2021). In that scheme, the average obtuse angle between synthetic C’ and antithetic C’ shear direction might be around 105 ± 10° (Fig. 18) that is consistent with geometry and flow kinematics of a typical ductile shear zone (Fossen et al., 2012; Gillam et al., 2013) even if anticlockwise back-rotation between NE-SW dextral corridors is considered.

Conclusions

Our field work, structural, thermobarometric, and geochronological results argue that the Belledonne and Pelvoux massifs share the same Carboniferous tectono-metamorphic evolution. The Belledonne-Pelvoux area experienced a D_1 event related to crustal thickening during the Eastward nappe stacking event in response to E-W to NW-SE contraction. The D_1/M_1 episode ended with the onset of crustal partial melting at ca. 650°C during Late Visean time. Ongoing NW-SE bulk shortening is responsible for sinistral D_2 shearing in the partially molten middle-lower crust (i.e. Inner Pelvoux) with the strain partitioning between C and C’ shear zones and horizontal longitudinal flow in the range 330-300 Ma. Field and radiometric data argue for contemporaneity between D_2 and D_3 and attest for vertical strain partitioning between the suprastructure and infrastructure during horizontal crustal flow and strike-slip shearing, as commonly described in the Variscan belt. Within the orogen scale dextral East-Variscan Shear Zone, the sinistral transpression recorded in the Pelvoux massif corresponds to an antithetic strain domain. The data presented in this paper on the East Variscan Shear Zone exposed in the Belledone-Pelvoux massifs, should be compared to other late-Variscan shear zones in order to check for kinematic compatibility and to reconstruct plate-scale kinematics during late carboniferous time.

Acknowledgments.

The authors thank the Institut des Sciences de la Terre d'Orléans (ISTO), BRGM, the Laboratoire Chrono-Environnement, and the Observatoire des Sciences de l'Univers en Région Centre (OSUC) for their financial support. We also gratefully acknowledge the French RENATECH network and its FEMTO-ST technological facility that partly supports this work. We thank Laurent Jolivet and Olivier Vanderhaeghe for their comments and editorial work. The constructive and helpful reviews by Julien Berger and Yann Rolland are acknowledged with thanks.

References:

Abrecht J, Biino G. G, Mercolli I, Stille P. 1991. *M*afic-ultramafic rock associations in the Aar, Gotthard and Tavetsch massifs of the Helvetic domain in the Central Swiss Alps: markers of ophiolitic pre-Variscan sutures, reworked by polymetamorphic events? *Schweiz. Mineral. Petrogr. Mitt.* 71:295–300.

Aguilar, C., Liesa, M., Castiñeiras, P., & Navidad, M. (2014). Late Variscan metamorphic and magmatic evolution in the eastern Pyrenees revealed by U–Pb age zircon dating. Journal of the Geological Society, 171(2), 181-192.

Alcock, J. E., Catalán, J. R. M., Pascual, F. J. R., Montes, A. D., Fernández, R. D., Barreiro, J. G., ... & Clavijo, E. G. (2015). 2-D thermal modeling of HT–LP metamorphism in NW and Central Iberia: Implications for Variscan magmatism, rheology of the lithosphere and orogenic evolution. Tectonophysics, 657, 21-37

Autran A, Cogné J. 1980. La zone interne de l'orogène varisque dans l'ouest de la France et sa place dans le développement de la chaîne hercynienne. *Géologie Eur. 26° CGI Paris Mém. BRGM* 108:90–111.

Ballèvre M, Manzotti P, Dal Piaz GV. 2018. Pre-Alpine (Variscan) inheritance: A key for the location of the future Valaisan Basin (Western Alps). *Tectonics* 37:786–817.

Barbey P, Marignac C, Montel JM, Macaudière J, Gasquet D, Jabbori J. 1999. Cordierite Growth Texture and the Conditions of Genesis and Emplacement of Crustal Granitic Magmas: the Velay Granite Complex (Massif Central, France). *J. Petrol.* 40:1425–1441.

Barbey, P., Villaros, A., Marignac, C., & Montel, J. M. 2015. Multiphase melting, magma emplacement and PT-time path in late-collisional context: the Velay example (Massif Central, France). Bulletin de la Société géologique de France, 186(2-3), 93-116.

Barfety JC, Gidon M, Ménot RP, Debon F, Pêcher S, Guillot S, Fourneaux JC, Gamond JF. 2000. Notice de la carte géologique de la France, feuille Domène (773), scale 1:50 000. Orléans : BRGM.

Barfety JC, Montjuvent G, Pécher A, Carme F, 1988. Notice de la carte géologique de la France, feuille La Mure (821), scale 1:50 000. Orléans : BRGM.

Barfety JC, Pécher A, Vivier G, Demeulemeester P, Poulain PA, Vernet J, Fourneaux JC, Bambier A. 1982. Notice de la carte géologique de la France, feuille St-Christophe-en-Oisans (822), scale 1:50 000. Orléans : BRGM.

Bellahsen N, Mouthereau F, Boutoux A, Bellanger M, Lacombe O, Jolivet L, Rolland Y. 2014. Collision kinematics in the western external Alps. *Tectonics* 33: 2013TC003453. https://doi.org/10.1002/2013TC003453

Bellanger M, Augier R, Bellahsen N, Jolivet L, Monié P, Baudin T, Beyssac O. 2015. Shortening of the European Dauphinois margin (Oisans Massif, Western Alps): New insights from RSCM maximum temperature estimates and 40Ar/39Ar in situ dating. *J. Geodyn.* 83:37–64. https://doi.org/10.1016/j.jog.2014.09.004

Bellanger M, Bellahsen N, Jolivet L, Baudin T, Augier R, Boutoux A. 2014. Basement shear zones development and shortening kinematics in the Ecrins Massif, Western Alps. *Tectonics* 33:84–111.

Bellot JP. 2005. The Palaeozoic evolution of theMauresMassif (France) and its potential correlation with other areas of the Variscan belt: a review. *J. Virtual Explor.* 19:1–24.

Bodinier JL, Dupuy C, Dostal J, Carme F. 1981. Geochemistry of Ophilolites from Chamrousse Complexe (Belledonne Massif, Alps). *Contrib Miner. Pet.* 78:379–388.

Bogdanoff S, Menot R.P, Vivier G. 1991. Les Massifs cristallins externes des Alpes occidentales francaises, un fragment de la zone interne varisque. Extern. Cryst. Massifs Fr. West. Alps Part Intern. *Variscan Zone* 44:237–285.

Bordet P, Bordet C. 1963. Belledonne-Grande Rousses et Aiguilles Rouges Mont Blanc: quelques données nouvelles sur leurs rapports structuraux. -Livre à la mémoire du professeur Fallot.-. *Mém. Hors Sér. Société Géologique Fr.* 1:309–316.

Boutoux A, Bellahsen N, Lacombe O, Verlaguet A, Mouthereau F. 2014. Inversion of pre-orogenic extensional basins in the external Western Alps: Structure, microstructures and restoration. *J. Struct. Geol.* 60:13–29.

Bruguier O, Bosch D, Caby R, Vitale-Brovarone A, Fernandez L, Hammor D, Laouar R, Ouabadi A, Abdallah N, Mechati M. 2017. Age of UHP metamorphism in the Western Mediterranean : insight from rutile and zircon inclusions in a diamond-bearing garnet magacryst (Edough Massif, Algeria). *Earth Planet. Sci. Lett.* 474:215-225.

Bussy F, von Raumer JF. 1994. U–Pb geochronology of Palaeozoic magmatic events in the Mont-Blanc Crystalline Massif, Western Alps. *Schweiz. Mineral. Petrogr. Mitt.* 74:514–515.

Bussy F, Péronnet V, Ulianov A, Epard JL, von Raumer J. 2011. Ordovician magmatism in the External French Alps: witness of a peri-Gondwanan active continental margin. In Gutiérrez-Marco JC, Rábano I, García-Bellido D, Eds. The Ordovician of the World: Madrid, Instituto Geológico y Minero de España, Cuadernos del Museo Geominero, v. 14, p. 75–82.

Carme F. 1970. Age briovérien probable de la majeure partie des séries supposées dévono-dinantiennes et existence d'un cycle ororgénique anté-hercynien, sans doute cadomien, dans la chaîne de Belledonne (Alpes Française). *C R Acad Sc Paris* 271:631–633.

Carme F. 1965. Sur deux formations, d'origine volcanique, des schistes cristallins anté-houillers de la chaîne de Belledonne (Alpes Francaise). *C R Acad Sc Paris* 260:6401–6404.

Chardon D, Aretz M, Roques D. 2020. Reappraisal of Variscan tectonics in the southern French Massif Central. *Tectonophysics* 787:228477.

Carosi R, Montomoli C, Tiepolo M, Frassi C. 2012. Geochronological constraints on post-collisional shear zones in the Variscides of Sardinia (Italy). *Terra Nova* 24:42–51.

Chelle-Michou C, Laurent O, Moyen JF, Block S, Paquette JL, Couzinié S, Gardien V, Vanderhaeghe O, Villaros A, Zeh A. 2017. Pre-Cadomian to late-Variscan odyssey of the eastern Massif Central, France: Formation of the West European crust in a nutshell. *Gondwana Res*. 46:170-190.

Cochelin B, Chardon D, Denèle Y, Gumiaux C, Le Bayon B. 2017. Vertical strain partitioning in hot Variscan crust: Syn-convergence escape of the Pyrenees in the Iberian-Armorican syntax. *Bull. Soc. Geol. Fr.* 188.

Cochelin B, Lemirre B, Denèle Y, de Saint Blanquat M. 2021. Strain partitioning within bending orogens, new insights from the Variscan belt (Chiroulet-Lesponne domes, Pyrenees). *Tectonics* 40, e2020TC006386.

Collombet, M., Thomas, J. C., Chauvin, A., Tricart, P., Bouillin, J. P., & Gratier, J. P. (2002). Counterclockwise rotation of the western Alps since the Oligocene: New insights from paleomagnetic data. Tectonics, 21(4), 1032.

Compagnoni R, Ferrando S, Lombardo B, Radulesco N, Rubatto D. 2010. Paleo-European crust of the Italian Western Alps: Geological history of the Argentera Massif and comparison with Mont Blanc-Aiguilles Rouges and Maures-Tanneron Massifs. *J. Virtual Explor.* 36: https://doi.org/10.3809/jvirtex.2010.00228

Connolly JA. 2005. Computation of phase equilibria by linear programming: A tool for geodynamic modeling and its application to subduction zone decarbonation. *Earth Planet. Sci. Lett.* 236: 524–541.

Connolly J.A, Pettrini K. 2002. An automated strategy for calculation of phase diagram sections and retrieval of rock properties as a function of physical conditions. *J. Metamorph. Geol.* 20: 697–708.

Corsini M, Rolland Y. 2009. *L*ate evolution of the southern European Variscan belt: Exhumation of the lower crust in a context of oblique convergence. *C. R. Geosci.* 341:214–223.

Couzinié S, Moyen JF, Villaros A, Paquette JL, Scarrow JH, Marignac C. 2014. Temporal relationships between Mg-K mafic magmatism and catastrophic melting of the Variscan crust in the southern part of Velay Complex (Massif Central, France). *J Geosci* 59:1-18.

Debon F, Lemmet M. 1999. Evolution of Mg/Fe Ratios in Late Variscan Pultonic Rocks from the External Crystalline Massif of the Alps (France, Italy, Switzerland). J. Petrol. 40:1151–1185.

Duchesne, J. C., Liégeois, J. P., Bolle, O., Vander Auwera, J., Bruguier, O., Matukov, D. I., & Sergeev, S. A. (2013). The fast evolution of a crustal hot zone at the end of a transpressional regime: The Saint-Tropez peninsula granites and related dykes (Maures Massif, SE France). Lithos, 162, 195-220.

Duesterhoeft E, Lanari P, 2020. Iterative thermodynamic modelling—Part 1: A theoretical scoring technique and a computer program (Bingo-Antidote). J Metamorph Geol 8:527–551.

Edel, J. B., Schulmann, K., Lexa, O., & Lardeaux, J. M. (2018). Late Palaeozoic palaeomagnetic and tectonic constraints for amalgamation ofPangea supercontinent in the European Variscan belt. Earth-Science Reviews,177, 589–612. https://doi.org/10.1016/J.EARSCIREV.2017.12.007

Faure M, Mezeme E.B, Duguet M, Cartier C, Talbot JY. 2005. Paleozoic tectonic evolution of medio-europa from the example of the french massif central and massif armoricain. *J. Virtual Explor.* 19: Paper 5.

Faure M., Rossi P., Gaché J., Melleton J., Frei D, Li X., Lin W. 2014. Variscan orogeny in Corsica: New structural and geochronological insights, and its place in the Variscan geodynamic framework. Int. J. Earth Sci. (Geol Rundsch) DOI 10.1007/s00531-014-1031-8.

Faure M., Ferrière J. 2022. Reconstructing the Variscan terranes in the Alpine basement: facts and arguments for an Alpidic orocline. Geosciences, 12, in press

Fernandez A, Guillot S, Ménot R.P, Ledru P. 2002. Late Paleozoic polyphased tectonics in the SW Belledonne massif (external crystalline massifs, French Alps). *Geodin. Acta* 15:127–139.

Ferrando S, Lombardo B, Compagnoni R. 2008. Metamorphic history of HP mafic granulites from the Gesso-Stura Terrain (Argentera Massif, Western Alps, Italy). *Eur. J. Mineral.* 20:777–790. https://doi.org/10.1127/0935-1221/2008/0020-1891

Franke W. 2000. The mid-European segment of the Variscides: tectonostratigraphic units, terrane boundaries and plate tectonic evolution. *Geol. Soc. Lond. Spec. Publ.* 179:35–61.

Franke W, Cocks LRM, Torsvik TH, 2017. The Palaeozoic Variscan oceans revisited. *Gondwana Res* 48:257-284.

Fréville K, 2016. The variscan orogeny in the external crystalline massifs of Belledonne and Pelvoux (French Western Alps): the role of partial melting and plutonism on the structuration of the continental crust, (Doctoral dissertation). Orléans, France, Université de Orléans.

Fréville K, Trap P, Faure M, Melleton J, Xian-Hua L, Wei L, Blein O, Bruguier O, Poujol M. 2018. New structural, metamorphic and geochronological insights on the Variscan evolution in the Alpine Belledonne massif (France). *Tectonophysics* 726:14–42.

Fuhrman ML, Lindsley DH, 1988. Ternary-feldspar modeling and thermometry. *Am Mineral* 73:201-215.

Gärtner A, Youbi N, Villeneuve M, Sagawe A. 2017. *T*he zircon evidence of temporally changing sediment transport— the NW Gondwana margin during Cambrian to Devonian time (Aoucert and Smara areas, Moroccan Sahara). *Int. J. Earth Sci.* 106:2747–2769.

Gerbault M, Schneider J, Reverso-Peila A, Corsini M. 2018. Crustal exhumation during ongoing compression in the Variscan Maures-Tanneron Massif, France - geological and thermo-mechanical aspects. *Tectonophysics* 746:439–458.

Gibergy P. 1968. Découverte de “grès à trous” renfermant des schistes noirs de Valbonnais (série cristallophyllienne des Massifs Cristallins Externes dans les Alpes française). *C R Acad Sc Paris* 267:1251–1254.

Gidon M, Bonhomme J.-L, Fourneaux J.C, Monjuvent G. Mouterde R. 1980. Notice de la carte géologique de la France, feuille Saint-Bonnet (845), scale 1:50 000. Orléans : BRGM.

Gonçalves GO, Lana C, Scholz R, Buick IS, Gerdes A, Kamo SL, Corfu F, Marinho MM, Chaves AO, Valeriano C, Nalini A Jr. 2016. An assessment of monazite from the Itambé pegmatite district for as U-Pb isotope reference material for microanalysis and implications for the origin of the “Moacyr” monazite. *Chem. Geol.* 424:30-50.

Grandjean V, Guillot S, Pecher A. 1996. Un nouveau témoin de l’évolution métamorphique BP-HT post-orogénique hercynienne : l’unité de Peyre-Arguet (Haut-Dauphiné). *C. R. Acad. Sci. Sér. 2 Sci. Terre Planètes* 322:189–195.

Guerrot C, Debon F. 2000. U-Pb zircon dating of two contrasting Late Variscan plutonic suites from the Pelvoux massif (French Western Alps). *Schweiz. Mineral. Petrogr. Mitt.* 80:249–256

Guillot S, di Paola S, Ménot R.-P, Ledru P, Spalla M, Gosso G, Schwartz S. 2009. Suture zones and importance of strike-slip faulting for Variscan geodynamic reconstructions of the External Crystalline Massifs of the western Alps. B*ull Soc Géol Fr.* 180:483–500.

Guillot S. Ménot R.P. 2009. Paleozoic evolution of the External Crystalline Massifs of the Western Alps. *C R* Geosci. 341:253–265.

Henk A. 2000. Foreland-directed lower-crustal flow and its implications for the exhumation of high-pressure-high-temperature rocks. Geol. Soc. Lond. Spec. Publ. 179: 355–368. https://doi.org/10.1144/GSL.SP.2000.179.01.21

Jacob J.B. 2022 Quelle place pour les Massifs Cristallins Externes des Alpes occidentales dans l’orogenèse varisque? PhD Thesis. Université de Grenoble.

Jacob J.B, Guillot S, Rubatto D, Janots E, Melleton J, Faure M. 2021. Carboniferous high-pressure metamorphism and deformation in the Belledonne Massif (Western Alps). *J. Metamorph. Geol.* 39:1009-1044, doi:10.1111/jmg.12600.

Jacob JB, Janots E, Guillot S, Rubatto D, Fréville K, Melleton J, Faure M, 2022. HT overprint of HP granulites in the Oisans–Pelvoux massif: implications for the dynamics of the Variscan collision in the external Western Alps. doi.org/10.1016/j.lithos.2022.106650.

Jouffray F, Spalla M.I, Lardeaux J.M, Filippi M, Rebay G, Corsini M, et al. 2020. Variscan eclogites from the Argentera-Mercantour Massif (External Crystalline Massifs, SW Alps): a dismembered cryptic suture zone. *Int. J. Earth Sci.* 109: 1273–1294. https://doi.org/10.1007/s00531-020-01848-2.

Kalt A, Berger A, Blumel P. 1999. Metamorphic Evolution of Cordierite-Bearing Migmatites from the Bayerische Wald (Variscan Belt, Germany). J. Petrol. 40: 601–627.

Kretz R. 1983. Symbols of rock-forming minerals. Am. Mineral. 68:277–279.

Lardeaux JM, Schulmann K, Faure M, Janouzek V, Lexa O, Skrzypek E, Edel JB, Štípská P. 2014. The Moldanubian Zone in the French Massif Central, Vosges/Schwarzwald and Bohemian Massif revisited: differences and similarities. *Geol. Soc. Lond. Spec. Publ.* 405:7–44. https://doi.org/10.1144/SP405.14

Ledru, P., Courrioux, G., Dallain, C., Lardeaux, J. M., Montel, J. M., Vanderhaeghe, O., & Vitel, G. 2001. The Velay dome (French Massif Central): melt generation and granite emplacement during orogenic evolution. Tectonophysics, 342(3-4), 207-237.

Le Fort P. 1973. Géologie du Haut-Dauphiné cristallin (Alpes Française): Etudes pétrologique et structurale de la partie occidentale (Phd thesis). Université Nancy I.

Lemoine M. 1988. Des nappes embryonnaires aux blocs basculés : évolution des idées et des modèles sur l’histoire mésozoïque des Alpes occidentales. *G-Alp.* 8:787–797.

Lemoine M, Bas T, Arnaud-Vanneau A, Arnaud H, Dumont T, Gidon M, Bourbon M, de Graciansky P.-C, Rudkiewicz J.-L, Megard-Galli J, Tricart P. 1986. The continental margin of the Mesozoic Tethys in the Western Alps. Mar. *Pet. Geol.* 3:179–199.

Linnemann U, Gerdes A, Hofmann M, Marko L. 2014. The Cadomian Orogen: Neoproterozoic to Early Cambrian crustal growth and orogenic zoning along the periphery of the West African Craton-Constraints fromU-Pb zircon ages and Hf isotopes (Schwarzburg Antiform, Germany). *Precambrian Res.* 244: 236–278. https://doi.org/10.1016/j.precamres.2013.08.007.

Lombardo B, Colombo F, Compagnoni R, Ghiglione G, Rubatto D. 1997. Relics of pre-Variscan events in the Malinvern-Argentera Complex, Argentera Massif, Western Alps. *Quaderni di Geodinamica Alpina e Quaternaria* 4:66.

Manzotti P, Ballèvre M, Poujol M, 2016. Detrital zircon geochronology in the Dora-Maira and Zone Houillère: a record of sediment travel paths in the Carboniferous. *Terra Nova* 28:279-288.

Matte P. 1991. Accretionary history and crustal evolution of the Variscan belt in Western Europe. *Tectonophysics* 196:309–307.

Matte P. 2001. The varisacn collage and orogeny (480-290 Ma) and the tectonic definition of the Armorica microplate: a review. *Terra Nova* 13:122–128.

Matte P. 2007. Variscan thrust nappes, detachment, and strike-slip faults in the French Massi Central: Interpretation of lineations. *Geol. Soc. Am. Memoire* 200:391–402.

Melleton J, Cocherie A, Faure M, Rossi P. 2010. Precambrian protoliths and Early Paleozoic magmatism in the French Massif Central: U–Pb data and the North Gondwana connection in the west European Variscan belt. *Gondwana Res* 17:13-25.

Ménot RP. 1988a. An overview of the geology of the Belledonne Massif (External Crystalline Massifs of western Alps). *Schweiz Miner. Petrogr Mitt* 70:33–53.

Ménot RP. 1988b. Magmatisme paléozoïque et structuration carbonifère du massif de Belledonne (Alpes françaises). Contraintes nouvelles pour les schémas d'évolution de la chaîne varisque Ouest-Européenne. *Mémoire et documents du centre armoricain d'étude structurale des socles*. Rennes.

Ménot RP. 1987. Magmatismes et structuration orogénique Paléozoïques de la Chaîne de Belledonne (Massifs cristallins externes alpins). Le Domaine Sud - Occidental. *G-Alp.* 63: 55–93.

Oberli F, Meier M, Biino GG. 1994. Time constraints on the pre-Variscan magmatic/metamorphic evolution of the Gotthard and Tavetsch units derived from U-Pb results. *Schweiz. Mineral. Petrogr. Mitt.* 74:483–488.

Padovano M, Elter F.M, Pandeli E, Franceshelli M. 2012. The East Variscan Shear Zone: new insights into its role in the Late Carboniferous collision in southern Europe. *Int. Geol. Rev.* 54: 957–970.

Padovano M, Dörr W, Elter FM, Gerdes A. 2014. The East Variscan Shear Zone: Geochronological constraints from the Capo Ferro area (NE Sardinia, Italy). *Lithos* 196–197:27–41.

Paquette JL, Ménot RP, Peucat JJ. 1989. REE, Sm-Nd and U-Pb zircon study of eclogites from the Alpine External Massifs (Western Alps)" evidence for crustal contamination. *Earth Planet. Sci. Lett.* 96:181–198.

Paris F. Robardet M. 1990. Early Palaeozoic palaeobiogeography of the Variscan regions. *Tectonophysics* 1977:193–213.

Pecher A. 1970. Etude pétrographique de la partie orientale du massif des Ecrins-Pelvoux: le socle ancien - Alpes françaises. (Thesis). Faculté des Sciences de l'Université de Grenoble, pp 151.

Pecher A, Vialon P. 1970. Présence de gneiss du "faciès granulite" dans le noyau précambrien du massif des Ecrins-Pelvoux (Alpes du Dauphiné, France). *C R Acad Sc Paris* 270:666–668.

Pin C, Carme F. 1987. A Sm-Nd isotopic study of 500 Ma old oceanic crust in the Variscan belt of Western Europe: the Chamrousse ophiolite complex, Western Alps (France). *Contrib. Mineral. Petrol.* 96:406–413.

Poitrasson F, Chenery SR, Shepherd TJ, 2000. Electron microprobe and LA-ICP-MS study of monazite hydrothermal alteration: implications for U-Th-Pb geochronology and nuclear ceramics. *Geochim Cosmochim Acta* 64:3283-3297

Rabin M. Trap P, Carry N, Fréville K, Cenki-Tok B, Lobjoie C, Goncalves P, Marquer D. 2015. Strain partitioning along the anatectic front in the Variscan Montagne Noire massif (southern French Massif Central). *Tectonics* 34: 2014TC003790. https://doi.org/10.1002/2014TC003790

Roger F, Respaut JP, Brunal M, Matte P, Paquette JL. 2004. Première datation U–Pb des orthogneiss oeillés de la zone axiale de la Montagne noire (Sud du Massif central) : nouveaux témoins du magmatisme ordovicien dans la chaîne Varisque. *C R Geosci* 336:19-28.

Rolland Y, Corsini M, Demoux A, 2009. Metamorphic and structural evolution of the Maures-Tanneron Massif (SE Variscan chain): Evidence of doming along a transpressional margin: *Bull Soc Geol Fr* 3:217–230.

Rubatto D, Ferrando S, Compagnoni R, Lombardo B. 2010. Carboniferous high-pressure metamorphism of Ordovician protoliths in the Argentera Massif (Italy), Southern European Variscan belt. *Lithos* 116: 65–76. https://doi.org/10.1016/j.lithos.2009.12.013

Schaltegger U. 1993. The evolution of the polymetamorphic basement in the central Alps unravelled by precise U-Pb zircon dating. *Contrib. Mineral. Petrol.* 113: 466-478.

Schnapperelle S, Mezger JE, Stipp M, Hofmann M, Gärtner A, Linnemann U. 2020 Polyphase magmatic pulses along the Northern Gondwana margin: U-Pb zircon geochronology from gneiss domes of the Pyrenees. *Gondwana Res* 81:291-311.

Schneider J, Corsini M, Reverso-Peila A, Lardeaux JM. 2014. Thermal and mechanical evolution of an orogenic wedge during Variscan collision: an example in the Maures-Tanneron Massif (SE France). *Geol. Soc. Lond. Spec. Publ.* 405:313–331. https://doi.org/10.1144/SP405.4

Sergeev SA, Steiger RH. 1993. High-precision U-Pb single zircon dating of Variscan and Caledonian magmatic cycles in the Gotthard massif, Central Swiss Alps. *Terra Nova* 5:394-395.

Simonetti M, Carosi R, Montomoli C, Langone A, D'Addario E, Mammoliti E. 2018. Kinematic and geochronological constraints on shear deformation in the Ferriere-Mollières shear zone (Argentera-Mercantour Massif, Western Alps): implications for the evolution of the Southern European Variscan Belt. *Int. J. Earth Sci.* 107:2163–2189. https://doi.org/10.1007/s00531-018-1593-y

Simonetti M, Carosi R, Montomoli C, Cottle JM, Law RD. 2020a. Transpressive Deformation in the Southern European Variscan Belt: New Insights From the Aiguilles Rouges Massif (Western Alps). *Tectonics* 39. https://doi.org/10.1029/2020TC006153

Simonetti M, Carosi R, Montomoli C, Corsini M, Petroccia A, Cottle JM, Iaccarino S. 2020b. Timing and kinematics of flow in a transpressive dextral shear zone, Maures Massif (Southern France). *Int J Earth Sci* 109:2261–2285. doi.org/10.1007/s00531-020-01898-6

Simonetti M, Carosi R, Montomoli C, Lawd RD, Cottle JM. 2021. Unravelling the development of regional-scale shear zones by a multidisciplinary approach: The case study of the Ferriere-Mollières Shear Zone (Argentera Massif, Western Alps). *J Struct Geol* 149, 104399

Sláma J, Košler J, Condon DJ, Crowley JL, Gerdes A, Hanchar JM, Horstwood MSA, Morris GA, Nasdala L, Norberg N, Schaltegger U, Schoene B, Tubrett MN, Whitehouse MJ. 2008. Plešovice zircon — A new natural reference material for U–Pb and Hf isotopic microanalysis. *Chem. Geol.* 249:1–35. https://doi.org/10.1016/j.chemgeo.2007.11.005

Stampfli GM, Hochard C, Vérard C, Wilhem C, Von Raumer JF. 2013. The formation of Pangea. *Tectonophysics* 593:1–19.

Stephan T, Kroner U, Romer RL. 2019. The pre-orogenic detrital zircon record of the Peri-Gondwanan crust. *Geol. Mag.* 156:281–307. doi.org/10.1017/S0016756818000031.

Stipp M, Stunitz H, Heilbronner R, Schmid S. 2002. Dynamic recrystallization of quartz: correlation between natural and experimental conditions. In: De Meer, S., Drury, M.R., De Bresser, J.H.P., Pennock, G.M.(eds) Deformation Mechanisms, Rheology and Tectonics: Current Statusand Future Perspectives. *Geol Soc London Spec Publ* 200:171–190.

Strzerzynski P, Guillot S, Courrioux G, Ledru P, 2005. Modélisation géométrique 3D des granites stéphaniens du massif du Pelvoux (Alpes, France). *C R Geosci* 337:1284–1292.

Tait J, Schatz M, Bachtadse V, Soffel H. 2000. Palaeomagnetism and Palaeozoic palaeogeography of Gondwana and European terranes. *Geol. Soc. Lond. Spec. Publ.* 179:21–31.

Tait J.A, Bachtadse V, Franke W, Soffel H.C. 1997. Geodynamic evolution of the European Variscan fold belt: palaeomagnetic and geological constraints. *Geol. Rundsch.* 86:585–598.

Trap P, Roger F, Cenki-Tok B, Paquette JL. 2017. *T*iming and duration of partial melting and magmatism in the Variscan Montagne Noire gneiss dome (French Massif Central). *Int. J. Earth Sci.* 106:453–476.

Vanardois J, 2021. Fusion partielle, transfert de magma et partitionnement de la déformation dans la croûte tardi-orogénique. Exemple des massifs des Aiguilles-Rouges (Alpes) et de l'Agly (Pyrénées) dans la chaîne Varisque. PhD Thesis, Université de Franche-Comté, France. pp 487.

Vanardois J, Roger F, Trap P, Goncalves P, Lanari P, paquette JL, Marquer D, Cagnard F, Le Bayon B, Melleton J, Barou F. 2022. Variscan eclogites from Aiguilles-Rouges Massif (Western Alps): Witnesses of exhumation of deep crust through strike-slip shear zone. *J Metamorph Geol.*

Vanderhaeghe, O., Burg, J. P., & Teyssier, C. 1999. Exhumation of migmatites in two collapsed orogens: Canadian Cordillera and French Variscides. Geological Society, London, Special Publications, 154(1), 181-204.

Vanderhaeghe O., Laurent O., Gardien V., Moyen J.F., Gébelin G., Chelle-Michou C., Couzinié S., Villaros A., Bellanger B.; Flow of partially molten crust controlling construction, growth and collapse of the Variscan orogenic belt: the geologic record of the French Massif Central. Bulletin de la Société Géologique de France 2020;; 191 (1): 25. doi: https://doi.org/10.1051/bsgf/2020013

von Raumer JF, Bussy F, 2004. Mont-Blanc and Aiguilles-Rouges: Geology of their polymetamorphic basement (External massifs, France-Switzerland): *Mémoires de Géologie (Lausanne)* 42:1–203.

Von Raumer J, Albrecht J, Bussy F, Lombardo B, Ménot R.-P, Schaltegger U. 1999. The Palaeozoic metamorphic evolution of the Alpine External Massifs. *Schweiz. Miner. Petrog Mitt.* 79: 5–22.

Von Raumer JF, Stampfi GM, Bussy F. 2003. Gondwana-derived microcontinents, the constituents of the Variscan and Alpine collisional orogens. *Tectonophysics* 365:7–22.

Von Raumer JF, Bussy F, Scaltegger U, Schulz B, Stampfli G.M. 2013. Pre-Mesozoic Alpine basements? Their place in the European Paleozoic framework. *GSA Bull*. 125:89–108.

Von Raumer JF. Stampfli GM. Arenas R. Martínez SS. 2015. Ediacaran to Cambrian oceanic rocks of the Gondwana margin and their tectonic interpretation. Int. J. Earth Sci. 104:1107–1121.

Villaros, A., Laurent, O., Couzinié, S., Moyen, J. F., & Mintrone, M. 2018. Plutons and domes: the consequences of anatectic magma extraction—example from the southeastern French Massif Central. International Journal of Earth Sciences, 107(8), 2819-2842.

White RW, Powell R, Holland TJB, Worley BA. 2000. The effect of TiO2 and Fe2O3 on metapelitic assemblages at greenschist and amphibolite facies conditions: mineral equilibria calculations in the system K2O-FeO-MgO-Al2O3-SiO2-H2O-TiO2-Fe2O3. *J Metamorph Geol* 18:497–511.

White RW, Powell R, Holland TJB, Johnson TE, Green ECR. 2014. New mineral activity–composition rela-tions for thermodynamic calculations in metapelitic systems. *J Metamorph Geol* 32:261–286.

Figure Captions:

Figure 1. A: Location of the External Crystalline Massif (ECMs) within the Variscan framework, modified after Franke et al. (2017). B: State-of-the art concept showing the possible shear zone pattern along the ECMs and Corsica-Sardigna, in relation with the dextral EVSZ (modified from Simonetti et al. 2020). The studied area, i.e. the Belledonne-Pelvoux massif, is not yet considered in this scheme.

Figure 2. A: Simplified Geological map of the ECMs. Dashed square shows the extent of Figure 2B. B: Geological map of the Pelvoux Massif with sample location. Dashed area shows the location of Figure 3.

Figure 3. A: Structural map of the Pelvoux massif showing the heterogeneous Variscan strain pattern. Lower-hemisphere Wulf stereographic plots of poles of foliations and strikes of lineation.

Figure 4. A: NW-SE cross-section through the northern part of the Pelvoux massif. B: E-W cross-section through the western part of the Pelvoux massif. C: W-E cross-section through the central part of the Pelvoux Massif.

Figure 5. Field pictures of D_2 folding and shearing. A and B: F2 folding of migmatitic S_1 and development of N30°E trending S_2 foliation as axial surface or transposition layering. C and D: Folding and shearing along the C_2 and C'_2 trend (NS and NW-SE). The folded and sheared foliation is a S_1, S_2 or C_2 planar surface. In photograph 5C, the gneissic protolith was folded when the anatectic melt was present, and the melt also migrated along D_2 shear zone that parallels the axial plane. In 5D, shearing parallel to the axial plane resulted in solid-state recrystallization. E: Diatexite with a high proportion of leucocratic neosome with metamafic layers showing D_2 folding and sinistral shearing along a N120°E trending C'_2 syn-melt shear zone. F: Schollen diatexite with meter scale metamafic enclaves stretched along N-S direction (C_2) and shearing by a NW-SE trending C'_2 infilled by melt. Location of outcrop photographs is given in Figure 2.

Figure 6: Field pictures of D_2 deformation synchronous with partial melting. A: Sigmoidal quartz-rich resistor within D_2 metatexite indicating sinistral shearing along C_2 directed

migmatitic foliation. B: Oblate metamafic enclave observed in the XY-section within a stromatic diatexite. C: Conjugate melt-bearing dextral and sinistral shear bands within heterogeneous diatexite. Main foliation is subvertical and trends ca. N170°E. D: Schollen diatexite migmatite developed from a hornblende-bearing volcano-sedimentary protolith. E: Close-up on Figure 6D showing the dioritic to tonalitic composition of the leucoratic material containing various proportions of hornblende, some pyroxenes are also observed. The pen points to a garnet + hornblende rich schlieren. F: Metatexite migmatite showing two sets of late cordierite-bearing leucosome, one set parallels the main foliation trends (~N15°E, i.e. C_2) and the other one is oblique to the foliation, and oriented ~N135°E (C'_2).

Figure 7: A: Schematic drawing showing the three main trends of the D_2 planar surface arranged in a sinistral S_2-C_2-C'_2 like anastomosed transpressional system. This representative outcrop comes from the Bans valley, southeastern Inner Pelvoux. Picture 7B shows the steeply dipping S_2 cleavage observed within the Peyre-Arguet mafic granulite, retrogressed into amphibolite. Very thin seams of leucosome are located parallel to the compositional layering, and S_2 or C_2 foliation. Picture 7C shows a strongly layered stromatic migmatite that has been reworked by solid-state deformation during sinistral shearing along a C'_2 plane.

Figure 8. Outcrop photographs and micro-photographs of the D_3 deformation. A: Folding and transposition of the subvertical S_2 foliation by the flat laying S_3 foliation in the northern part of the *Le Rochail* block. B: Folding and transposition of the relictual S_1 foliation by the flat laying S_3 foliation in the northern part of the *Le Rochail* block. C: S_3-C_3 structures showing top-to-the-NW kinematics from sample *MCE382b*. D: Zoom of the photo E with top-to-the-NW kinematic indicators and schematic block diagram of the outcrop.

Figure 9. Field pictures of D_3 deformation. A and B. Low-angle S_3 reworking a steep S_2 foliation. Both foliations are melt-bearing and a pegmatitic leucosome parallels C_3 shear bands. The outcrop is located near the Gioberney mountain refuge. C. Melt-bearing flat-lying D_3 shear zone cross-cutting the steep S_2 foliation. Outcrop photographs A, B C and D are located around the Gioberney mountain refuge, in the La Meige Block. D. Vertical shortening of S_2 and development of axial planar S_3. E. Mylonitic S_3 with top-to-the NW shearing at the base of the Cortical Pelvoux, near Villard-Notre-Dame village. F. Moderately dipping migmatitic gneiss (*MCE 330*) showing a solid-state protomylonitic foliation S_3 developed during D_3 shearing and cooling.

Figure 10. Thin-sections photographs and BSE images showing structural and petrological relationships of samples *MCE379* and *MCE382b*. A: Thin-section photograph of sample *MCE379* structured by D_1 planar fabric. B: BSE image of a monazite included in K-feldspar. C and D: BSE images of monazite grains in mica marking the S_1 foliation. E: Thin-section photograph of sample *MCE382* structured by D_1 planar fabric and D_3 shear bands. F: BSE image of a monazite included in K-feldspar. G and H: BSE images of monazite grains in biotite marking the S_3 foliation. Mineral abbreviations from Kretz (1983).

Figure 11. Thin-sections photographs and BSE images showing structural and petrological relationships of samples *MCE339v*, *MCE338* and *MCE328*. A: Thin-section photograph of sample *MCE339v* structured by D_2 planar fabric. B: BSE image of a monazite oriented parallel with the ancient S_1 foliation preserved in kyanite (white dotted line). C: BSE image of monazite grains in mica marking the S_2 foliation. D: Thin-section photograph of sample *MCE338* structured by D_1 planar fabric showing elongated garnet grains parallel to the S_1 foliation. E: BSE image of a monazite included in quartz showing a sigmoidal shape. F: BSE image of a monazite in micas marking the S_2 foliation. G: Thin-section photograph of sample *MCE328* structured by D_1 planar fabric and D_3 shear bands. H: BSE image of a monazite elongated parallel to the S_1 foliation included in quartz. I: BSE image of a monazite staurolite and quartz.

Figure 12. Monazite U-Pb concordia diagrams obtained by LA-ICPMS. A: *MCE379*; B: *MCE382b*; C: *MCE339v*; D: *MCE338*; E: *MCE328*; F: *MCE314*. Error ellipses and uncertainties in ages are ± 2σ. Dotted ellipses are not considered for the age calculation.

Figure 13. Thermobarometric modelling of metapelitic sample *MCE339v* located in the Cortical Pelvoux. A: Chemical profile of a garnet. B: T-XH_2O diagram calculated with a pressure of 0.7 GPa, the mineral assemblage of the sample indicates a H_2O content of 1.33 %wt. C: Pseudosection calculated in the MnNCKFMASH system. D: Modelling of the Qcmp factor of the mineral composition of biotite based on MgO, FeO, MnO, Al_2O_3 and SiO_2 contents (Table S2). Bi, Biotite; Mu, muscovite; Crd, Cordierite; Kfs, K-feldspar; Pl, Plagioclase; Gt, Garnet; and, Andalousite; ky, Kyanite; sill, Sillimanite; Opx, Orthopyroxene; q, Quartz; melt, silicate liquid.

Figure 14. Thermobarometric modelling of metapelitic sample *MCE338* located in the Cortical Pelvoux. A: Chemical profile of a garnet. B: T-XH_2O diagram calculated with a pressure of 0.5 GPa, the mineral assemblage of the sample indicates a H_2O content of 1.47 %wt. C: Pseudosection calculated in the MnNCKFMASH system. Modelling of the Qcmp factor of the mineral composition of (D) biotite based on MgO, FeO, MnO, Al_2O_3 and SiO_2 contents, (E) muscovite based on Na_2O, K_2O, CaO, Al_2O_3, FeO, MgO and SiO_2 contents, and (F) plagioclase based on K_2O, Na_2O, CaO, Al_2O_3 and SiO_2 contents (Table S2). Bi, Biotite; Mu, muscovite; Crd, Cordierite; Kfs, K-feldspar; Pl, Plagioclase; Gt, Garnet; and, Andalousite; ky, Kyanite; sill, Sillimanite; Opx, Orthopyroxene; q, Quartz; melt, silicate liquid.

Figure 15. Zircon U-Pb Tera Wasserburg diagrams obtained by LA-ICPMS. A: *MCE330*; B: *MCE140b*; C: *MCE313b*; D: *MCE304v2*. Error ellipses and uncertainties in ages are ± 2σ. Dotted ellipses are not considered for the age calculation.

Figure 16. Geochronological and tectono-metamorphic interpretations for the Pelvoux massif. (a) P-T-t path of sample *MCE338* inferred from the mineral assemblage and mineral compositions and from textural features of monazite. (b) P-T-t path of sample *MCE339v* inferred from the mineral assemblage and biotite composition and from textural features of monazite. (c) P-T-t conditions from the Pelvoux massif. P-T-t paths of the Cortical Pelvoux are from this study. P-T data from metabasites of the Inner Pelvoux are from Jacob et al. (2022) and Grandjean et al. (1996). P-T conditions of Crd-migmatites are theoretical and age corresponds to monazite age of sample *MCE314* from this study. (d) Geochronological results constraining the ages of D_1, D_2 and D_3 from this study, (Fréville et al., 2018; Fréville, 2016). (e) Inferred tectono-metamorphic evolutions of the Cortical and Inner Pelvoux.

Figure 17. Sketch showing the strain partitioning in the Belledonne-Pelvoux orogenic crust suffering bulk NW-SE directed contraction (black arrows). The upper unmolten crustal level recorded folding, while the partially molten lower domain recorded lateral flow and sinistral transpression.

Figure 18. Sketch map of the anastomosed network of dextral shear zones of the EVSZ with local conjugate sinistral shear zones in the Pelvoux massif. Ante-alpine positions of the ECMs (black arrow) are from Bellahsen et al. (2014), except the Argentera massif. Positions of the Maures-Tanneron, Corsica and Sardinia massifs are from Edel et al. (2014, 2018). Blue arrow represents the present orientation in reference to the north. AG: Aar-Gothard; Arg: Argentera;

AR-MB: Aiguilles-Rouges - Mont-Blanc; Bell: Belledonne; BSZ: Barrabisa Shear Zone; EBSZ: Emosson-Bérarde Shear Zone; FMSZ: Ferrière-Mollière Shear Zone; GF: Grimaud Fault; MF: La Moure Fault; PAL: Posada-Asinara Shear Zone; Pelv: Pelvoux; PVSZ: Porto Vecchio Shear Zone.

Table 1. Summary of geographic location, rock types, and U-Pb geochronological results for samples analyzed in this study.

Table 2. Bulk-chemical composition in weight percent oxides for samples *MCE339v* and *MCE338*.

Table 3. Representative chemical compositions of minerals used for themobarometric calculation.

Table 4. Summary of tectonic and metamorphic events recorded in the Belledonne-Pelvoux area.

Supplementary material:

Figure S1. Zircon cathodoluminescence and monazite back-scattered electrons images from studied samples.

Table S1. U-Pb analyses for dated samples.

Table S2. Operating conditions for the LA-ICP-MS equipment for Montpellier.

Table S3. Operating conditions for the LA-ICP-MS equipment for BRGM.

Table S4. Operating conditions for the LA-ICP-MS equipment for Rennes.

Figure 1

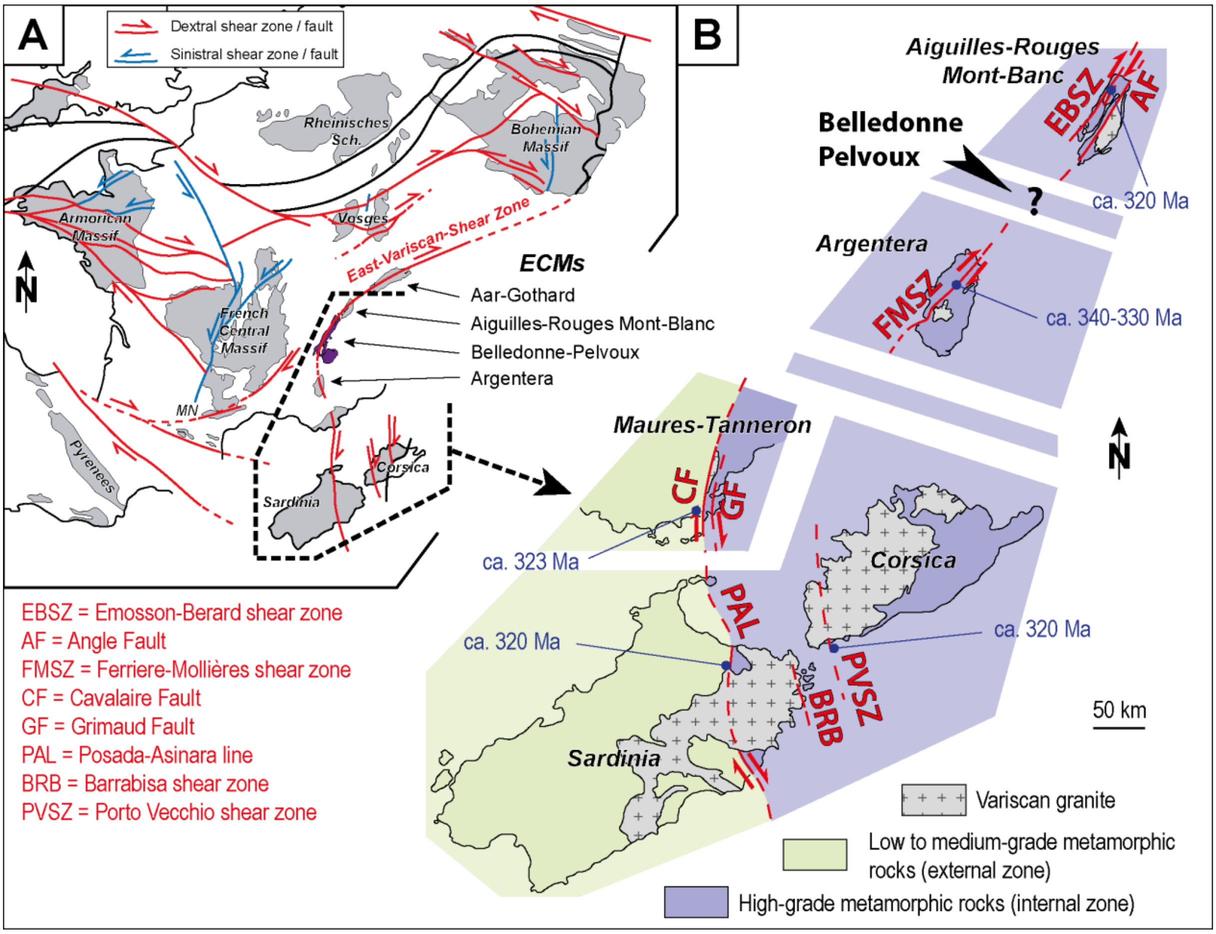
A
Dextral shear zone / fault
Sinistral shear zone / fault
Rheinisches Sch.
Bohemian Massif
Armorican Massif
Vosges
East-Variscan-Shear Zone
French Central Massif
MN
Pyrenees
Sardinia
Corsica
N
ECMs
Aar-Gothard
Aiguilles-Rouges Mont-Blanc
Belledonne-Pelvoux
Argentera
EBSZ = Emosson-Berard shear zone
AF = Angle Fault
FMSZ = Ferriere-Mollières shear zone
CF = Cavalaire Fault
GF = Grimaud Fault
PAL = Posada-Asinara line
BRB = Barrabisa shear zone
PVSZ = Porto Vecchio shear zone
B
Aiguilles-Rouges Mont-Banc
EBSZ
AF
Belledonne Pelvoux
?
ca. 320 Ma
Argentera
FMSZ
ca. 340-330 Ma
Maures-Tanneron
CF
GF
ca. 323 Ma
N
Corsica
PAL
ca. 320 Ma
ca. 320 Ma
PVSZ
BRB
Sardinia
50 km
Variscan granite
Low to medium-grade metamorphic rocks (external zone)
High-grade metamorphic rocks (internal zone)

Figure 2

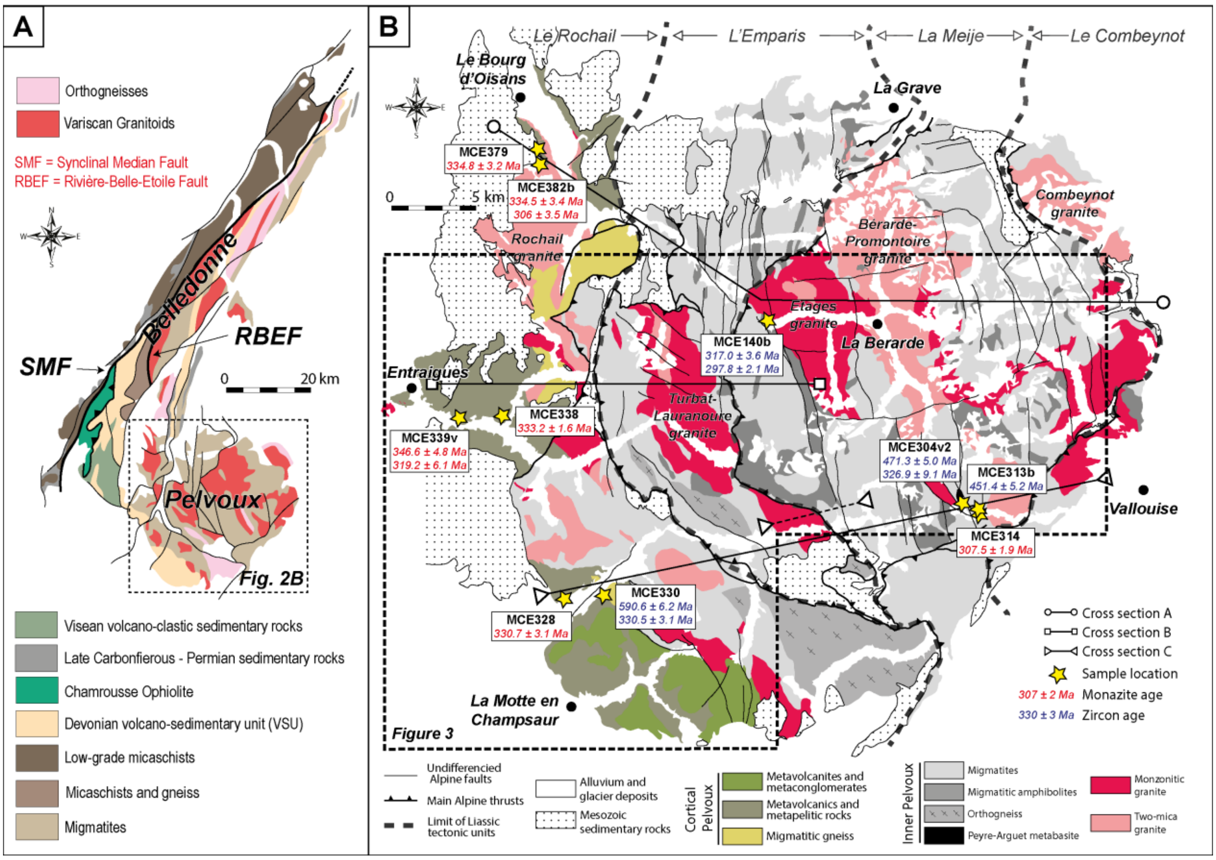
A
Orthogneisses
Variscan Granitoids
SMF = Synclinal Median Fault
RBEF = Rivière-Belle-Etoile Fault
Belledonne
RBEF
SMF
0
20 km
Pelvoux
Fig. 2B
Visean volcano-clastic sedimentary rocks
Late Carbonfierous - Permian sedimentary rocks
Chamrousse Ophiolite
Devonian volcano-sedimentary unit (VSU)
Low-grade micaschists
Micaschists and gneiss
Migmatites
B
Le Rochail
L'Emparis
La Meije
Le Combeynot
Le Bourg d'Oisans
La Grave
MCE379
334.8 ± 3.2 Ma
MCE382b
334.5 ± 3.4 Ma
306 ± 3.5 Ma
0
5 km
Rochail granite
Combeynot granite
Berarde-Promontoire granite
Etages granite
La Berarde
MCE140b
317.0 ± 3.6 Ma
297.8 ± 2.1 Ma
Entraigues
Turbat-Lauranoure granite
MCE338
333.2 ± 1.6 Ma
MCE339v
346.6 ± 4.8 Ma
319.2 ± 6.1 Ma
MCE304v2
471.3 ± 5.0 Ma
326.9 ± 9.1 Ma
MCE313b
451.4 ± 5.2 Ma
Vallouise
MCE314
307.5 ± 1.9 Ma
MCE330
590.6 ± 6.2 Ma
330.5 ± 3.1 Ma
MCE328
330.7 ± 3.1 Ma
La Motte en Champsaur
Figure 3
Cross section A
Cross section B
Cross section C
Sample location
307 ± 2 Ma Monazite age
330 ± 3 Ma Zircon age
Undifferencied Alpine faults
Main Alpine thrusts
Limit of Liassic tectonic units
Alluvium and glacier deposits
Mesozoic sedimentary rocks
Cortical Pelvoux
Metavolcanites and metaconglomerates
Metavolcanics and metapelitic rocks
Migmatitic gneiss
Inner Pelvoux
Migmatites
Migmatitic amphibolites
Orthogneiss
Peyre-Arguet metabasite
Monzonitic granite
Two-mica granite

Figure 3

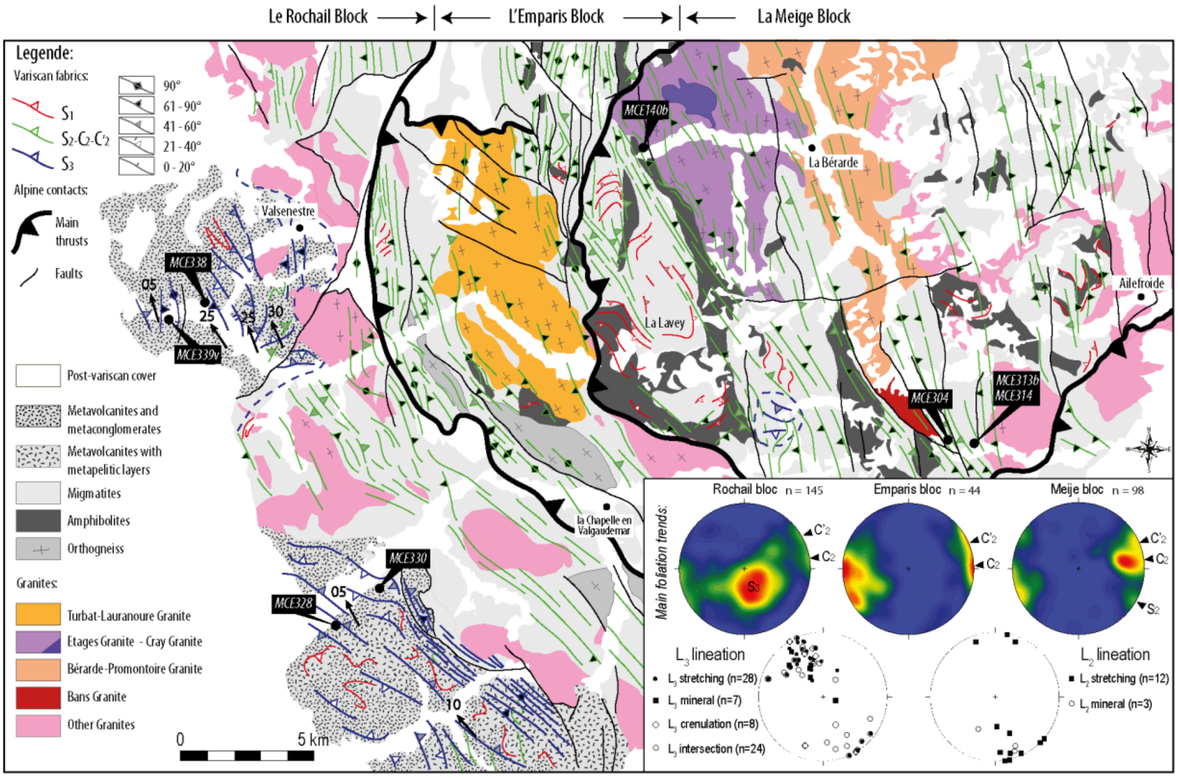
Le Rochail Block
L'Emparis Block
La Meige Block
Legende:
Variscan fabrics:
S1
S2-C2-C'2
S3
90°
61 - 90°
41 - 60°
21 - 40°
0 - 20°
Alpine contacts:
Main thrusts
Faults
Post-variscan cover
Metavolcanites and metaconglomerates
Metavolcanites with metapelitic layers
Migmatites
Amphibolites
Orthogneiss
Granites:
Turbat-Lauranoure Granite
Etages Granite - Cray Granite
Bérarde-Promontoire Granite
Bans Granite
Other Granites
0
5 km
Valsenestre
MCE338
MCE339v
05
25
25
30
MCE330
MCE328
05
10
MCE140b
La Bérarde
La Lavey
Ailefroide
MCE304
MCE313b
MCE314
la Chapelle en Valgaudemar
N
W
E
S
Main foliation trends:
Rochail bloc n = 145
Emparis bloc n = 44
Meije bloc n = 98
S3
C'2
C2
C'2
C2
C'2
C2
S2
L3 lineation
L3 stretching (n=28)
L3 mineral (n=7)
L3 crenulation (n=8)
L3 intersection (n=24)
L2 lineation
L2 stretching (n=12)
L2 mineral (n=3)

Figure 4

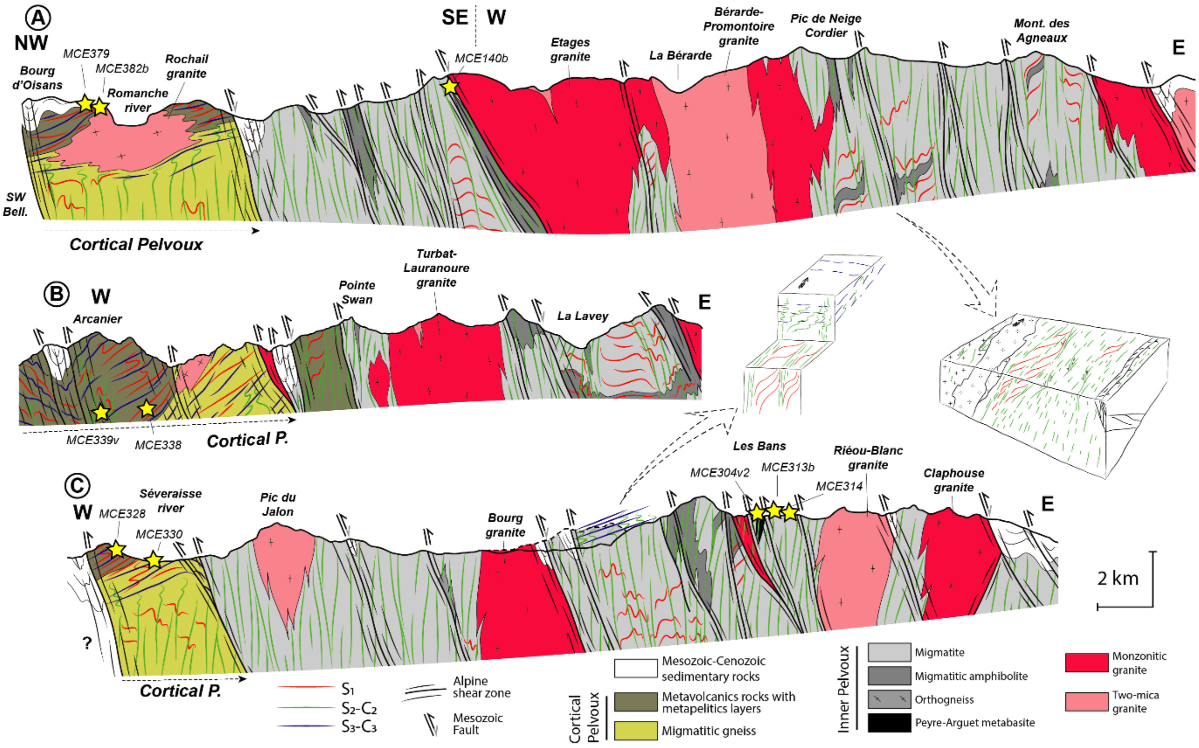
A
NW
Bourg d'Oisans
MCE379
MCE382b
Rochail granite
Romanche river
SW Bell.
Cortical Pelvoux
SE
W
MCE140b
Etages granite
La Bérarde
Bérarde-Promontoire granite
Pic de Neige Cordier
Mont. des Agneaux
E
B
W
Arcanier
Pointe Swan
Turbat-Lauranoure granite
La Lavey
E
MCE339v
MCE338
Cortical P.
C
W
MCE328
Séveraisse river
MCE330
Pic du Jalon
Bourg granite
Les Bans
MCE304v2
MCE313b
Riéou-Blanc granite
MCE314
Claphouse granite
E
?
Cortical P.
2 km
S_1
S_2-C_2
S_3-C_3
Alpine shear zone
Mesozoic Fault
Cortical Pelvoux
Mesozoic-Cenozoic sedimentary rocks
Metavolcanics rocks with metapelitics layers
Migmatitic gneiss
Inner Pelvoux
Migmatite
Migmatitic amphibolite
Orthogneiss
Peyre-Arguet metabasite
Monzonitic granite
Two-mica granite

Figure 5

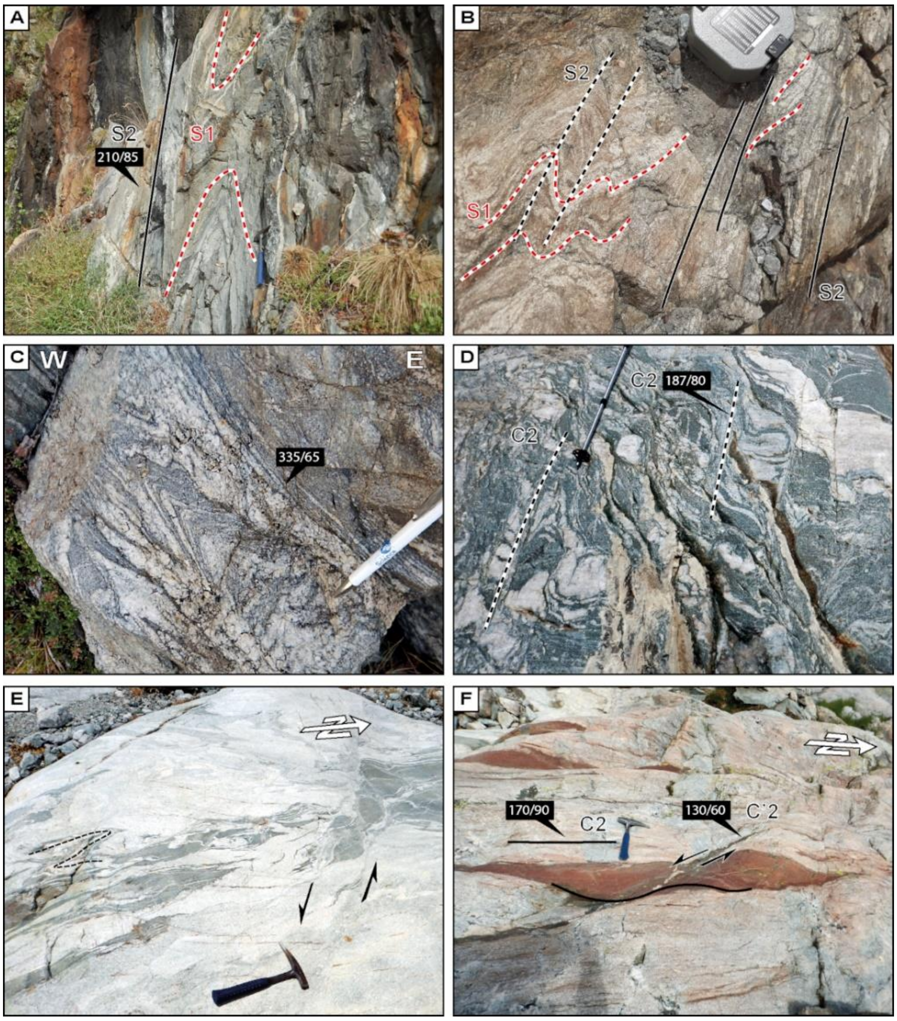
A
S2
210/85
S1
B
S2
S1
S2
C
W
E
335/65
D
C2
187/80
C2
E
F
170/90
C2
130/60
C'2

Figure 6

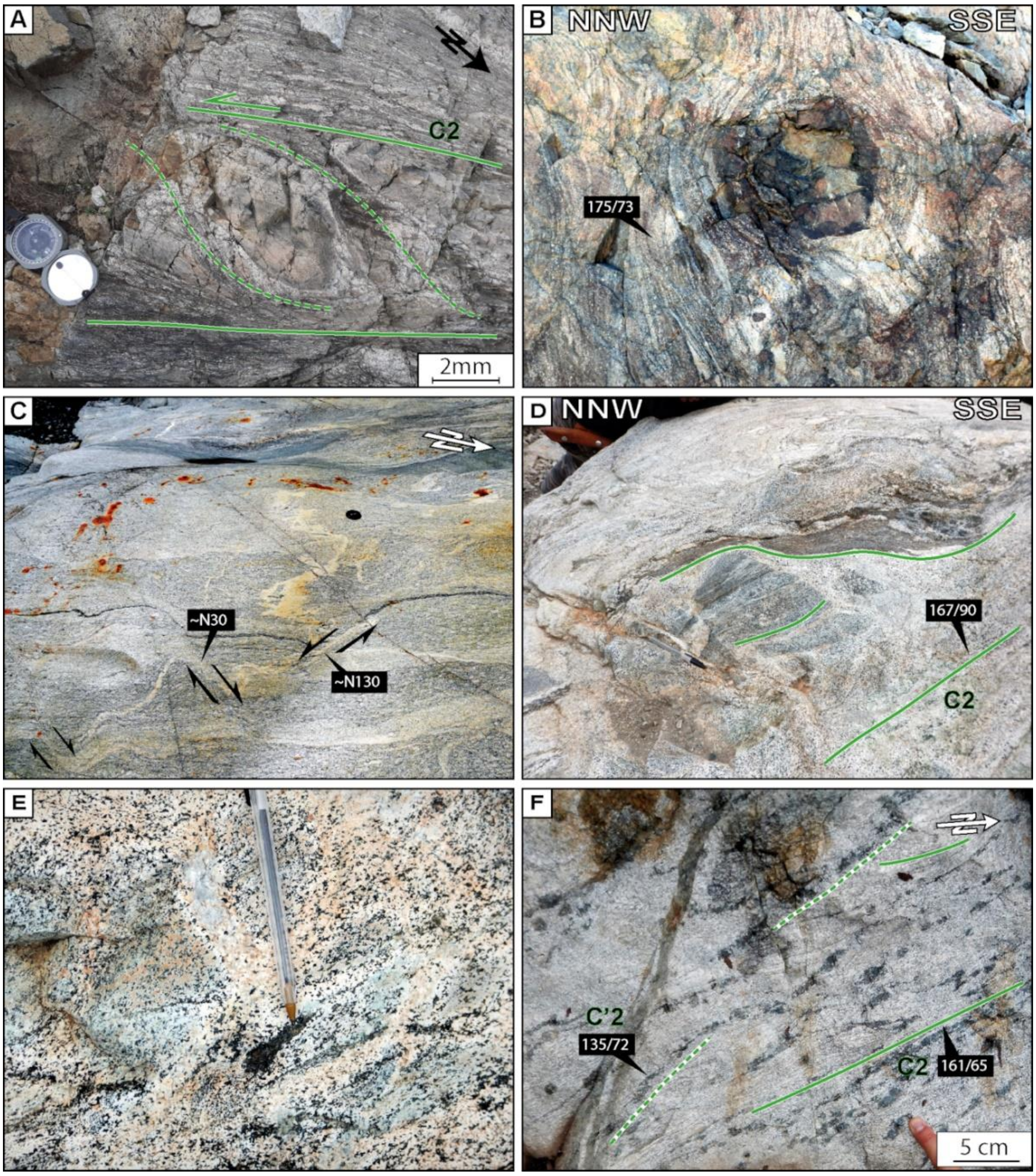
A
C2
2mm
B
NNW
SSE
175/73
C
~N30
~N130
D
NNW
SSE
167/90
C2
E
F
C'2
135/72
C2
161/65
5 cm

Figure 7

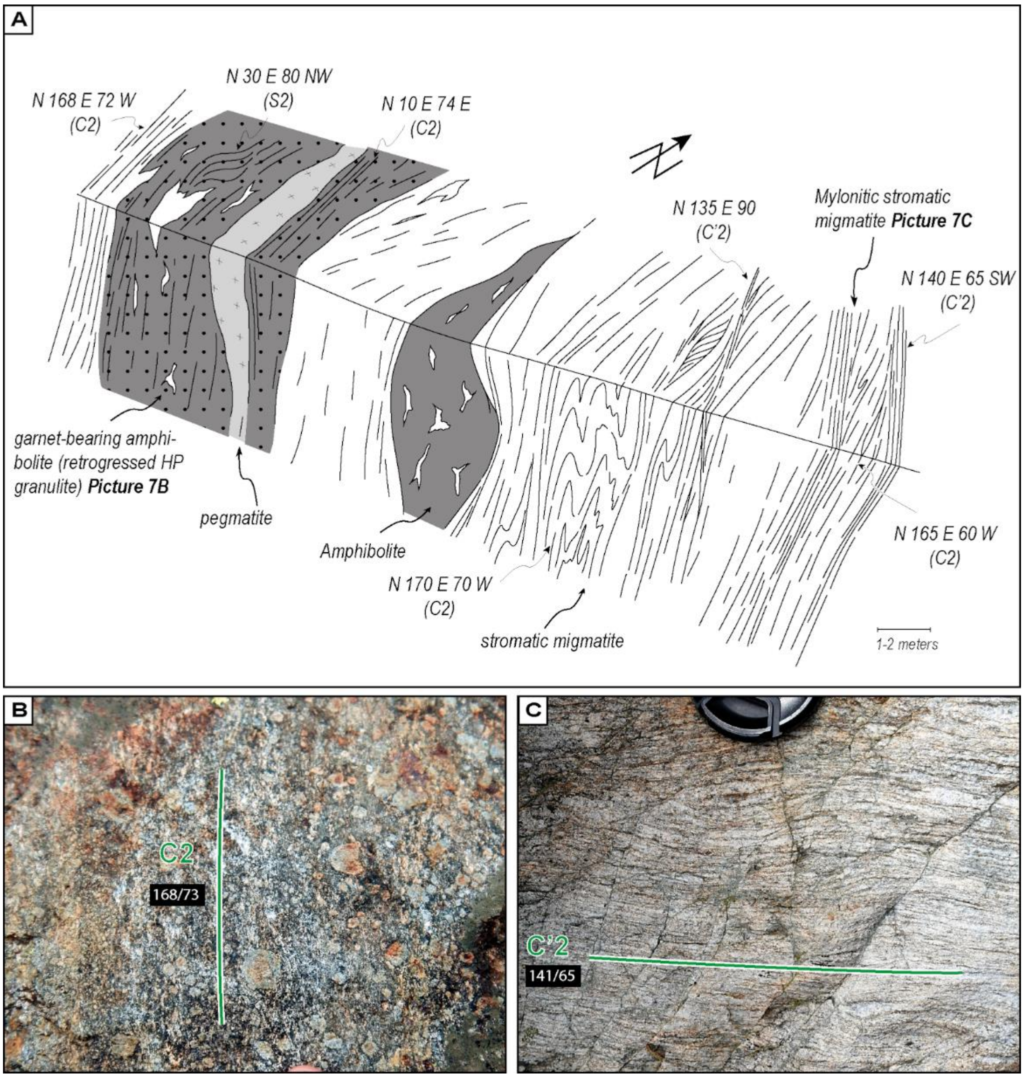
A
N 168 E 72 W
(C2)
N 30 E 80 NW
(S2)
N 10 E 74 E
(C2)
N 135 E 90
(C'2)
Mylonitic stromatic
migmatite **Picture 7C**
N 140 E 65 SW
(C'2)
garnet-bearing amphi-
bolite (retrogressed HP
granulite) **Picture 7B**
pegmatite
Amphibolite
N 170 E 70 W
(C2)
stromatic migmatite
N 165 E 60 W
(C2)
1-2 meters
B
C2
168/73
C
C'2
141/65

Figure 8

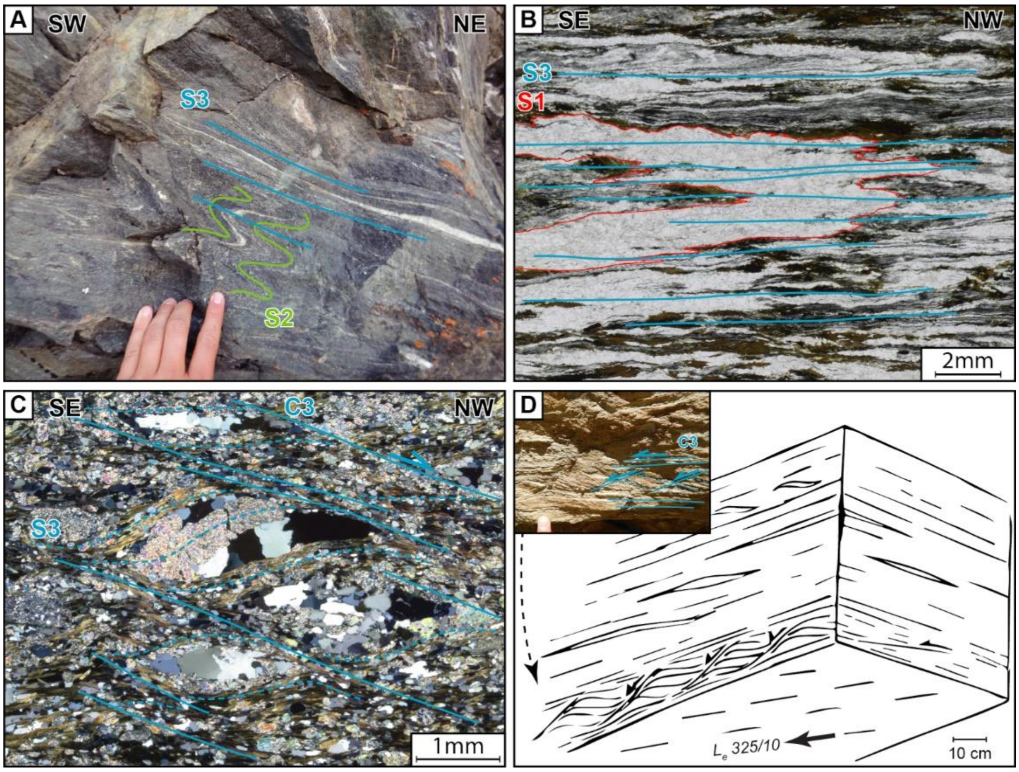

Figure 9

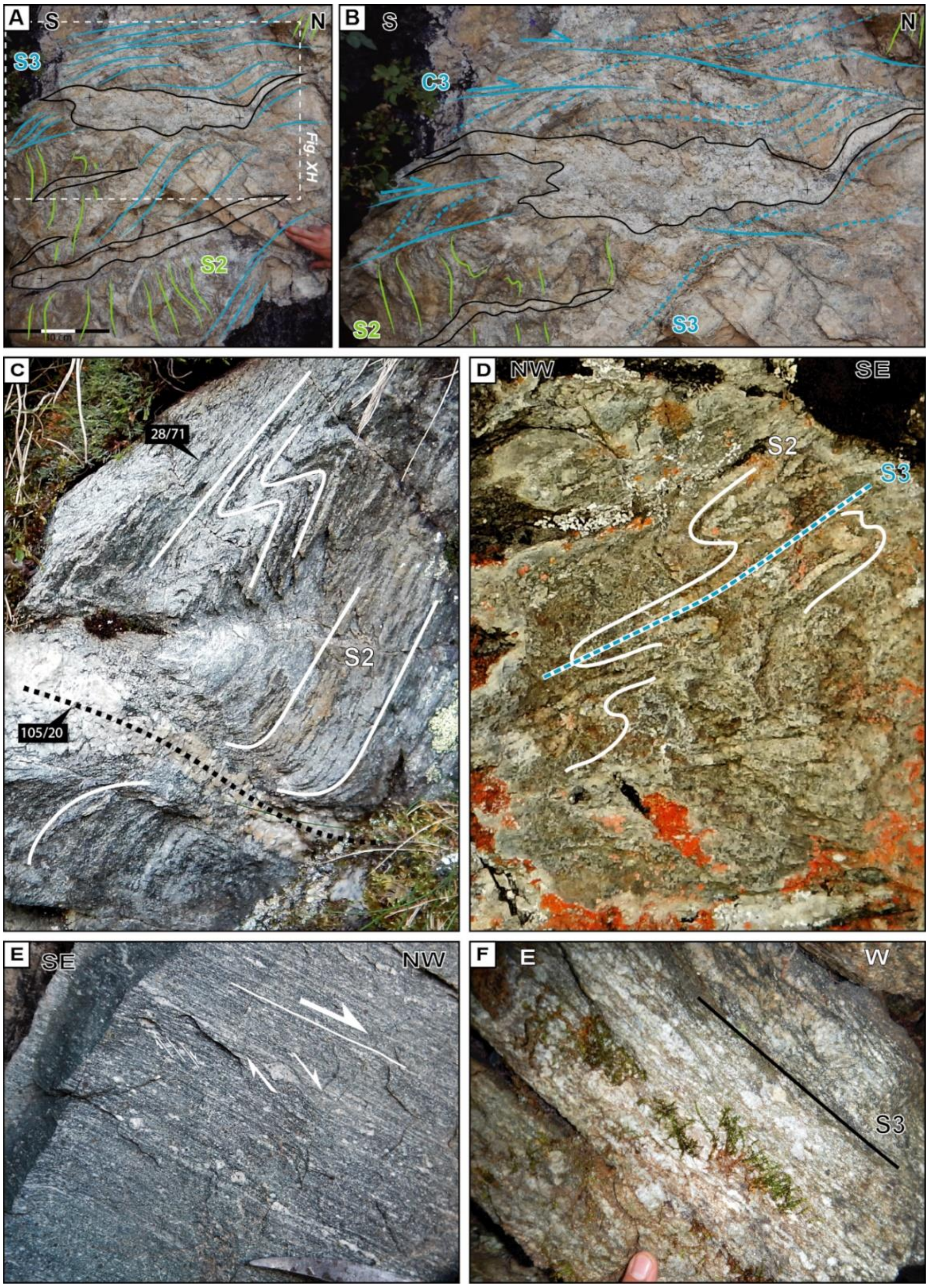
A
S
N
S3
Fig. XH
S2
B
S
N
C3
S2
S3
C
28/71
S2
105/20
D
NW
SE
S2
S3
E
SE
NW
F
E
W
S3

Figure 10

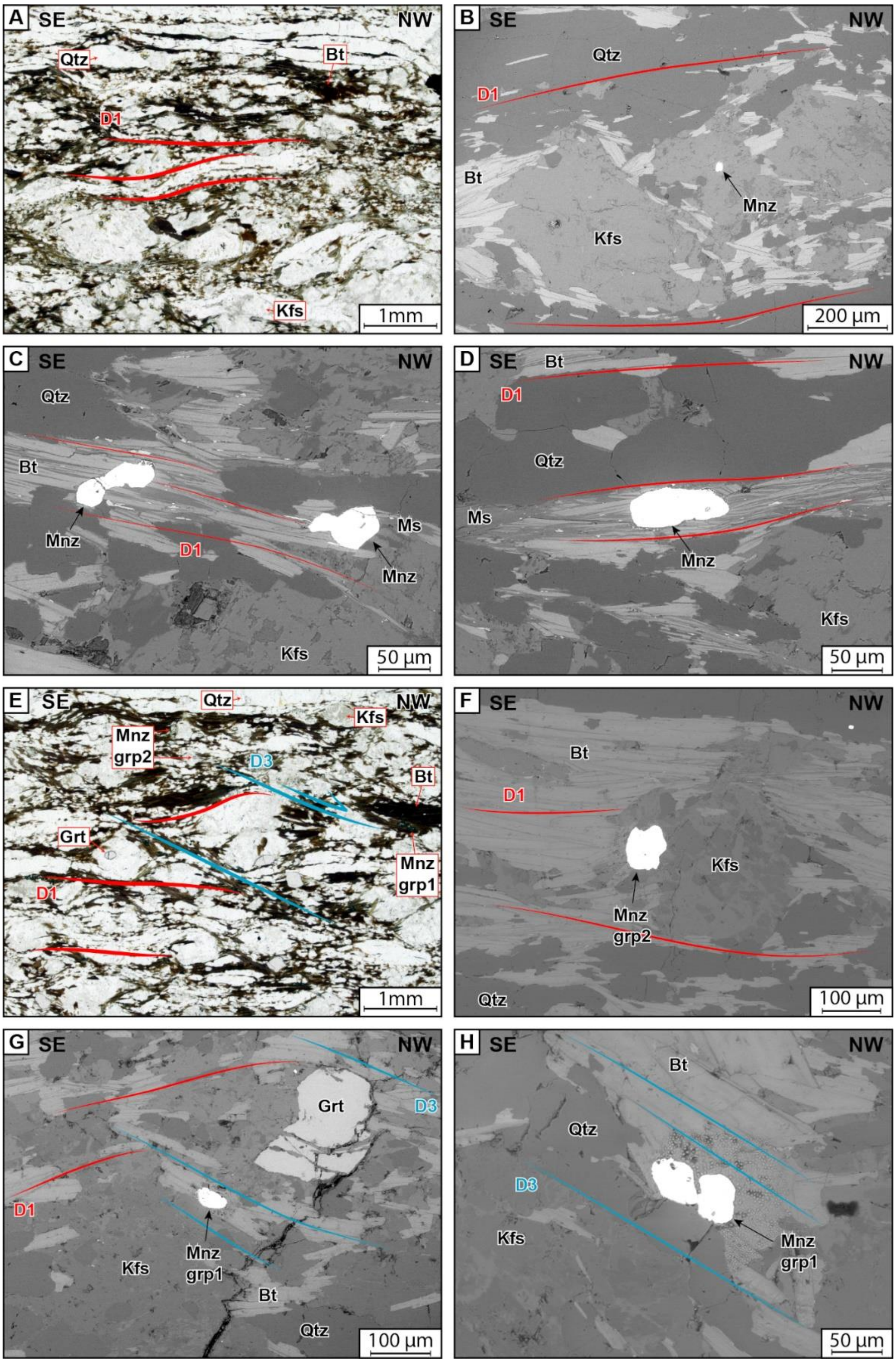
A
SE
NW
Qtz
Bt
D1
Kfs
1mm
B
SE
NW
Qtz
D1
Bt
Mnz
Kfs
200 µm
C
SE
NW
Qtz
Bt
Mnz
D1
Ms
Mnz
Kfs
50 µm
D
SE
Bt
NW
D1
Qtz
Ms
Mnz
Kfs
50 µm
E
SE
Qtz
NW
Kfs
Mnz grp2
D3
Bt
Grt
Mnz grp1
D1
1mm
F
SE
NW
Bt
D1
Kfs
Mnz grp2
Qtz
100 µm
G
SE
NW
Grt
D3
D1
Mnz grp1
Kfs
Bt
Qtz
100 µm
H
SE
NW
Bt
Qtz
D3
Kfs
Mnz grp1
50 µm

Figure 11

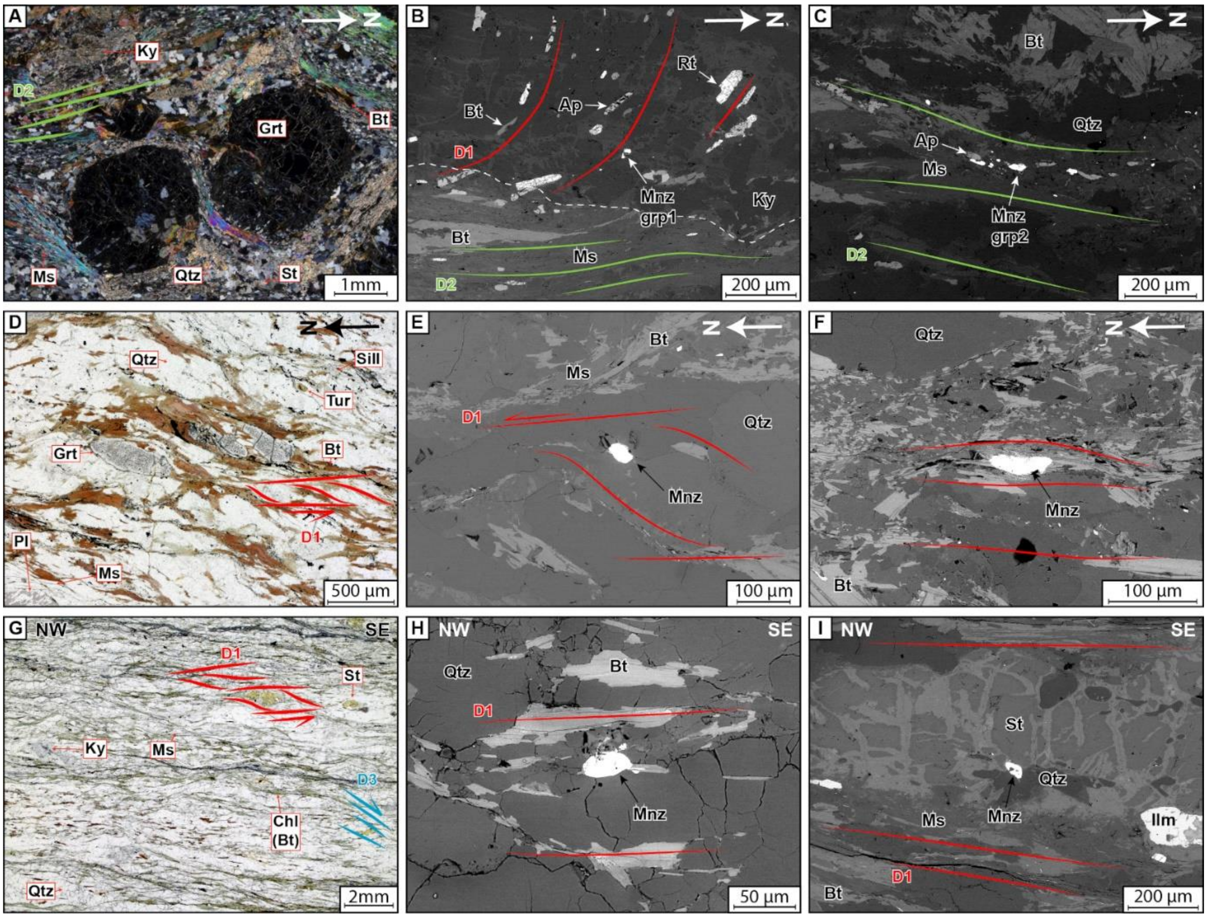
A
N
Ky
D2
Grt
Bt
Ms
Qtz
St
1mm
B
N
Rt
Bt
Ap
D1
Mnz grp1
Ky
Bt
Ms
D2
200 µm
C
N
Bt
Qtz
Ap
Ms
Mnz grp2
D2
200 µm
D
N
Qtz
Sill
Tur
Grt
Bt
D1
Pl
Ms
500 µm
E
N
Bt
Ms
D1
Qtz
Mnz
100 µm
F
N
Qtz
Mnz
Bt
100 µm
G
NW
SE
D1
St
Ky
Ms
D3
Chl (Bt)
Qtz
2mm
H
NW
SE
Qtz
Bt
D1
Mnz
50 µm
I
NW
SE
St
Qtz
Mnz
Ms
Ilm
D1
Bt
200 µm

Figure 12

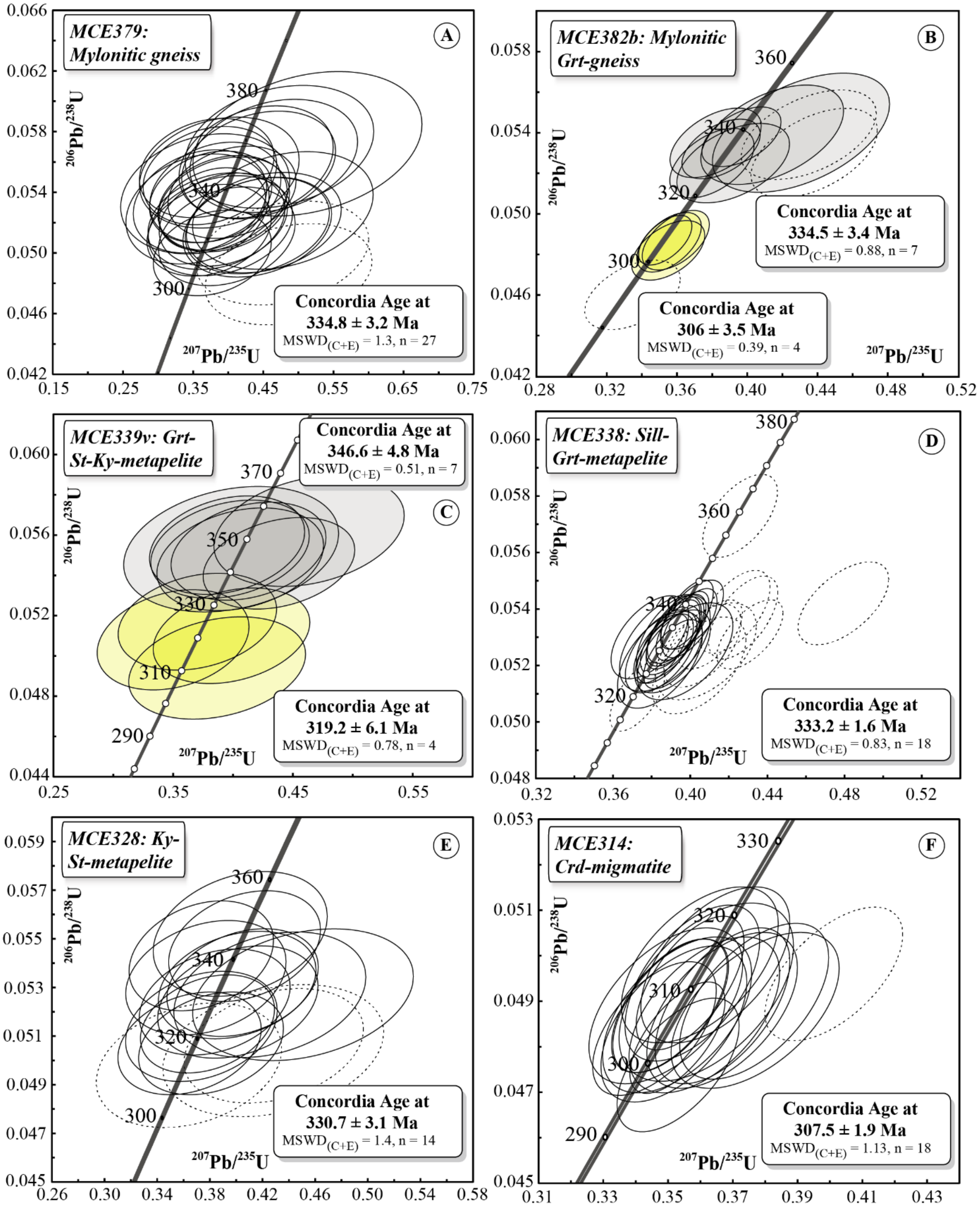
A
MCE379: Mylonitic gneiss
Concordia Age at 334.8 ± 3.2 Ma
MSWD(C+E) = 1.3, n = 27
380
340
300
B
MCE382b: Mylonitic Grt-gneiss
Concordia Age at 334.5 ± 3.4 Ma
MSWD(C+E) = 0.88, n = 7
Concordia Age at 306 ± 3.5 Ma
MSWD(C+E) = 0.39, n = 4
360
340
320
300
C
MCE339v: Grt-St-Ky-metapelite
Concordia Age at 346.6 ± 4.8 Ma
MSWD(C+E) = 0.51, n = 7
Concordia Age at 319.2 ± 6.1 Ma
MSWD(C+E) = 0.78, n = 4
370
350
330
310
290
D
MCE338: Sill-Grt-metapelite
Concordia Age at 333.2 ± 1.6 Ma
MSWD(C+E) = 0.83, n = 18
380
360
340
320
E
MCE328: Ky-St-metapelite
Concordia Age at 330.7 ± 3.1 Ma
MSWD(C+E) = 1.4, n = 14
360
340
320
300
F
MCE314: Crd-migmatite
Concordia Age at 307.5 ± 1.9 Ma
MSWD(C+E) = 1.13, n = 18
330
320
310
300
290
206Pb/238U
207Pb/235U

Figure 13

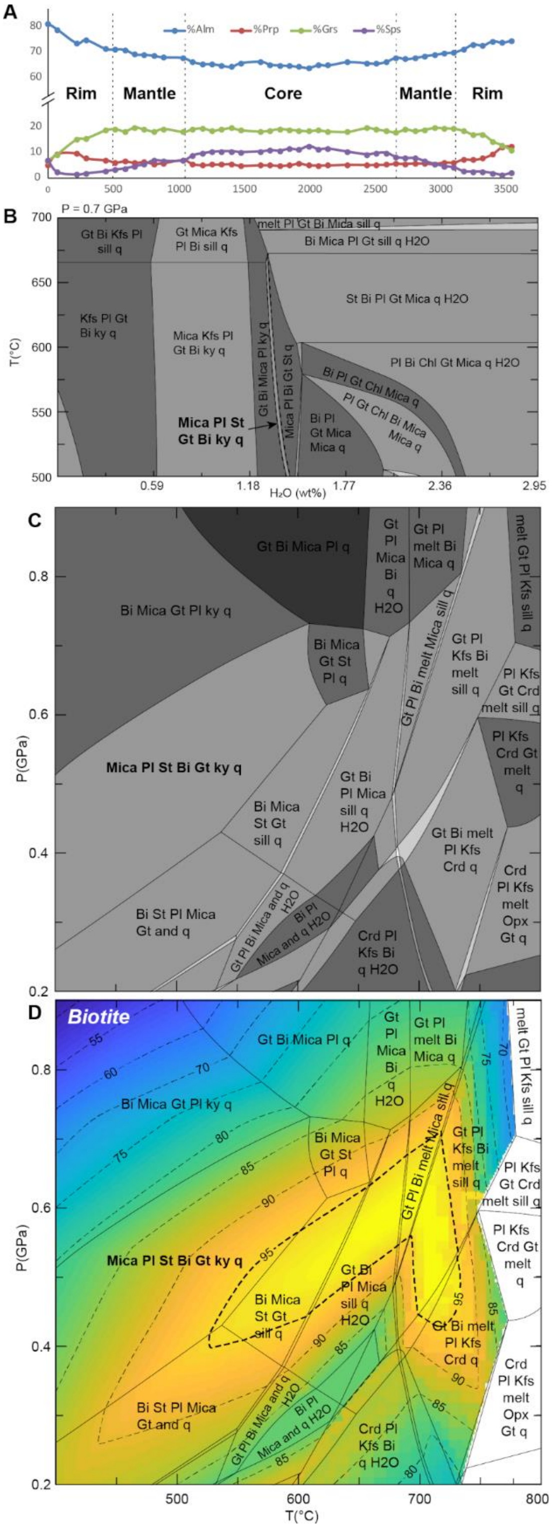
A
%Alm
%Prp
%Grs
%Sps
Rim
Mantle
Core
Mantle
Rim
B
P = 0.7 GPa
Gt Bi Kfs Pl sill q
Gt Mica Kfs Pl Bi sill q
melt Pl Gt Bi Mica sill q
Bi Mica Pl Gt sill q H2O
St Bi Pl Gt Mica q H2O
Kfs Pl Gt Bi ky q
Mica Kfs Pl Gt Bi ky q
Gt Bi Mica Pl ky q
Mica Pl Bi Gt St q
Pl Bi Chl Gt Mica q H2O
Bi Pl Gt Chl Mica q
Pl Gt Chl Bi Mica Mica q
Bi Pl Gt Mica Mica q
Mica Pl St Gt Bi ky q
T(°C)
H₂O (wt%)
C
Gt Bi Mica Pl q
Gt Pl Mica Bi q H2O
Gt Pl melt Bi Mica q
melt Gt Pl Kfs sill q
Bi Mica Gt Pl ky q
Bi Mica Gt St Pl q
Gt Pl Bi melt Mica sill q
Gt Pl Kfs Bi melt sill q
Pl Kfs Gt Crd melt sill q
Pl Kfs Crd Gt melt q
Mica Pl St Bi Gt ky q
Gt Bi Pl Mica sill q H2O
Bi Mica St Gt sill q
Gt Bi melt Pl Kfs Crd q
Crd Pl Kfs melt Opx Gt q
Bi St Pl Mica Gt and q
Gt Pl Bi Mica and q H2O
Bi Pl Mica and q H2O
Crd Pl Kfs Bi q H2O
P(GPa)
D
Biotite
55
60
70
75
80
85
90
95
T(°C)

Figure 14

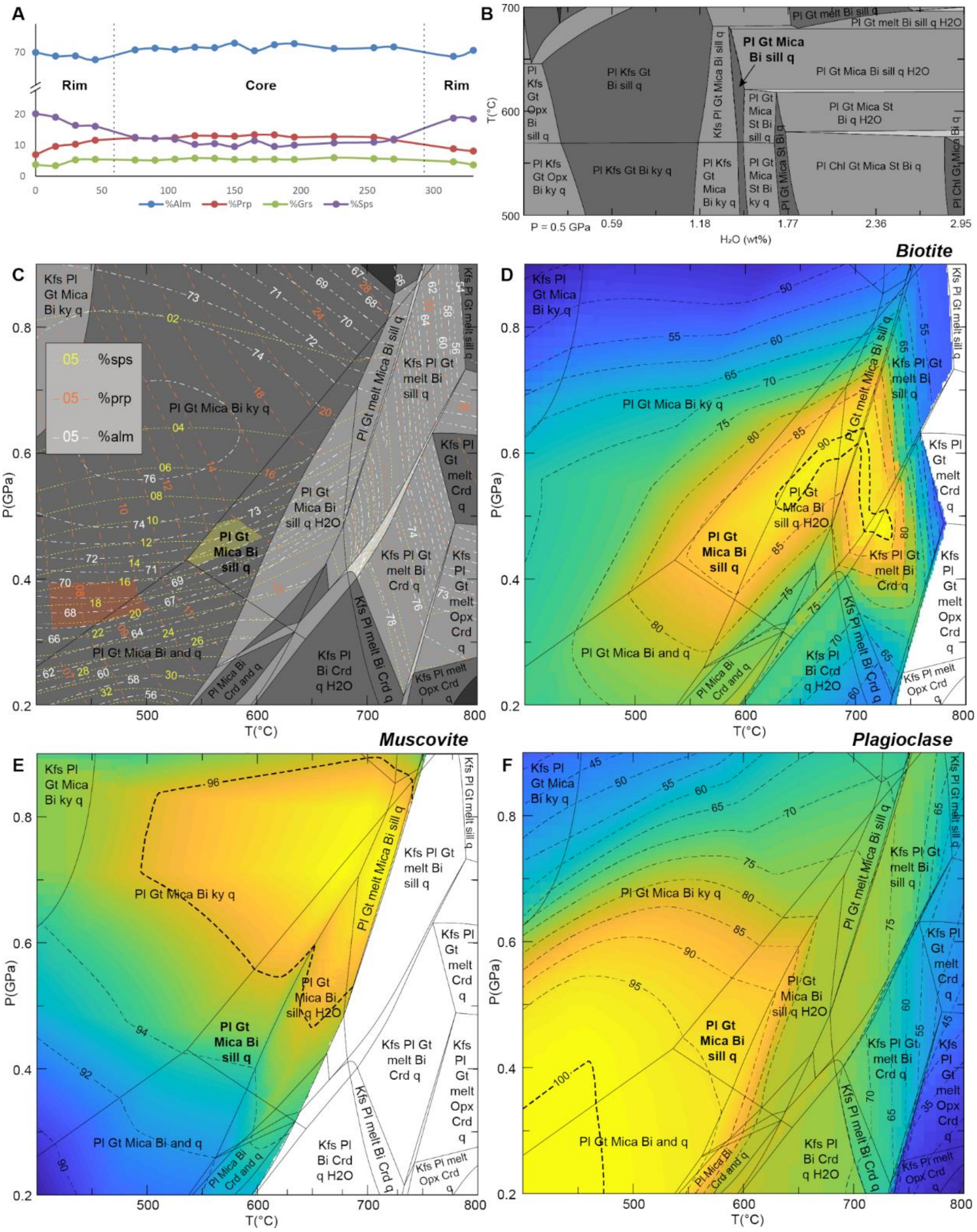
A
70
Rim
Core
Rim
20
10
0
0
50
100
150
200
250
300
%Alm
%Prp
%Grs
%Sps
B
700
600
T(°C)
500
P = 0.5 GPa
0.59
1.18
1.77
2.36
2.95
H₂O (wt%)
Pl Gt melt Bi sill q
Pl Gt melt Bi sill q H2O
Pl Gt Mica Bi sill q
Pl Kfs Gt Bi sill q
Pl Gt Mica Bi sill q H2O
Pl Kfs Gt Opx Bi sill q
Kfs Pl Gt Mica Bi sill q
Pl Gt Mica St Bi sill q
Pl Gt Mica St Bi q H2O
Pl Kfs Gt Opx Bi ky q
Pl Kfs Gt Bi ky q
Pl Kfs Gt Mica Bi ky q
Pl Gt Mica St Bi ky q
Pl Gt Mica St Bi q
Pl Chl Gt Mica St Bi q
Pl Chl Gt Mica Bi q
C
Kfs Pl Gt Mica Bi ky q
%sps
%prp
%alm
Pl Gt Mica Bi ky q
Pl Gt melt Mica Bi sill q
Kfs Pl Gt melt Bi sill q
Kfs Pl Gt melt sill q
Kfs Pl Gt melt Crd q
Pl Gt Mica Bi sill q H2O
Pl Gt Mica Bi sill q
Kfs Pl Gt melt Bi Crd q
Kfs Pl Gt melt Opx Crd q
Pl Gt Mica Bi and q
Pl Mica Bi Crd and q
Kfs Pl Bi Crd q H2O
Kfs Pl melt Bi Crd q
Kfs Pl melt Opx Crd q
P(GPa)
T(°C)
Biotite
D
Muscovite
E
Plagioclase
F
0.8
0.6
0.4
0.2
500
600
700
800

Figure 15

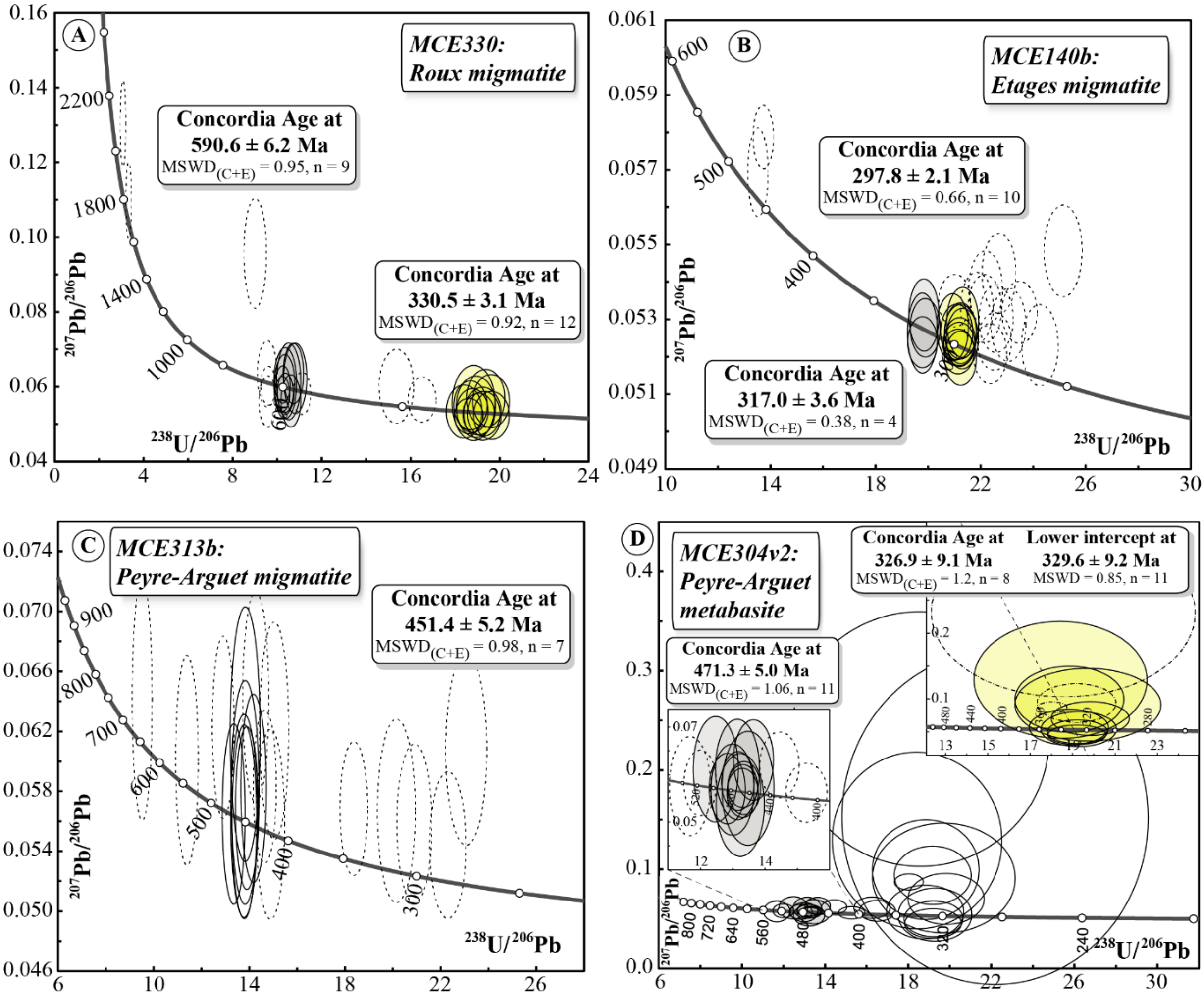
A
MCE330:
Roux migmatite
Concordia Age at
590.6 ± 6.2 Ma
MSWD(C+E) = 0.95, n = 9
Concordia Age at
330.5 ± 3.1 Ma
MSWD(C+E) = 0.92, n = 12
207Pb/206Pb
238U/206Pb
2200
1800
1400
1000
0.16
0.14
0.12
0.10
0.08
0.06
0.04
0
4
8
12
16
20
24
B
MCE140b:
Etages migmatite
Concordia Age at
297.8 ± 2.1 Ma
MSWD(C+E) = 0.66, n = 10
Concordia Age at
317.0 ± 3.6 Ma
MSWD(C+E) = 0.38, n = 4
600
500
400
0.061
0.059
0.057
0.055
0.053
0.051
0.049
10
14
18
22
26
30
C
MCE313b:
Peyre-Arguet migmatite
Concordia Age at
451.4 ± 5.2 Ma
MSWD(C+E) = 0.98, n = 7
900
800
700
600
500
400
300
0.074
0.070
0.066
0.062
0.058
0.054
0.050
0.046
6
10
14
18
22
26
D
MCE304v2:
Peyre-Arguet
metabasite
Concordia Age at
326.9 ± 9.1 Ma
MSWD(C+E) = 1.2, n = 8
Lower intercept at
329.6 ± 9.2 Ma
MSWD = 0.85, n = 11
Concordia Age at
471.3 ± 5.0 Ma
MSWD(C+E) = 1.06, n = 11
0.4
0.3
0.2
0.1
0.0
800
720
640
560
480
400
320
240
6
10
14
18
22
26
30

Figure 16

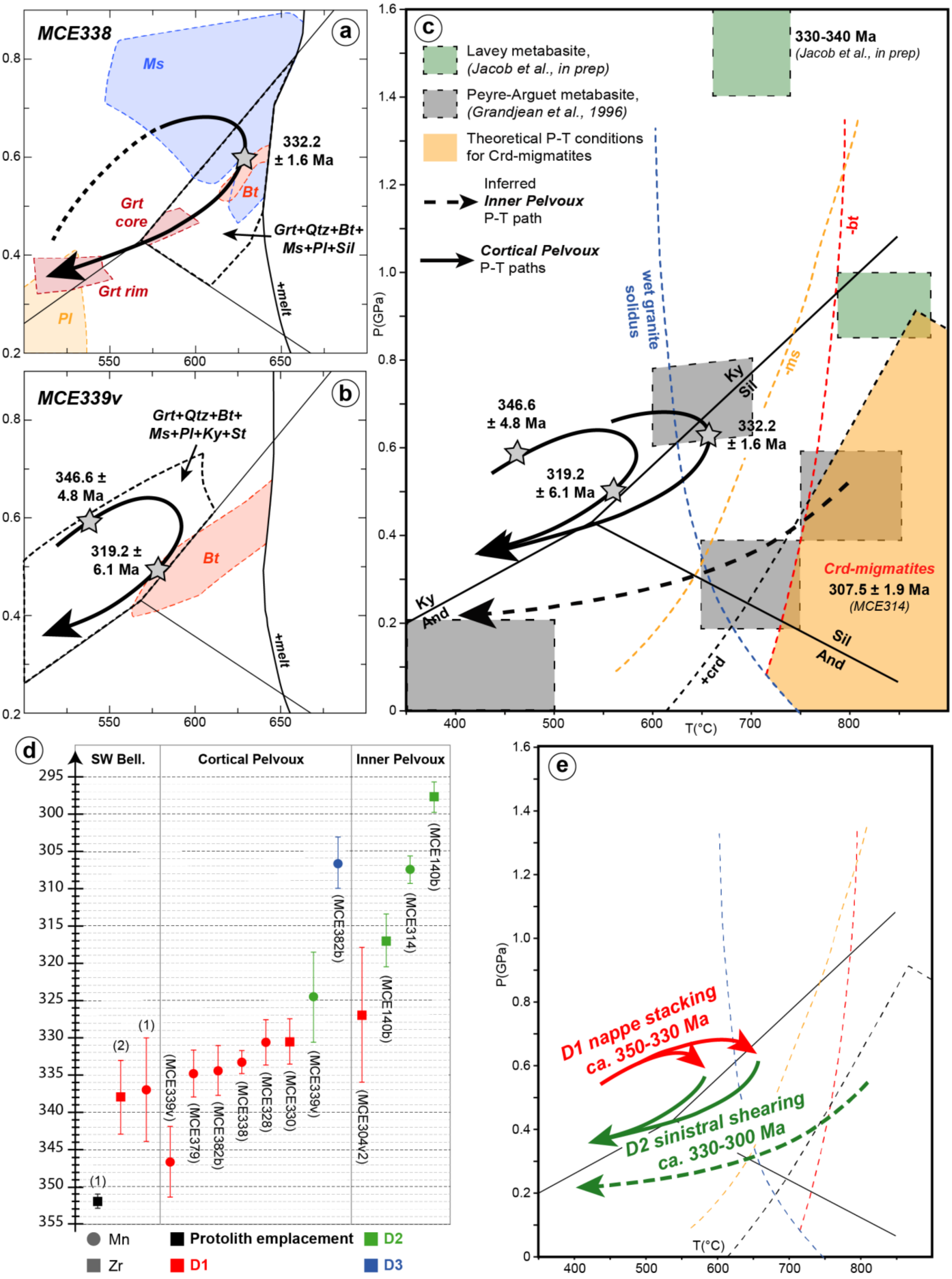
MCE338
a
Ms
Grt core
Bt
Grt rim
Pl
332.2 ± 1.6 Ma
Grt+Qtz+Bt+Ms+Pl+Sil
+melt
0.8
0.6
0.4
0.2
550
600
650
MCE339v
b
Grt+Qtz+Bt+Ms+Pl+Ky+St
346.6 ± 4.8 Ma
319.2 ± 6.1 Ma
Bt
+melt
c
Lavey metabasite, (Jacob et al., in prep)
Peyre-Arguet metabasite, (Grandjean et al., 1996)
Theoretical P-T conditions for Crd-migmatites
Inferred Inner Pelvoux P-T path
Cortical Pelvoux P-T paths
330-340 Ma (Jacob et al., in prep)
wet granite solidus
-ms
-bt
Ky
Sil
And
+crd
346.6 ± 4.8 Ma
332.2 ± 1.6 Ma
319.2 ± 6.1 Ma
Crd-migmatites
307.5 ± 1.9 Ma (MCE314)
P(GPa)
T(°C)
1.6
1.4
1.2
1.0
0.8
0.6
0.4
0.2
0
400
500
600
700
800
d
SW Bell.
Cortical Pelvoux
Inner Pelvoux
295
300
305
310
315
320
325
330
335
340
345
350
355
(1)
(2)
(1)
(MCE339v)
(MCE379)
(MCE382b)
(MCE338)
(MCE328)
(MCE330)
(MCE339v)
(MCE382b)
(MCE304v2)
(MCE140b)
(MCE314)
(MCE140b)
● Mn
■ Zr
■ Protolith emplacement
■ D1
■ D2
■ D3
e
D1 nappe stacking ca. 350-330 Ma
D2 sinistral shearing ca. 330-300 Ma
P(GPa)
T(°C)
1.6
1.4
1.2
1.0
0.8
0.6
0.4
0.2
0
400
500
600
700
800

1392 Figure 17

1393

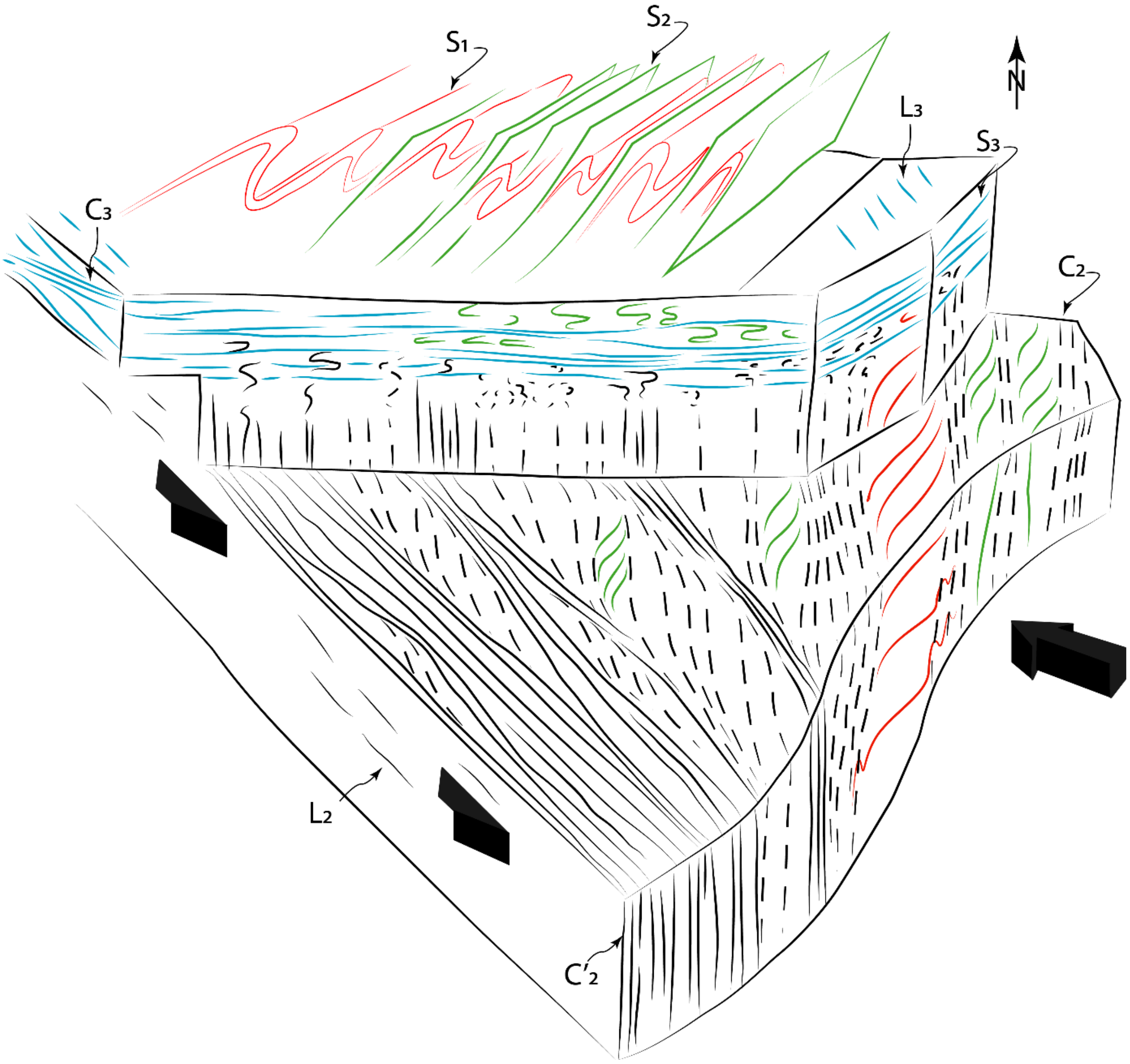

1394

1395

1396

1397

Figure 18

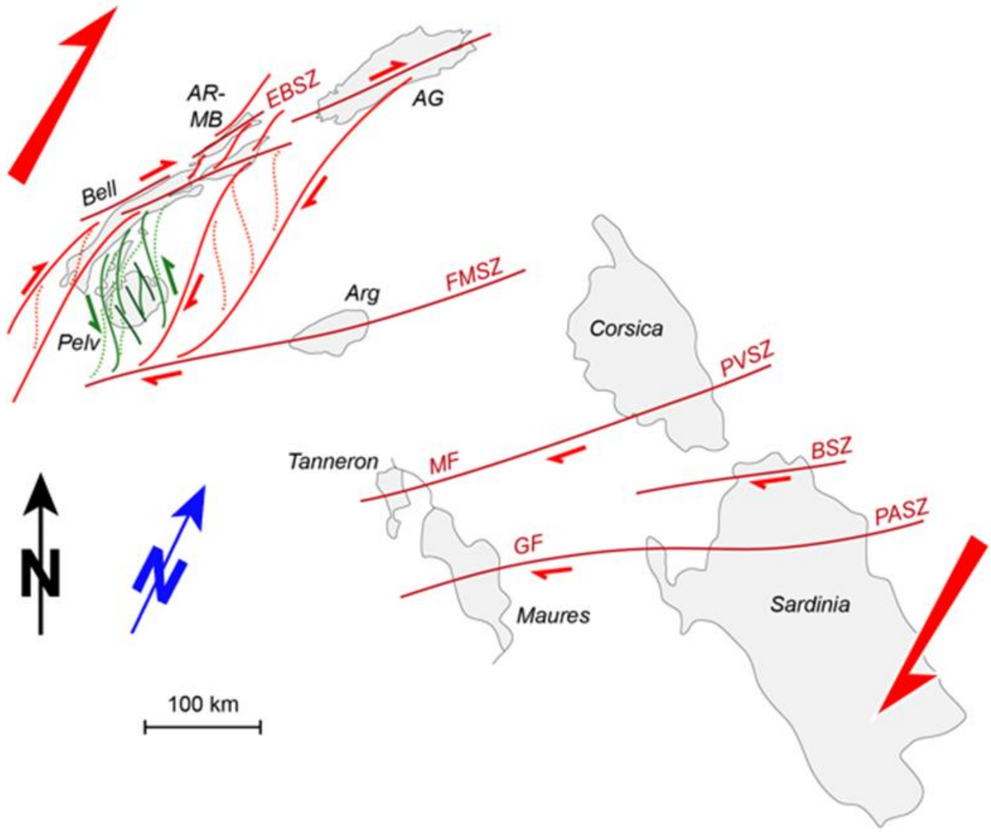
AR-
MB
EBSZ
AG
Bell
Arg
FMSZ
Pelv
Corsica
PVSZ
Tanneron
MF
BSZ
PASZ
GF
Sardinia
Maures
N
N
100 km

Table 1

Sample	Rock type	GPS location	Mineral dated	U-Th-Pb age (±2σ)
Cortical Pelvoux				
MCE379	Mylonitic gneiss	N45°1'23.49" E06°2'33.70"	Monazite	334.8 ± 3.2 Ma
MCE382b	Mylonitic Grt-gneiss	N45°1'2.61" E06°2'50.99"	Monazite	334.5 ± 3.4 Ma
				306.0 ± 3.5 Ma
MCE339v	Grt-St-Ky-metapelite	N44°52'52.00" E05°59'17.34"	Monazite	346.6 ± 4.8 Ma
				319.2 ± 6.1 Ma
MCE338	Sill-Grt-metapelite	N44°52'58.84" E06°0'49.10"	Monazite	333.2 ± 1.6 Ma
MCE328	Ky-St-metapelite	N44°47'12.12" E06°4'1.62"	Monazite	330.7 ± 3.1 Ma
MCE330	Roux migmatite	N44°47'29.86" E06°5'18.09"	Zircon	330.5 ± 3.1 Ma
				590.6 ± 6.2 Ma
Inner Pelvoux				
MCE314	Peyre-Arguet Crd-migmatite	N44°50'6.69" E06°22'2.42"	Monazite	307.5 ± 1.9 Ma
MCE313b	Peyre-Arguet migmatite	N44°56'4.37" E06°12'55.58"	Zircon	451.4 ± 5.2 Ma
MCE140b	Etages migmatite	N44°56'4.37" E06°12'55.58"	Zircon	297.8 ± 2.1 Ma
				317.0 ± 3.6 Ma
MCE304v2	Peyre-Arguet metabasite	N44°50'15.34" E06°21'22.25"	Zircon	326.9 ± 9.1 Ma
				471.3 ± 5.0 Ma

Table 2

oxyde (wt%)	SiO_2	Al_2O_3	FeO	MgO	CaO	Na_2O	K_2O	TiO_2	MnO	P_2O_5	Cr_2O_3	NiO	LOI	total
MCE339v	*67,30*	*16,00*	*5,95*	*2,26*	*1,01*	*2,09*	*3,18*	*0,75*	*0,07*	*0,16*	*0,01*	*0,00*	*2,15*	*100,93*
MCE338	*59,70*	*19,00*	*7,32*	*3,26*	*1,09*	*2,07*	*3,82*	*0,93*	*0,11*	*0,12*	*0,02*	*0,00*	*2,95*	*100,39*

Table 3

	Garnet				Biotite		Muscovite	Plagioclase
	MCE339v		MCE338		MCE339v	MCE338	MCE338	MCE338
	Core	Rim	Core	Rim				
Oxydes (wt%)								
SiO2	36,39	36,71	36,38	36,54	34,19	35,05	46,27	61,19
Al2O3	20,34	20,44	20,48	20,16	19,23	18,45	36,41	23,14
TiO2	0,19	0,05	0,03	0,01	1,66	1,47	0,34	
FeO	29,56	33,90	31,96	30,09	20,16	20,48	1,33	
MgO	1,27	2,31	3,14	2,02	8,63	9,10	0,69	
MnO	4,57	0,86	4,78	8,13	0,05	0,05	0,02	
CaO	6,62	5,14	1,93	1,31	0,00	0,02	0,03	4,83
Na2O					0,11	0,18	1,31	8,61
K2O					8,51	8,99	9,62	0,11
Total	*98,94*	*99,41*	*98,70*	*98,26*	*92,54*	*93,79*	*96,02*	*97,88*
Mol cations								
Si	2,97	2,97	2,97	3,02	2,68	2,72	3,05	2,79
Al	1,96	1,96	1,98	1,96	1,78	1,69	2,83	1,24
Ti	0,01	0,00	0,00	0,00		0,09	0,02	
Fe^{2+}	2,02	2,30	2,14	2,05	1,32	1,33	0,07	
Fe^{3+}	0,00	0,00	0,05	0,03				
Mg	0,16	0,28	0,38	0,25	1,01	1,05	0,07	
Mn	0,32	0,06	0,33	0,61	0,00	0,00	0,00	
Ca	0,58	0,45	0,57	0,11	0,00	0,00	0,00	0,24
Na					0,02	0,03	0,17	0,62
K					0,85	0,89	0,81	0,01
X_{Fe}					0,57	0,56		
End members								71,89
An								27,34
Orth								0,77
Prp	5,13	9,21	12,66	8,35				
Alm	65,26	74,09	70,77	68,69				
Grs	18,87	14,49	5,51	3,85				
Sps	10,45	1,96	10,97	19,07				

Figure 4

Event		Belledonne SW	Cortical Pelvoux	Inner Pelvoux
D3	Structure		Low angle S3 +/- mylonitc Horizontal axis F3 fold and a-Type F3 fold Top to NE shearing	Low angle S3 +/- mylonitic Horizontal axis F3 fold
	P-T		Retrograde amphibolite facies 0.45-0.35 GPa-450- 50 °C	High-T migmatite Cordierite bearing migmatite
	Age		ca. 306-298 Ma	*ca.* 306-298 Ma ?
D2	Structure	High angle S2 N030E Upright fold NE-SW axis NE-SW L2	High angle S2 N030E High angle C2 N-S High angle C'2 N150E Folded S2, Horizontal axis	High angle S2 N030E Upright fold NE-SW axis High angle C2 N-S High angle C'2 N150E NS to NE-SW L2
	P-T	Sill +melt	Low-T migmatite	Low-T migmatite
	Age	ca. 330-310 Ma *Freville et al. 2018*	*ca.* 330-298 Ma	*ca.* 330-298 Ma
D1	Structure	Low angle S1 Recumbent fold to the east E-W L1	Mark the lithological limits low angle S1-3	Mostly erased Relictual S1 in F2 fold hinge
	P-T	Amphibolite facies Grt-Bt +melt 0.6-0.8 GPa-600-630°C	Amphibolite facies ? +melt	No evidence
	Age	339 +/- 5 Ma	*ca.* 350-330 Ma	*ca.* 340-330 Ma ? (HP stage, *Jacob et al., in review*)

Figure S1

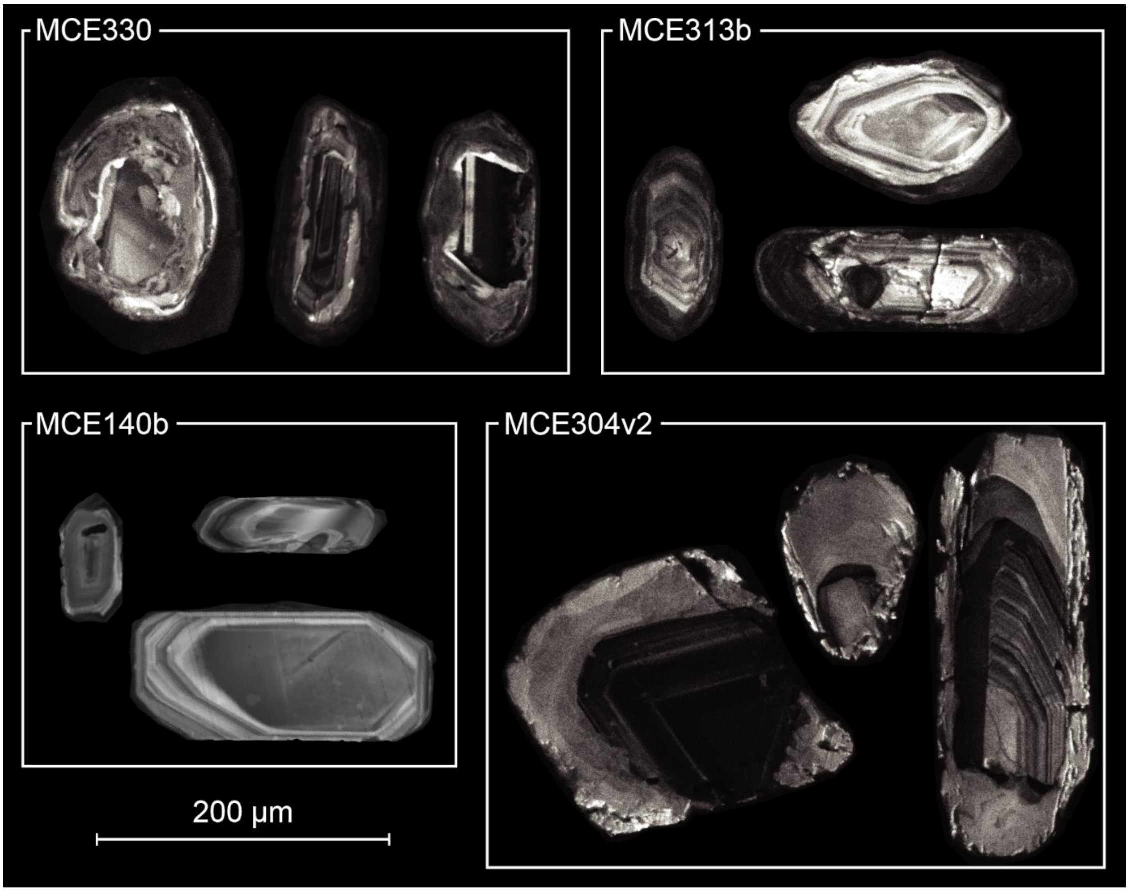
MCE330
MCE313b
MCE140b
MCE304v2
200 µm

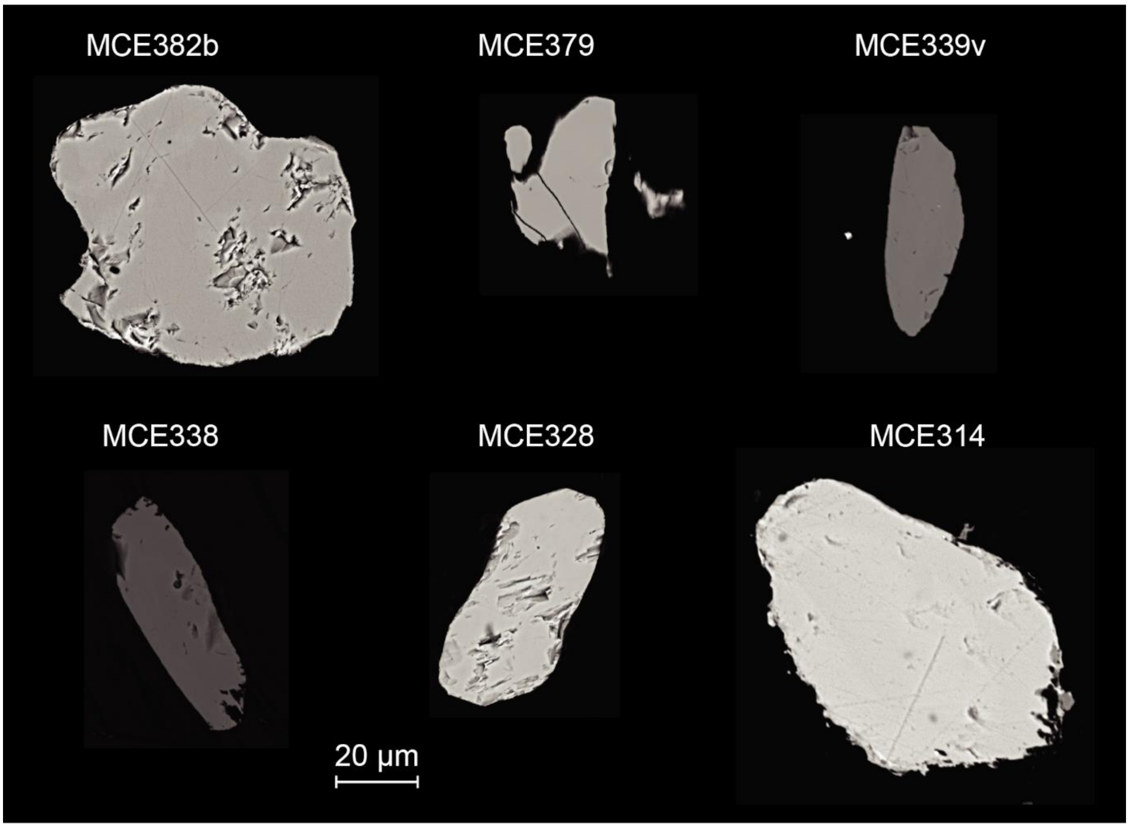
MCE382b
MCE379
MCE339v
MCE338
MCE328
MCE314
20 µm

1422

1423

Table S1

					Isotopic Ratios		
	U (ppm)	Pb (ppm)	207Pb/206Pb	±1σ	207Pb/235U	±1σ	206Pb/238
MCE330 (Roux migmatite)							
mce330-1	1093	101	0,0602	0,0024	0,8661	0,0329	0,104
mce330-2	1258	58	0,0528	0,0027	0,3776	0,0185	0,051
mce330-3	1614	140	0,0580	0,0021	0,7825	0,0276	0,097
mce330-4	951	45	0,0536	0,0026	0,3939	0,0186	0,053
mce330-5	868	74	0,0584	0,0024	0,7774	0,0306	0,096
mce330-6	331	31	0,0560	0,0030	0,8072	0,0426	0,104
mce330-7	139	40	0,1303	0,0053	5,8510	0,2323	0,325
mce330-8	1142	99	0,0606	0,0023	0,8151	0,0296	0,097
mce330-9	2004	95	0,0521	0,0021	0,3862	0,0154	0,053
mce330-10	1007	80	0,0582	0,0025	0,7221	0,0307	0,089
mce330-11	247	12	0,0556	0,0044	0,4076	0,0313	0,053
mce330-12	1055	49	0,0527	0,0025	0,3811	0,0174	0,052
mce330-13	506	42	0,0635	0,0036	0,8163	0,0449	0,093
mce330-14	923	49	0,0565	0,0027	0,4721	0,0219	0,060
mce330-15	649	173	0,1098	0,0046	4,5500	0,1852	0,300
mce330-16	150	15	0,0957	0,0066	1,4641	0,0977	0,111
mce330-17	765	36	0,0550	0,0029	0,4060	0,0208	0,053
mce330-18	1226	55	0,0523	0,0028	0,3675	0,0195	0,050
mce330-19	621	52	0,0562	0,0031	0,7296	0,0391	0,094
mce330-20	1561	70	0,0562	0,0031	0,3948	0,0215	0,051
mce330-21	321	26	0,0623	0,0041	0,7939	0,0514	0,092
mce330-22	624	53	0,0606	0,0036	0,8077	0,0462	0,096
mce330-23	1178	54	0,0528	0,0031	0,3783	0,0218	0,052
mce330-24	1237	59	0,0534	0,0031	0,3998	0,0229	0,054
mce330-25	651	30	0,0547	0,0036	0,3979	0,0256	0,052
mce330-26	2605	119	0,0569	0,0034	0,4050	0,0236	0,051
mce330-27	787	73	0,0635	0,0039	0,9153	0,0551	0,104
mce330-28	338	29	0,0610	0,0042	0,8110	0,0545	0,096
mce330-29	323	27	0,0615	0,0045	0,8054	0,0577	0,095
mce330-30	396	23	0,0601	0,0044	0,5393	0,0381	0,065
MCE304v2 (Peyre-Arguet metabasite)							
mce304V2-1	301	20,2	0,0586	0,0028	0,6144	0,0283	0,076
mce304V2-2	32	1,4	0,0702	0,0111	0,4882	0,0751	0,050
mce304V2-3	545	36,2	0,0562	0,0023	0,5822	0,0237	0,075
mce304V2-4	164	11	0,0536	0,0047	0,5586	0,0477	0,075
mce304V2-5	153	8,2	0,0581	0,0046	0,4854	0,0372	0,060
mce304V2-6	27	1,3	0,0569	0,0115	0,4170	0,0826	0,053

mce304V2-7	1349	89,6	0,0576	0,0021	0,5964	0,0210	0,075
mce304V2-8	27	1,3	0,0939	0,0130	0,6750	0,0904	0,052
mce304V2-9	199	13,6	0,0568	0,0042	0,6032	0,0435	0,077
mce304V2-10	104	7	0,0611	0,0046	0,6409	0,0473	0,076
mce304V2-11	189	12,3	0,0631	0,0038	0,6378	0,0369	0,073
mce304V2-12	8	0,3	0,0911	0,0243	0,6372	0,1644	0,050
mce304V2-13	166	11,5	0,0570	0,0033	0,6131	0,0344	0,078
mce304V2-14	12	0,6	0,0996	0,0219	0,7286	0,1553	0,053
mce304V2-15	81	6,1	0,0576	0,0046	0,6802	0,0527	0,085
mce304V2-16	43	2	0,0502	0,0076	0,3599	0,0536	0,052
mce304V2-17	72	3,3	0,0455	0,0063	0,3269	0,0446	0,052
mce304V2-18	801	53,3	0,0572	0,0025	0,5908	0,0254	0,074
mce304V2-19	483	35,8	0,0582	0,0031	0,6695	0,0344	0,083
mce304V2-20	5	0,2	0,1517	0,0743	0,9431	0,4450	0,045
mce304V2-21	1852	91,5	0,0872	0,0037	0,6665	0,0275	0,055
mce304V2-22	6	0,3	0,1290	0,0398	0,9654	0,2859	0,054
mce304V2-23	114	6,3	0,0612	0,0047	0,5190	0,0387	0,061
mce304V2-24	142	10,2	0,0612	0,0049	0,6761	0,0526	0,080
mce304V2-25	29	1,3	0,0542	0,0112	0,3874	0,0790	0,051
mce304V2-26	677	41,8	0,0621	0,0031	0,5925	0,0289	0,069
mce304V2-27	3	0,1	0,2312	0,0686	1,7179	0,4555	0,053
mce304V2-28	102	6,8	0,0571	0,0052	0,5848	0,0522	0,074
mce304V2-29	1480	86,5	0,0562	0,0028	0,5072	0,0245	0,065
MCE140b (Etage migmatite)							
5010616	25	469	0,0527	0,0051	0,3668	0,0053	0,050
6010616	21	404	0,0531	0,0046	0,3690	0,0052	0,050
7010616	189	4205	0,0523	0,0044	0,3407	0,0043	0,047
8010616	84	1723	0,0524	0,0045	0,3651	0,0047	0,050
9010616	195	4292	0,0524	0,0044	0,3408	0,0043	0,047
10010616	71	1548	0,0528	0,0044	0,3658	0,0049	0,050
11010616	129	2730	0,0522	0,0046	0,3401	0,0043	0,047
12010616	54	1196	0,0525	0,0046	0,3397	0,0045	0,046
16010616	106	2329	0,0527	0,0044	0,3420	0,0044	0,047
17010616	69	1541	0,0526	0,0046	0,3417	0,0046	0,047
18010616	109	2361	0,0535	0,0040	0,3510	0,0045	0,047
19010616	80	1727	0,0524	0,0046	0,3208	0,0042	0,044
20010616	90	1971	0,0520	0,0049	0,3374	0,0044	0,047
21010616	71	938	0,0579	0,0029	0,5814	0,0076	0,072
22010616	95	2083	0,0527	0,0045	0,3443	0,0045	0,047
23010616	64	1460	0,0521	0,0049	0,3212	0,0043	0,044
27010616	20	279	0,0569	0,0035	0,5804	0,0084	0,073
28010616	90	2143	0,0532	0,0043	0,3123	0,0042	0,042
29010616	55	1165	0,0528	0,0046	0,3477	0,0047	0,047
30010616	55	1174	0,0529	0,0046	0,3423	0,0047	0,046
31010616	78	1818	0,0530	0,0045	0,3236	0,0044	0,044

32010616	43	1112	0,0548	0,0041	0,3007	0,0045	0,039
33010616	89	2001	0,0533	0,0044	0,3363	0,0046	0,045
34010616	129	2961	0,0533	0,0044	0,3316	0,0045	0,045
38010616	53	1308	0,0523	0,0053	0,2974	0,0043	0,041
39010616	216	5260	0,0529	0,0047	0,3161	0,0044	0,043
40010616	78	1772	0,0538	0,0043	0,3344	0,0047	0,045
41010616	87	1954	0,0542	0,0042	0,3294	0,0047	0,044
MCE313b (Peyre Arguet migmatite)							
mce313b-1	1645	79	0,0568	0,0020	0,4266	0,0147	0,054
mce313b-2	353	23	0,0565	0,0027	0,5834	0,0268	0,074
mce313b-4	411	26	0,0560	0,0029	0,5597	0,0278	0,072
mce313b-5	1043	66	0,0569	0,0024	0,5642	0,0234	0,072
mce313b-7	631	38	0,0583	0,0023	0,5489	0,0210	0,068
mce313b-9	466	32	0,0623	0,0027	0,6653	0,0283	0,077
mce313b-12	472	29	0,0643	0,0031	0,6211	0,0294	0,070
mce313b-15	2404	96	0,0544	0,0022	0,3364	0,0132	0,044
mce313b-17	327	21	0,0582	0,0028	0,5660	0,0264	0,070
mce313b-18	2335	90	0,0608	0,0029	0,3633	0,0165	0,043
mce313b-19	2106	90	0,0558	0,0024	0,3684	0,0153	0,047
mce313b-21	499	30	0,0620	0,0033	0,5689	0,0289	0,066
mce313b-22	436	28	0,0579	0,0033	0,5778	0,0320	0,072
mce313b-23	815	49	0,0558	0,0028	0,5169	0,0254	0,067
mce313b-24	566	37	0,0564	0,0030	0,5639	0,0293	0,072
mce313b-26	292	19	0,0618	0,0038	0,6162	0,0364	0,072
mce313b-28	1608	71	0,0567	0,0028	0,3880	0,0182	0,049
mce313b-29	286	27	0,0641	0,0036	0,9290	0,0508	0,105
mce313b-30	753	59	0,0601	0,0031	0,7272	0,0368	0,087

Table S2

Table S2: Operating conditions for the LA-ICP-MS equipment

Laboratory & Sample Preparation	
Laboratory name	Géosciences Montpellier, UMR CNRS 5243, Montpellier, France
Sample type/mineral	Monazite
Sample preparation	Polished thin-section
Imaging	Hirox SH3000, BSE detector BRGM
Laser ablation system	
Make, Model & type	LambdaPhysiks, Compex 102, Excimer
Ablation cell	Geolas
Laser wavelength	193 nm
Pulse width	15 ns
Fluence	10 J/cm^{-2}
Repetition rate	2 Hz
Spot size	26 µm
Sampling mode / pattern	Single spot
Carrier gas	100% He mixed with Ar before entering the plasma
Background collection	15 seconds
Ablation duration	45 seconds
Wash-out delay	/
Cell carrier gas flow (He)	0.3 l/min
ICP-MS Instrument	
Make, Model & type	Element XR, SF-ICP-MS
Sample introduction	Via conventional tubing
RF power	1350W
Sampler, skimmer cones	Ni
Extraction lenses	/
Make-up gas flow (Ar)	0.6 l/min
Detection system	Electron multiplier
Data acquisition protocol	Time-resolved analysis
Scanning mode	Peak hopping, three points per peak
Detector mode	Pulse counting, except for ^{208}Pb and ^{232}Th (analog mode), dead time correction applied.
Masses measured	^{204}(Hg + Pb), ^{206}Pb, ^{207}Pb, ^{208}Pb, ^{232}Th, ^{238}U
Integration time per peak	10.24 ms for all masses, except ^{208}Pb and ^{232}Th (5.12 ms) and ^{207}Pb (40.96 ms)
Sensitivity / Efficiency	3000 cps/ppm Pb (26µm, 4Hz)
Data Processing	
Gas blank	15 seconds on-peak
Calibration strategy	Manangotry monazite standard used as primary reference material.
Reference Material info	Manangotry (Poitrasson et al., 2000)
Data processing package used	GLITTER ® (van Achterbergh et al., 2001)
Quality control / Validation	/

Table S3

Laboratory & Sample Preparation	
Laboratory name	Bureau de Recherche Géologique et Minière (BRGM), Orléans, France
Sample type/mineral	Zircon
Sample preparation	Polished thin-section
Imaging	Hirox SH3000, BSE detector BRGM
Laser ablation system	
Make, Model & type	CETAC Excite 193, Excimer
Ablation cell	HelEx II
Laser wavelength	193 nm
Pulse width	15 ns
Fluence	6 J/cm^{-2}
Repetition rate	3 Hz
Spot size	15 µm
Sampling mode / pattern	Single spot
Carrier gas	100% He mixed with Ar with 'Squid system' before entering the plasma
Background collection	20 seconds
Ablation duration	40 seconds
Wash-out delay	/
Cell carrier gas flow (He)	0.45 l/min
ICP-MS Instrument	
Make, Model & type	Thermo-scientific, X-serie II, Q-ICP-MS
Sample introduction	Via conventional tubing
RF power	1400W
Sampler, skimmer cones	Ni
Extraction lenses	/
Make-up gas flow (Ar)	1 l/min
Detection system	Electron multiplier
Data acquisition protocol	Time-resolved analysis
Masses measured	^{204}(Hg + Pb), ^{206}Pb, ^{207}Pb, ^{208}Pb, ^{232}Th, ^{238}U
Integration time	50 ms for all masses
Data Processing	
Calibration strategy	Trebilcock monazite standard used as primary reference material.
Reference Material info	Trebilcock (272 ± 2 Ma, Tomascak et al. 1996)
Data processing package used	GLITTER ® (van Achterbergh et al., 2001)
Quality control / Validation	Madmon Monazite standard used has quality control (515 Ma, Schulz et al., 2007.)

Table S4

Table S4: Operating conditions for the LA-ICP-MS equipment

Laboratory & Sample Preparation	
Laboratory name	GeOHeLiS Analytical Platform, OSUR, Univ Rennes 1, France
Sample type/mineral	Detrital zircon
Sample preparation	Epoxy mount
Imaging	MIRA3 TESCAN, Tescan CL detector (semi-parabolic mirror and light guide), BRGM
Laser ablation system	
Make, Model & type	ESI NWR193UC, Excimer
Ablation cell	ESI NWR TwoVol2
Laser wavelength	193 nm
Pulse width	< 5 ns
Fluence	8 J/cm-2
Repetition rate	4 Hz
Spot size	25 µm
Sampling mode / pattern	Single spot
Carrier gas	100% He, Ar make-up gas and N2 (3 ml/mn) combined using in-house smoothing device
Background collection	20 seconds
Ablation duration	60 seconds
Wash-out delay	15 seconds
Cell carrier gas flow (He)	0.75 l/min
ICP-MS Instrument	
Make, Model & type	Agilent 7700x, Q-ICP-MS
Sample introduction	Via conventional tubing
RF power	1350W
Sampler, skimmer cones	Ni
Extraction lenses	X type
Make-up gas flow (Ar)	0.85 l/min
Detection system	Single collector secondary electron multiplier
Data acquisition protocol	Time-resolved analysis
Scanning mode	Peak hopping, one point per peak
Detector mode	Pulse counting, dead time correction applied, and analog mode when signal intensity > ~ 10^6 cps
Masses measured	^{204}(Hg + Pb), ^{206}Pb, ^{207}Pb, ^{208}Pb, ^{232}Th, ^{238}U
Integration time per peak	10-30 ms
Sensitivity / Efficiency	22000 cps/ppm Pb (50µm, 10Hz)
Data Processing	
Gas blank	20 seconds on-peak
Calibration strategy	GJ1 zircon standard used as primary reference material, Plešovice used as secondary reference material (quality control)
Reference Material info	GJ1 (Jackson et al., 2004) Plešovice (Slama et al., 2008)
Data processing package used	GLITTER ® (van Achterbergh et al., 2001)
Quality control / Validation	Plešovice: concordia age = 336.3 ± 3.3 Ma (N=6; MSWD=0.54)